The relation between martensitic phase transformation and martensite reorientation in single crystal Ni-Mn-Ga magneticshape memory alloy

Guoshun Qin

To cite this version:

Guoshun Qin. The relation between martensitic phase transformation and martensite reorientation in single crystal Ni-Mn-Ga magneticshape memory alloy. Fluids mechanics [physics.class-ph]. Institut Polytechnique de Paris, 2021. English. NNT : 2021IPPAE011 . tel-03347001

NNT : 2021IPPAE011

Thèse de doctorat

The relation between martensitic phase transformation and martensite reorientation in single crystal Ni-Mn-Ga magnetic shape memory alloy

Thèse de doctorat de l'Institut Polytechnique de Paris
préparée à l'École nationale supérieure de techniques avancées

École doctorale n°626 de l'Institut Polytechnique de Paris (ED IP Paris)
Spécialité de doctorat: Mécanique des fluides et des solides, acoustique

Thèse présentée et soutenue à Palaiseau, le 03/09/2021, par

Guoshun QIN

Composition du Jury :

Etienne PATOOR Professeur, Georgia Tech-Lorraine	Président
Xavier BALANDRAUD Professeur, Université Clermont-Auvergne	Rapporteur
Tarak BEN ZINEB Professeur, Université de Lorraine	Rapporteur
Olivier HUBERT Professeur, ENS Paris Saclay	Examinateur
Ziad MOUMNI Professeur, ENSTA Paris	Examinateur
Yongjun HE Maîtres de conférences, ENSTA Paris	Directeur de thèse

Acknowledgements

This thesis is a summary of my research work in the past three years. During this period, many people give me help and support, and I wish to express my gratitude to them.

Firstly, I wish to express the sincerest gratitude towards my advisor Mr. Yongjun HE. He gave me lots of guidance and help in my research work. It’s a great pleasure to work with him because I learned a lot from him, not only the professional knowledge, but also his forever passion to scientific research, his rigorous attitude towards data analysis, his philosophy thoughts to deal with problems etc. All these things will influence and help me to better deal with the problems in the future.

Secondly, I wish to appreciate Mr. Ziad MOUMNI, director of my research group. His support helps me to accomplish my experimental work. I admire his kind and enthusiastic characters, and I’m happy and grateful to work in our research group.

Thirdly, I want to thank Xue CHEN, Shaobin ZHANG and Chengguan ZHANG, the former and the present Ph.D. students of my advisor. Discussion with them helped me overcome lots of difficulties in my research work and inspired me many effective ideas.

Fourthly, I want to thank the colleagues in my lab, Nicolas THURIEAU, Lahcene CHERFA, Thierry PICHON, Xiaofei JU, Gulcan OZERIM, Baris TELMEN etc. They all help me a lot during my Ph.D. period.

Lastly, I thank my families. My girlfriend Yaqian SHEN accompanied me to pass through my Ph.D. period and gave me much support and encouragement. My parents’ support is also very important to accomplish my Ph.D. work.

Publications

Journals

Zhang, S., **Qin, G.**, He, Y., 2020. Ambient effects on the output strain of Ni–Mn-Ga single crystal magnetic shape memory alloy. ***Journal of Alloys and Compounds*** 835, 155159.

Qin, G., Zhang, C., Zhang, S., Chen, X., He, Y., 2021. Self-accommodation versus Two-way memory in Ni-Mn-Ga single crystal. (Under review)

Abstract

Magnetic shape memory alloy (MSMA) is a promising candidate for actuators because of its high-frequency Magnetic-Field-Induced-Strain (MFIS) property. Compared to other types of MSMAs, Ni_2MnGa single crystal is the most popular one because of its much lower twinning stress ($\sigma_{tw} < 2$ MPa). Ni_2MnGa single crystal has two important microstructure processes: martensite reorientation and phase transformation, which give it various potential engineering applications. In literature, the martensite reorientation and phase transformation were usually studied separately. Their interaction (coupling) has not yet been systematically studied. In this thesis, I demonstrate in two typical situations (magnetic-field-induced martensite reorientation and stress-free temperature-induced phase transformation) that both martensite reorientation and phase transformation can take place simultaneously, leading to some special performances.

The first set of the systematic experiments investigates the thermal effect on the magnetic-field-induced strain oscillation of Ni_2MnGa single crystal by stepwise gradually changing thermal boundary condition (from still ambient air to strong airflow). The results show that the extremely weak or extremely strong ambient heat transfer can only have small strain oscillation amplitude while the maximum strain amplitude can be achieved only at a mild heat transfer condition (i.e., non-monotonic dependence of the strain amplitude on the ambient heat.) Particularly at weak ambient heat transfer, the energy dissipation of the high-frequency martensite reorientation can trigger the temperature increase of the specimen, leading to the phase transformation to austenite phase, which can in turn modulate the strain oscillation amplitude by the phase-fraction adjustment of the martensitic phase transformation.

The second set of the systematic experiments investigates the martensitic phase transformation of the Ni_2MnGa single crystal bars of different geometric sizes under different heating-cooling cycles without stress or magnetic-field. The experimental results show that the cooling-induced austenite → martensite phase transformation in Ni_2MnGa single crystal slim bar takes place via two steps: (1) austenite → martensite twin(s); (2) detwinning into single martensite variant (the major martensite variant in the twin frows at the expense of the minor martensite variant; i.e., the reorientation from the minor martensite variant to the major martensite variant takes place). This new phenomenon demonstrates that the martensite reorientation indeed occurs during the cooling-induced phase transformation without any directional driving force (i.e., without stress or magnetic field), which can have a large global shape change. It breaks the usual idea about the self-accommodation martensite formation in the one-way shape memory effect. This finding promotes the SMA applications such as the stress-free two-way shape memory effect. But the accurate prediction/control on the performance is still a challenging task, demanding further experimental and theoretical research.

Keywords: heat transfer, magnetic-field-induced martensite reorientation, self-accommodation, two-way shape memory effect, martensitic phase transformation, compatibility, martensite detwinning.

Résumé

L'alliage magnétique à mémoire de forme (MSMA) est un candidat prometteur pour les actionneurs en raison de sa propriété de déformation induite par champ magnétique à haute fréquence. Comparé à d'autres types de FSMA, le monocristal Ni_2MnGa est le plus populaire en raison de sa contrainte de twinning beaucoup plus faible ($\sigma_{tw} < 2$ MPa). Le monocristal Ni_2MnGa a deux processus de microstructure importants : la réorientation de la martensite et la transformation de phase, qui lui donnent diverses applications potentielles en ingénierie. Dans la littérature, la réorientation de la martensite et la transformation de phase ont généralement été étudiées séparément. Leur interaction (couplage) n'a pas encore été systématiquement étudiée. Dans cette thèse, je démontre dans deux situations typiques (réorientation de la martensite induite par un champ magnétique et transformation de phase induite par la température sans contrainte) que la réorientation de la martensite et la transformation de phase peuvent avoir lieu simultanément, conduisant à des performances spéciales.

La première série d'expériences systématiques étudie l'effet thermique sur l'oscillation de déformation induite par le champ magnétique du monocristal de Ni_2MnGa en modifiant progressivement les conditions aux limites thermiques (de l'air ambiant immobile à un fort flux d'air). Les résultats montrent que le transfert de chaleur ambiant extrêmement faible ou extrêmement fort ne peut avoir qu'une faible amplitude d'oscillation de déformation, tandis que l'amplitude de déformation maximale ne peut être atteinte que dans des conditions de transfert de chaleur douces (c'est-à-dire une dépendance non monotone de l'amplitude de déformation sur la chaleur ambiante.) En particulier à faible transfert de chaleur ambiant, la dissipation d'énergie de la réorientation de la martensite à haute fréquence peut déclencher l'augmentation de la température de l'échantillon, conduisant à la transformation de phase en phase austénite, qui peut à son tour moduler l'amplitude d'oscillation de déformation par la fraction de phase ajustement de la transformation de phase martensitique.

La deuxième série d'expériences systématiques étudie la transformation de phase martensitique des barres monocristallines Ni_2MnGa de différentes tailles géométriques sous différents cycles de chauffage-refroidissement sans contrainte ni champ magnétique. Les résultats expérimentaux montrent que la transformation de phase d'austénite en martensite induite par le refroidissement dans un barreau mince monocristallin de Ni_2MnGa s'effectue en deux étapes : (1) austénite en martensite jumeau(s); (2) le detwinning en variante martensite simple (la variante majeure de martensite dans les jumeaux aux dépens de la variante mineure de martensite ; c'est-à-dire que la réorientation de la variante mineure de martensite vers la variante majeure de martensite a lieu). Ce nouveau phénomène démontre que la réorientation de la martensite s'est effectivement produite lors de la transformation de phase induite par le refroidissement sans aucune force motrice directionnelle (sans contrainte ni champ magnétique), ce qui peut avoir un grand changement de forme global. Cela brise l'idée habituelle sur la formation de martensite auto-accommodante dans l'effet de mémoire de forme à sens unique. Cette découverte favorise les applications de SMA telles que l'effet de mémoire de forme bidirectionnelle sans stress. Mais la prédiction/le contrôle précis de la performance est toujours une tâche difficile, exigeant des recherches expérimentales et théoriques supplémentaires.

Mots clés : transfert de chaleur, réorientation martensitique induite par champ magnétique, auto-accommodation, mémoire bidirectionnelle, transformation de phase martensitique, compatibilité, détwinning martensitique.

Contents

List of figures

Chapter 1

Introduction

1.1 Overview of ferromagnetic shape memory alloy

With the development of science and technology, the demand for the materials with exceptional performances is increasing intensively. Smart/active materials, as a new type of multifunctional material, has attracted a wide attention in the last century. Smart materials can change one or more properties in response to the external stimuli, such as stress, electric field, magnetic field, temperature etc., which makes it potential for engineering applications, such as sensors and actuators (Tzou et al., 2004).

Conventional smart materials such as piezoelectric material and magnetostrictive material have the advantage of fast response (> 10 kHz), but yield only a small strain (<0.2%) (Karaca et al., 2007). By contrast, the conventional shape memory alloys (SMAs) can yield a very large strain (up to 8%), but the response speed is quite slow (1Hz). The conventional smart materials have the drawbacks (small strain or slow response), which seriously limits their applications.

Ferromagnetic shape memory alloys (FSMA), also called magnetic shape memory alloys (MSMA), is a new kind of smart materials with the coupling of their mechanical, thermal, and magnetic properties. They can work in high frequency range (up to 1kHz) and provide a large output strain (up to 10%) at the same time, which gives FSMAs great advantages over other kinds of the smart materials. Up to now, FSMAs have many potential engineering applications, such as actuators, sensors, energy harvesters and solid-state refrigeration (Chernenko et al., 2019; Kohl et al., 2009; Li et al., 2019; Liu et al., 2012; Song et al., 2013; Stephan et al., 2011; Straka et al., 2011b).

1.2 Ni_2MnGa single crystal

Several alloy systems have been confirmed to exhibit the characteristics of FSMAs, such as Ni-Mn-Ga, Ni-Fe-Ga, Fe-Pd, Co-Ni-Ga. (Heczko et al., 2000; James and Wuttig, 2009; Li et al., 2003; Morito et al., 2009; Sehitoglu et al., 2012). Among these alloys, Ni-Mn-Ga alloys are the most popular FSMAs. Since Ullakko et al. firstly reported 0.2% magnetic-field-induced strain (MFIS) by twin-boundary motion in Ni_2MnGa single crystal in 1996 (Ullakko et al., 1996), Ni_2MnGa single crystal has attracted a wide research interest (Chmielus et al., 2008; Chulist et al., 2013; Faran and Shilo, 2011, 2013; Heczko et al., 2000; Heczko et al., 2002; Karaca et al., 2006; Karaca et al., 2012; Kohl et al., 2014; Pagounis et al., 2014; Pinneker et al., 2014; Straka et al., 2012). Murray et al. obtained the nearly maximum theoretical strain of 6% in Ni_2MnGa single crystal at room temperature in 2000 (Murray et al., 2000), which makes it potential for engineering applications. The Ni_2MnGa single crystal usually exhibits a large reversible MFIS, but they are very brittle and expensive. These drawbacks encourage researches to develop Ni_2MnGa polycrystals which exhibit a much smaller MFIS because of the incompatibilities at grain boundaries (Ullakko et al. 2001; Jeong et al. 2003). Therefore, the Ni_2MnGa single crystals are still the research focus and numerous studies have been performed in different aspects, including crystal structure, phase transformation, martensite reorientation, magneto-caloric effect, two-way shape memory effect etc. (Chen and He, 2020; Heczko et al., 2002; Pascan et al., 2015; Radelytskyi et al., 2017; Wang et al., 2000; Webster et al., 1984; Zhang et al., 2018a, b). The thesis is focused on two basic and important properties of Ni_2MnGa single crystal: martensite reorientation and phase transformation.

1.2.1 Material structures of Ni_2MnGa single crystal

The Ni_2MnGa single crystals exhibit two phases under different temperatures: cubic austenite phase in high temperature and approximately “tetragonal” martensite phase in low temperature. The edge length of the austenite phase is noted as a_0, while the lengths of the long and short edge of the martensite phase are noted as a and c respectively as shown in

Fig.1.1 The lattice parameters are $a_0 \approx 0.584$ nm, $a \approx 0.595$ nm and $c \approx 0.561$ nm (Heczko et al., 2002; Straka et al., 2008). There exist 3 martensite variants M_1, M_2 and M_3 with the short axis along *x, y* and *z* axis respectively as shown in Fig.1.1. But strictly speaking, the martensite structure is monoclinic (12 variants) with a characteristic angle γ =90.37° (Chulist et al., 2013). As the monocinic distortion is small, the martensite structure of Ni_2MnGa single crystals is generaly considered as tetragonal structure to simplify the anlysis.

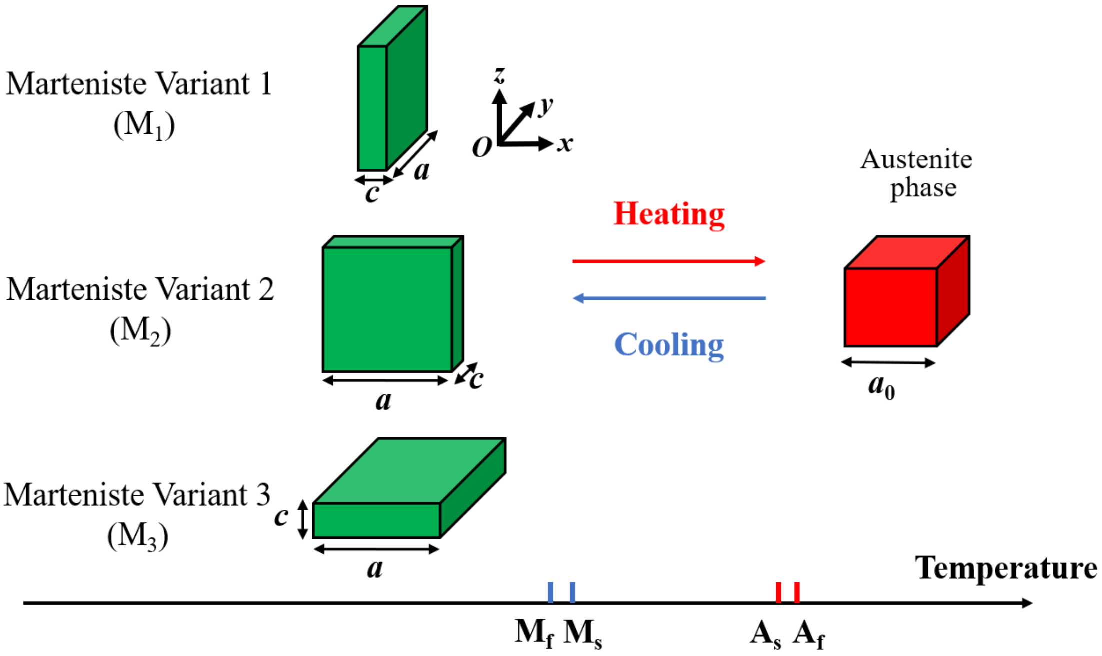

Figure 1.1 Lattice structures of Ni_2MnGa single crystal and the schematic diagram of temperature-induced phase transformation

1.2.2 Martensite reorientation

The martensite reorientation between different martensite variants can be induced by a mechanical stress, a magnetic field, or both in Ni_2MnGa single crystals.

1.2.2.1 Stress-induced martensite reorientation

The stress-induced martensite reorientation in Ni_2MnGa single crystals can be shown by the process from point “a” to point “d” in Figure 1.2. When a specimen initially consisting of the single variant M_1 is under a compression along *z* axis (point “a”), the variant M_3 nucleates and grows by twin boundary motion at the expense of the variant M_1 (from point “b” to point “c”). With the increase of the compressive stress, only the single variant M_3 exists at point “d” with a large strain up to 6% (so-called martensite reorientation). The maximum strain value 6% of Ni_2MnGa single crystals, depending on the degree of tetragonality of the martensite variant, can be theoretically calculated by $1-\frac{c}{a}$ (a and c are lattice parameters of martensite phase as shown in Figure 1.1). This strain will maintain during unloading (from point "d" to point "e" in Figure 1.2).

The twinning stress σ_{tw} (the plateau stress from point "b" to point "c") is an important parameter to characterize the driving force needed for the martensite reorientation. The Ni_2MnGa single crystals exhibit two types of twin boundaries (i.e., Type I and Type II) due to its slightly monoclinic structures, with the corresponding twinning stress of 0.8~1.4 MPa and 0.05~0.3 MPa respectively (Pascan, 2015; Sozinov et al., 2011; Straka et al., 2011a; Straka et al., 2012). Compared to other SMAs, the much smaller twinning stress of Ni_2MnGa single crystal, especially the Type II twin boundary, making it attractive for actuator applications.

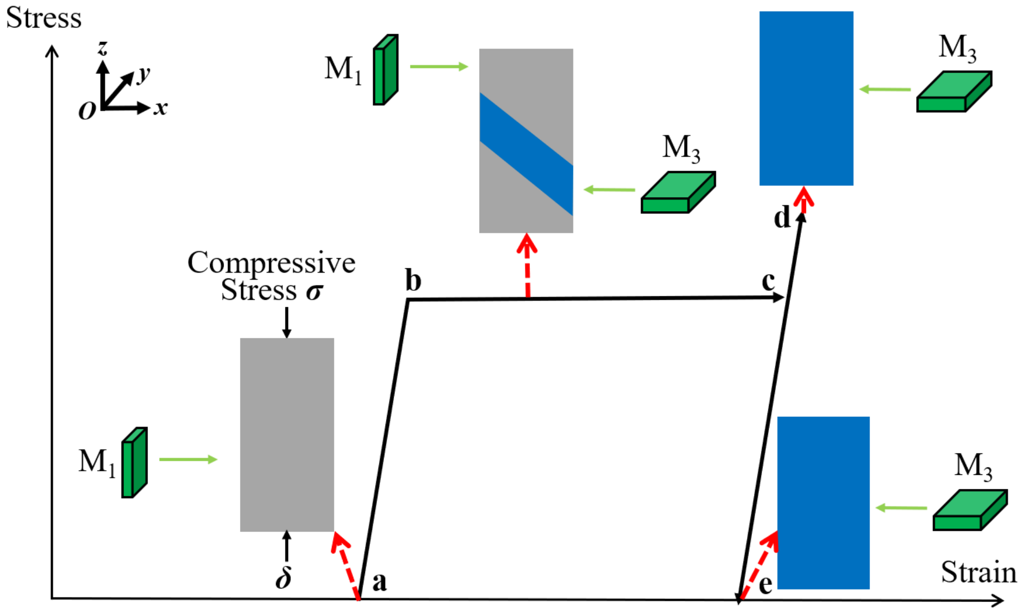

Figure 1.2 Schematic diagram of stress-induced martensite reorientation of Ni_2MnGa single crystal

1.2.2.2 Magnetic field-induced martensite reorientation

The magnetic-field induced martensite reorientation (MR) is based on the anisotropic magnetic energy in martensite variant of Ni_2MnGa single crystals, which means the magnetization vector prefers to align with the short axis c of martensite, to minimize the

Magnetocrystalline Anisotropy Energy (MAE). As shown in Figure 1.3, an external magnetic field along *x* axis is applied to the material in the initial state of single variant M_3 (point “a”). A part of variant M_3 will transform to variant M_1 whose short axis is along the external magnetic field direction (i.e., *x* axis), so-called magnetic field-induced martensite reorientation. With the increase of the magnetic field, the martensite reorientation continues (from point “b” to point “c”), which is achieved by the twin boundary motion, and finally all the variant M_3 transforms to the variant M_1 (point “d”) with a large strain up to 6%. This strain will remain when the external magnetic field is removed (from point “d” to point “e”).

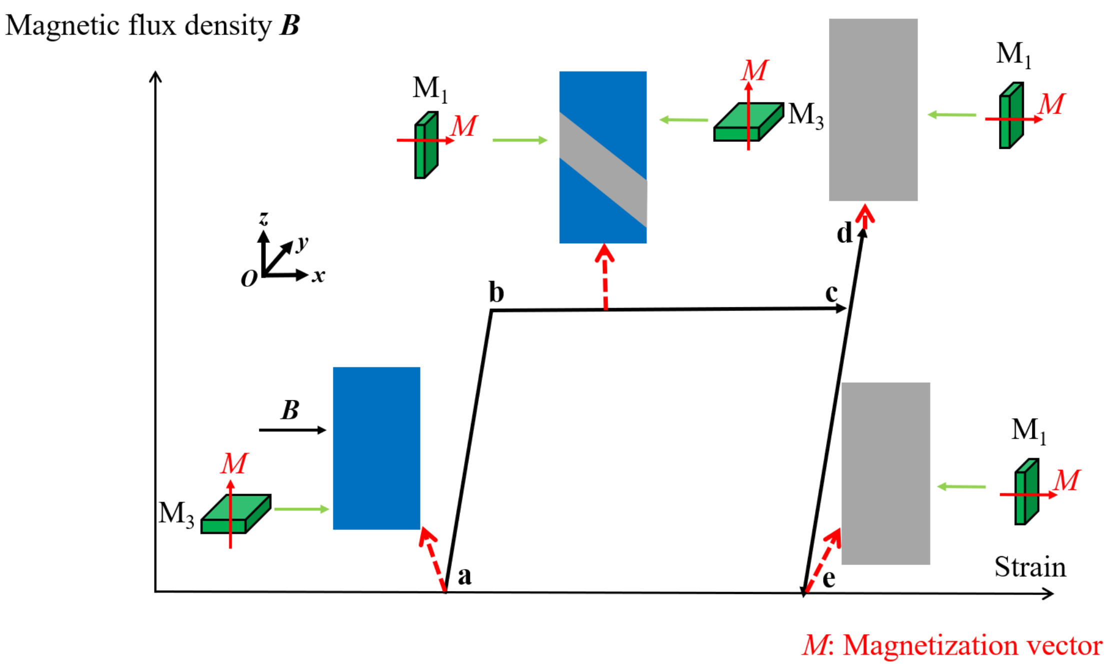

Figure 1.3 Schematic diagram of magnetic field-induced martensite reorientation in Ni_2MnGa single crystal

By the combination of the stress-induced and the magnetic field induced martensite reorientations, a cyclic reversible martensite reorientation can be realized by perpendicularly applying cyclic magnetic field and mechanical compressive stress as shown in Figure 1.4. Firstly, a constant compressive stress is applied along the vertical direction (*y* axis) to make the material in the initial state of single variant M_3 with its short axis along vertical direction (Figure 1.4(a)). Then a horizontal magnetic field (along *x* axis) is applied, and the material has no shape change when the magnetic field is small. With the increase of the magnetic field, the magnetic field-induced martensite reorientation will occur (Figure 1.4(b)) when the orientation criterion is satisfied: $\sigma_{mag} > \sigma_{comp} + \sigma_{tw}$, where σ_{mag} is the effective magnetic stress, σ_{comp} is the compressive stress and σ_{w} is the twinning stress (Heczko and Straka, 2004; Straka et al., 2006). A part of variant M_3 will transform to variant M_1 with the short axis along horizontal direction. With the further increasing of the magnetic field, all the material will change to variant M_1 with a large deformation strain of around 6% along the vertical direction (Figure 1.4(c)). Then, when the magnetic field is decreased to satisfy the criterion $\sigma_{comp} > \sigma_{mag} + \sigma_{tw}$ (Heczko and Straka, 2004; Zhang, 2018; Straka et al., 2006), the stress-induced martensite reorientation takes place (Figure 1.4(d)) and the material will return to M_3 variant with the short axis along vertical direction (Figure 1.4 (e)). Finally, a reversible deformation strain can be obtained by this process. Based on this mechanism, the Ni_2MnGa single crystal can provide high-frequency reservable strain when a high-frequency cyclic magnetic field is applied, which makes the Ni_2MnGa single crystals very promising for actuator applications. But the energy dissipation of the high-frequency reversible martensite reorientation increasing the specimen's temperature can trigger the phase transformation to influence the output strain (Chen and He, 2020; Zhang et al., 2018a, b; Zhang et al., 2020).

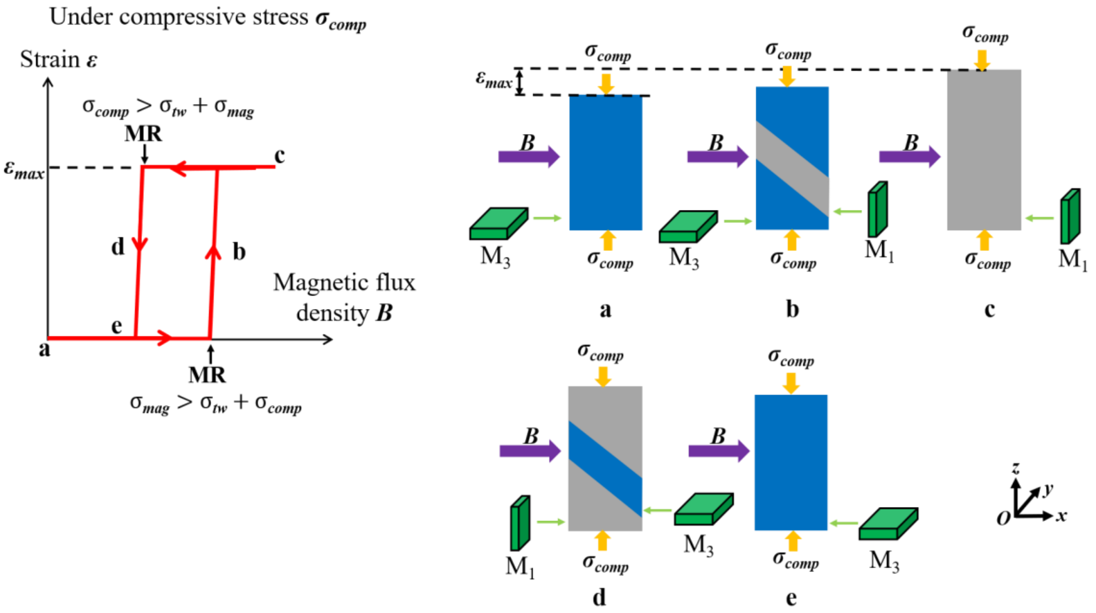

Figure 1.4 Schematic diagram of reversible martensite reorientation by perpendicular cyclic magnetic field and mechanical compressive stress

In summary, the stress-induced and the magnetic field-induced martensite reorientation have been well studied in the Ni_2MnGa single crystals, while the temperature is not expected to trigger martensite reorientation. However, my new experiments (Chapter 4) report a new phenomenon that the spontaneous detwinning without any external mechanical force or magnetic field can take place during the cooling-induced martensite phase transformation.

1.2.3 Phase transformation

The phase transformation between a high-symmetry phase (cubic austenite phase) and a low-symmetry phase (tetragonal martensite phase) can be induced by temperature, stress, magnetic field, or the combination of these fields in Ni_2MnGa single crystals.

1.2.3.1 Temperature (or thermal)-induced phase transformation

The Ni_2MnGa single crystals exhibit two phases under different temperatures: cubic austenite phase at high temperature and approximately “tetragonal” martensite phase at low temperature (Webster et al., 1984). As shown in Figure 1.1, the temperature-induced phase transformation from martensite to austenite by heating starts when the material temperature exceeds the A_s (austenite start temperature) and finishes when its temperature exceeds the A_f (austenite finish temperature). The different martensite variants can return to the original shape in the austenite phase upon heating (without other loadings), and this is the so-called “One-way shape memory effect”, which is a basic property of SMA. The temperature-induced phase transformation from austenite to martensite by cooling starts when the temperature of the material becomes smaller than the M_s (martensite start temperature) and finishes when its temperature is below the M_f (martensite finish temperature). The SMA polycrystals prefer to form multi-variants with different orientations to minimize the deformation energy during the cooling-induced martensite formation, leading to no macroscopic shape change in the SMA polycrystals, and this is the so-called “Self-accommodation effect”(Chai et al., 2009; Chulist et al., 2014; Miyazaki S. et al., 1989; Waitz, 2005; Waitz et al., 2008). However, whether the self-accommodation effect exists during the temperature-induced martensitic phase transformation in the SMA single crystals is still unclear in literature, and this will be one of the main topics of this thesis.

For another perspective, some SMAs can exhibit the “Two-way shape memory effect”: the material can “remember” two different macroscopic shapes respectively at high temperature (austenite phase) and low temperature (martensite phase) without any mechanical loadings. The two-way shape memory effect is not an inherent property of SMAs, but it can always be realized by training effects (e.g., thermo-mechanical training). (Guilemany and Fernandez, 1994; Lahoz at al., 2002; Masdeu at al., 2020; Yoo et Lee, 2011;). The origin of the two-way shape memory effect is usually due to the defects or the dislocations induced by the large strain of martensite phase during the repeated mechanical cycles. These defects or dislocations still exist during the heating process, and they will aide to form the same martensite during the cooling process, which will induce a large macroscopic shape change (Lexcellent at al., 2000).

1.2.3.2 Stress-induced phase transformation

The stress-induced phase transformation in Ni_2MnGa single crystals often happens for the materials in the initial state of austenite (Karaca et al., 2012; Kim et al., 2006), leading to the so-called “Pseudoelasticity (or Superelasticity”), which is another basic property of SMA. The stress-induced phase transformation is shown by the process “a” → “b” → “c” → “d” in Figure 1.5. The material is in austenite phase at the initial state when its temperature is above A_f. Then, applying a large mechanical stress can induce the phase transformation from austenite phase to a detwinned martensite with a large strain (up to 10%), i.e., the martensite variant(s) favored by the mechanical stress nucleates and grows. In contrary, unloading the mechanical stress can induce the martensite variant(s) to return to the austenite phase as shown by the process “d” → “e” → “f” → “a” in Figure 1.5.

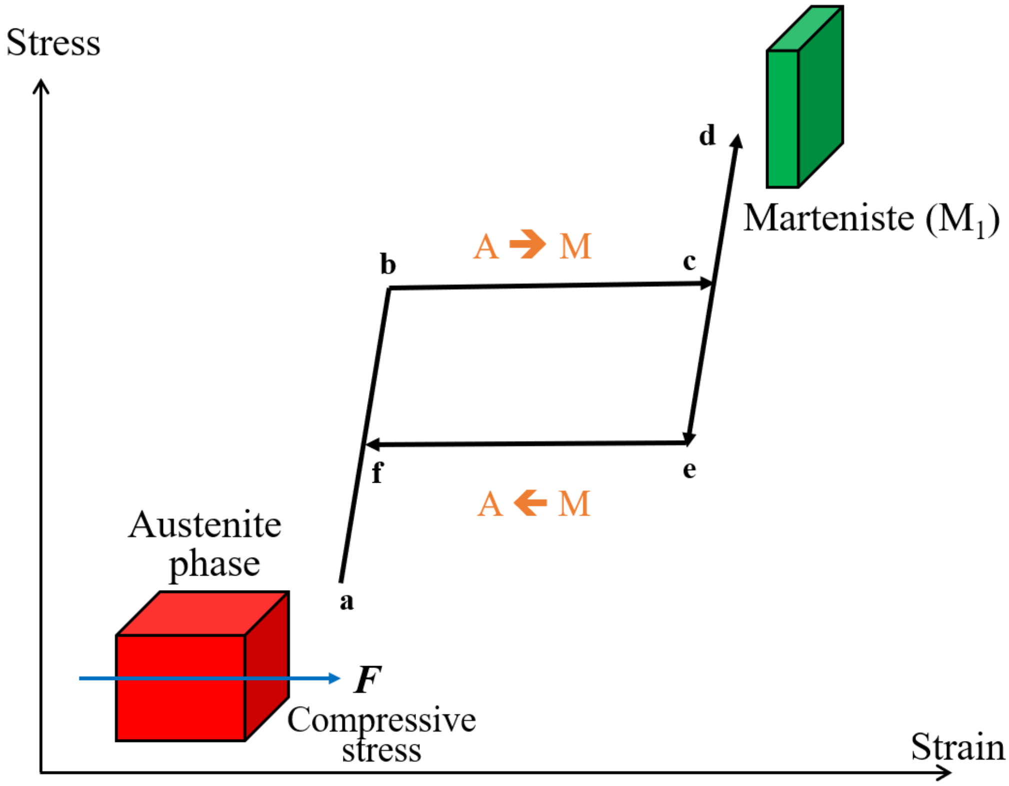

Figure 1.5 Schematic diagram of stress-induced phase transformation of Ni_2MnGa single crystal

1.2.3.3 Magnetic field-induced phase transformation

The magnetic field-induced phase transformation (and the associated magneto-caloric effect) in Ni_2MnGa single crystal is a significant research field because of its potential refrigeration application (Basso et al., 2012; Heczko et al., 2016). However, a very large magnetic field (> 7 Tesla) (Basso et al., 2012) to induce the phase transformation is hard to be satisfied. To overcome the limitations, current researches show that stress-assistant magnetic field-induced phase transformations are effective to reduce the needed magnetic field strength to 1~2 Tesla (Karaca et al., 2007; Karaman et al., 2006).

1.3 Motivations and objectives

Ni_2MnGa single crystal can take not only the martensite reorientation but also phase transformation under the thermal-magneto-mechanical driving forces. It is quite common that the martensite reorientation and phase transformation are regarded as two separate phenomena in Ni_2MnGa single crystal, but the recent experiments (Zhang et al., 2018b; Zhang et al., 2020) show that the high-frequency martensite reorientation always triggers the phase transformation from martensite to austenite phase which can influence the output strain amplitude. For better understanding the performances of high-frequency magnetic-field-induced martensite reorientation, the phase transformation should be considered simultaneously.

As the Ni_2MnGa single crystal exhibits austenite phase (only 1 cubic structure) in high temperature and martensite phase (3 pseudo-tetragonal variants) in low temperature, it is easy to identify the direct phase transformation process from martensite to austenite, but it is quite difficult to identify which variants or twins will nucleate or dominate during the reverse transformation process from austenite to martensite. Although the self-accommodated martensite structures have been observed in various SMA polycrystals (Chai et al., 2009; Chulist et al., 2014; Miyazaki S. et al., 1989; Waitz, 2005; Waitz et al., 2008), there is no experiment to verify the self-accommodation in SMA single crystals. Besides, the lack of the relevant experiment limits the theoretical modelling of the cooling-induced martensitic phase transformation in the SMA single crystal. For example, some theoretical researchers usually model the stress-free cooling-induced martensitic phase transformation in SMA single crystal by assuming “self-accommodation” (Seiner et al., 2008; Zhou et al., 2020), while others assume that the microstructure of austenite-twin (variant pair laminate of fine twin) is an energy minimizer, implying that cooling-induced phase transformation would not generate self-accommodation structure in SMA single crystals without constrains like grain boundary (Zhang et al., 2009). The contradictory modeling results are due to the lack of the clear experiments to demonstrate which microstructure will form during the stress-free cooling-induced martensitic phase transformation in SMA single crystals. So systematic experiments of temperature-induced phase transformation in SMA single crystals are highly demanded, which is also one of the main topics of this thesis.

In this work, we focus on the martensite variant evolution during the cooling-induced phase transformation by using different cooling methods and different specimens. Two adjacent lateral surfaces are observed by two optical cameras in order to conjecture the full-field evolution of the whole specimen in 3D, while an optical microscope is used to observe the detailed microstructures of the A-M interfaces during the temperature-induced phase transformation. The DIC technique (Digital Image Correlation) was used in the optical observation to trace the local strain evolution. A simple theoretical compatibility analysis combined with the local strain measurements can characterize the formation of the martensite variants/twins during the phase transformation and martensite reorientation.

The remaining part of this thesis is organized as follows: Chapter 2 describes the experimental setups for the two new sets of experiments: the high-frequency magnetic actuation test under different airflow conditions and the stress-free temperature-induced phase transformation test; Chapter 3 reports the systematic experiments on the strain amplitude modulation by utilizing compressed air passing through the FSMA specimen surface under a high-frequency magneto-mechanical loading system; Chapter 4 reports the temperature-induced phase transformation in free-standing FSMA bars without mechanical stress and magnetic field; Finally, Chapter 5 provides the general conclusions and perspectives.

Chapter 2

Experimental setup

This chapter describes the detailed setup of two different experiments of this thesis: the high-frequency thermo-magneto-mechanical coupling actuation system and the heating-cooling system for temperature-induced phase transformation of Ni_2MnGa single crystal.

2.1 Thermo-magneto-mechanical coupling actuation system

2.1.1 Experimental setup

The experimental setup of the high-frequency thermo-magneto-mechanical coupling actuation system is developed as shown in Figure 2.1(a) and (b). The whole actuation system is fixed on a damping grounded frame to prevent system vibrations. The electromagnet system (from Bouhnik) includes two cylindrical electromagnet poles (from SIGMAPHI) with a diameter of 25 mm, which are installed horizontally (along y-direction) with a 5 mm gap. An ac-electric current (up to 130 A and 500 Hz) is applied on the electromagnet coils to achieve a high-frequency magnetic field. A water-cooling system (with a water flow at 15 ^{o}C) surrounds the coils to avoid the temperature rise in the coils induced by the high frequency strong ac-electric current. This electromagnet system can provide a stable cyclic magnetic field with magnetic flux density between [-0.78, 0.78] Tesla and 500 Hz frequency for a long working time. A $Ni_{50}Mn_{28}Ga_{22}$ (at. %) single crystal specimen (from ETO Magnetic GmbH) with the dimension of 13×5×2 mm^3 is fixed inside the electromagnet poles with the long side (13 mm edge) along the vertical direction (x-direction). And it is clamped by two Plexiglas holders, which is made of non-magnetic material with a low-density and a low thermal conductivity. Above the upper Plexiglas holder, a spring compressed by a micrometer screw can apply a compressive force to the specimen along x-direction. The cyclic magnetic field and the compressive stress are perpendicular to each other, and are applied on the specimen by using this system. Thus, the interaction between the cyclic magnetic field (along y-direction) and the corresponding evolving compressive stress (from the spring along x-direction) eventually leads to a cyclic deformation strain of Ni_2MnGa single crystal by cyclic martensite reorientation. In this experimental system, during the magneto-mechanical cyclic loading, the ambient heat transfer efficiency of the specimen can be controlled by applying an ambient airflow of different velocities to pass through the specimen surfaces.

During the actuation, the deformation/nominal strain of the specimen along x-direction is measured by a laser displacement sensor (Keyence LK-H027) on the upper holder. The force along x-direction is measured by a force sensor (Kistler 9311B) fixed at the lower end of the lower Plexiglas holder. The global temperature of the specimen is monitored by a thermocouple (K-Type of sheath diameter of 0.5 mm) at the lower end of the specimen. A CMOS camera (Basler ac A2000-340 km) of 2048×1088 pixels with Nikkor lens is used to record the optical images of the specimen surface along z-direction. Based on the optical images, the Digital Image Correlation (DIC) software Vic-2D (Correlated Solutions) is used to obtain the local strain maps, which can help to determine the martensite variants.

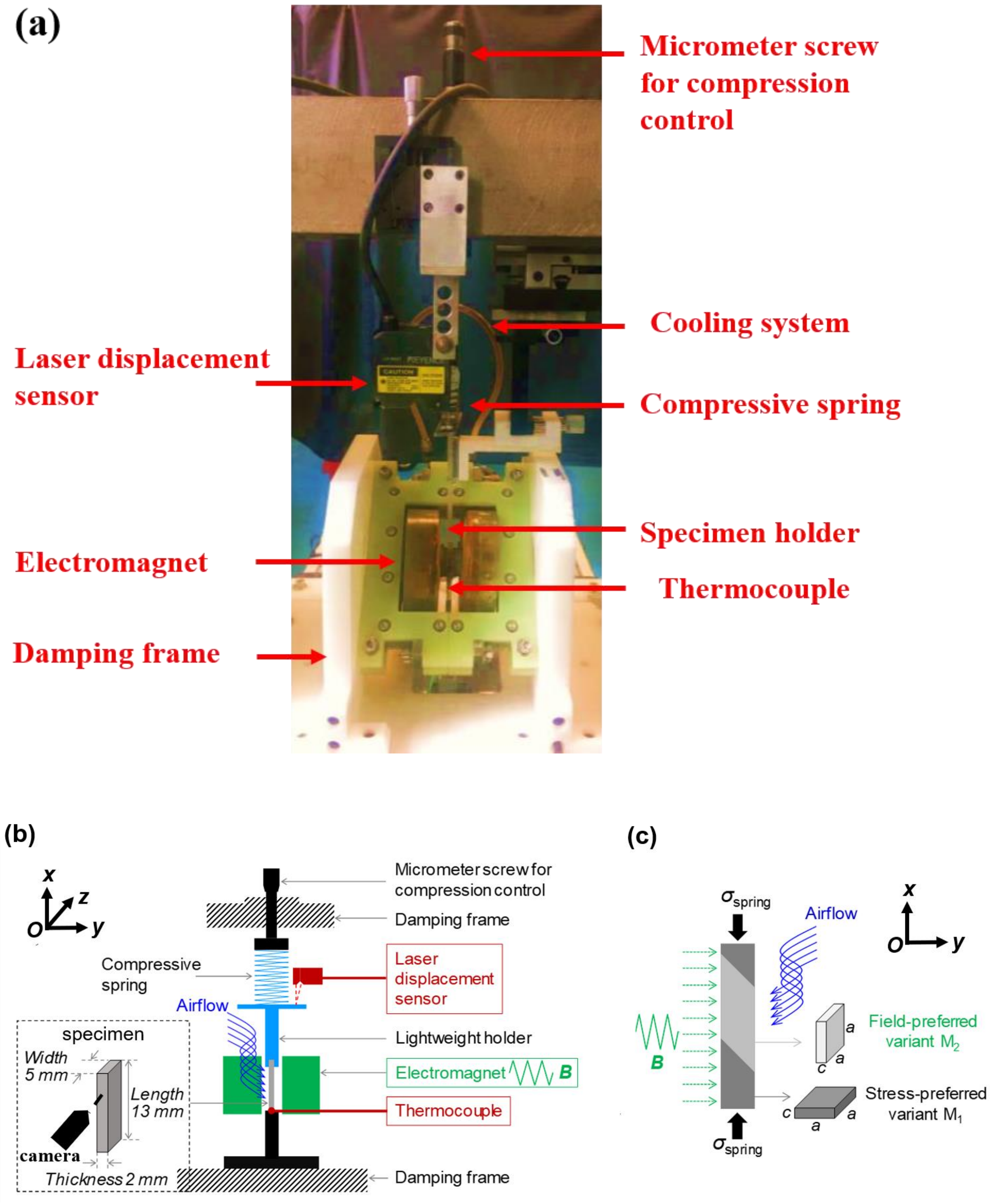

Figure 2.1 (a) Experimental setup of thermo-magneto-mechanical coupling actuation system of Ni_2MnGa single crystal; (b) Schematics of thermo-magneto-mechanical coupling actuation system; (c) Schematics of the magnified martensite reorientation

2.1.2 Ambient control

To investigate the ambient transfer effect, a compressed air (with controlled airflow velocity) is forced to pass through the specimen surface to control the heat transfer between the specimen and the ambient. The controlled airflow velocity can be measured by a portable airflow velocity indicator.

The heat transfer efficiency can be evaluated by a characteristic heat-relaxation time t_h, (He et al., 2010; He and Sun, 2010), which can be measured as follows: the specimen is first heated by the actuation of a high-frequency cyclic martensite reorientation, then the applied magnetic field is turned off and the relaxation of the specimen temperature is measured in a constant ambient airflow. In this case the temperature relaxation is only determined by the heat convection. The value of the heat-relaxation time t_h is obtained by fitting the experimentally measured temperature relaxation data to a heat-convection relaxation equation (He et al., 2010; He and Sun, 2010): $T = T_{\mathrm{ambient}} + (T_{\mathrm{initial}} - T_{\mathrm{ambient}}) \cdot e^{-\frac{t}{t_h}}$, where T_{initial} is the specimen temperature at time t = 0 s. For example, by using this method, the value of t_h at the ambient airflow velocity of 0 m/s (i.e., ambient still air) is determined to be 80.0 s in Figure 2.2. Similarly, t_h at different ambient conditions (different airflow velocity) can be experimentally measured.

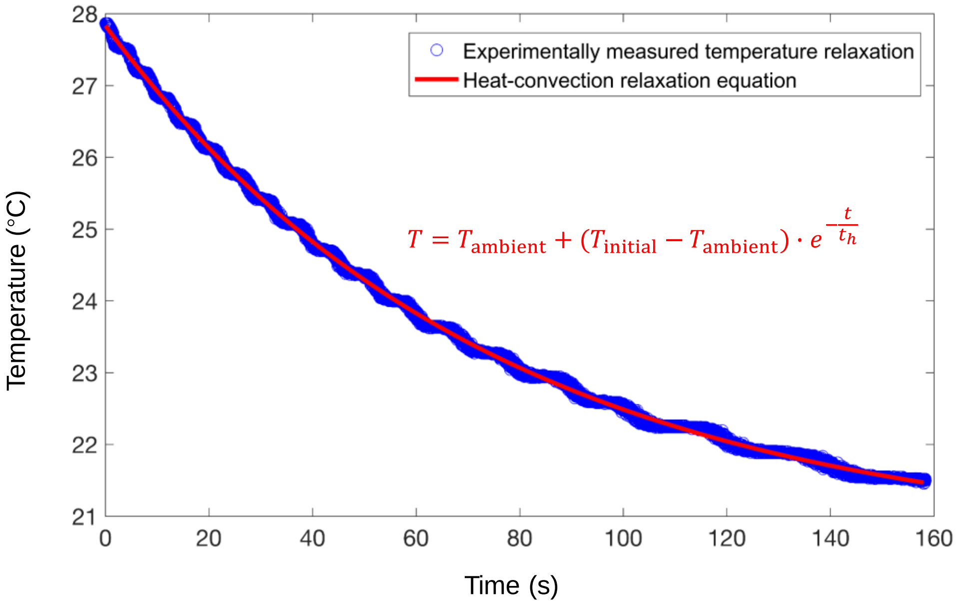

Figure 2.2 Measurement of the temperature relaxation time t_h of Ni_2MnGa single crystal specimen in still air ambient, where the characteristic heat-relaxation time t_h is fitted as 80.0 s.

2.2 Heating - cooling system for temperature-induced phase transformation

2.2.1 Experimental setup

The experimental setup of the heating and cooling system for temperature-induced phase transformation of Ni_2MnGa single crystal is shown in Figure 2.3 where a specimen is clamped horizontally (along *x*-direction) at one end while the other end is free to deform. An aluminum clamp manufactured in our lab is used to clamp the specimen and the heater (an electric iron) at the same time. The heater is used to heat the clamping end of the specimen by the heat conduction of the clamp. After the specimen is heated to induce the phase transformation from martensite to austenite, the specimen cools down to come back to martensite phase by two different ways: natural cooling mode (only switch off the heater) and ice local cooling mode (switch off the heater and then put a low-temperature ice (< 0°C) above the clamp) as shown in Figure 2.3(a) and (c) respectively. A thermocouple (K-Type of sheath diameter of 0.5 mm) is attached to the clamp to monitor the local temperature evolution at the clamping end of the specimen. To monitor the deformation of the specimen, two optical cameras (CMOS: acA2000-340km, Basler, Germany) equipped with a Nikkor lens are used to observe the specimen surfaces: the Camera 1 observes the specimen's top surface along *z*-direction, while the Camera 2 observes one of the side surfaces along *y*-direction. Based on these optical observations and the technique of Digital Image Correlation (DIC of the software VIC-2D), the local strain distributions (and in turn the distributions of the martensite variants) can be determined.

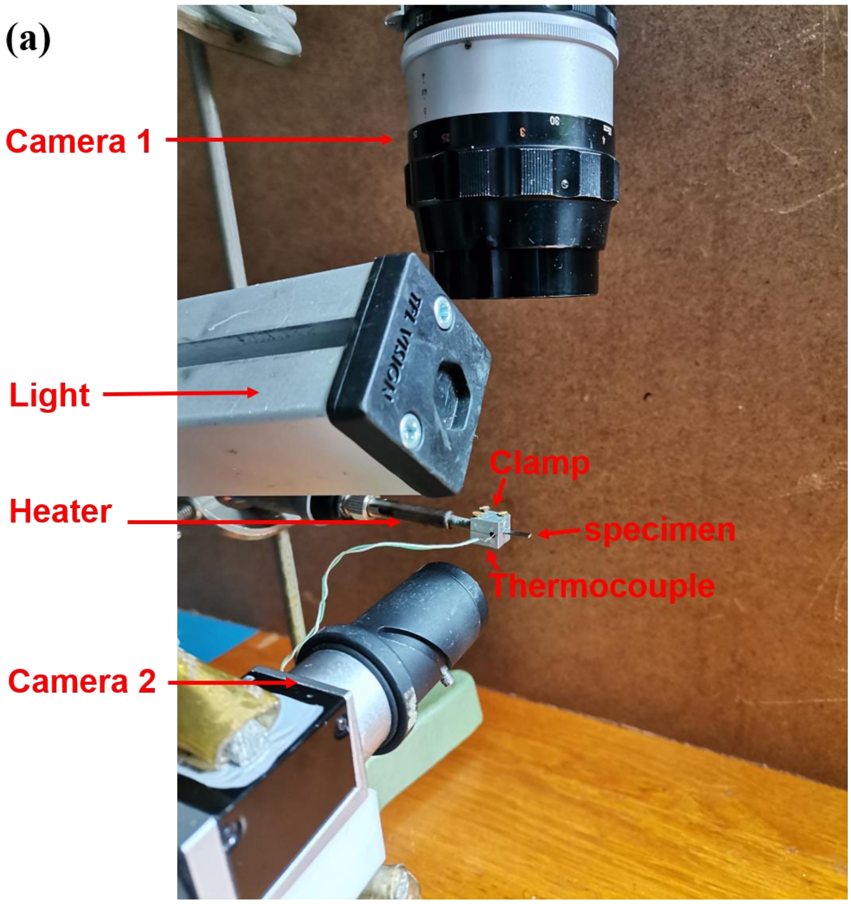
(a)
Camera 1
Light
Clamp
Heater
specimen
Thermocouple
Camera 2

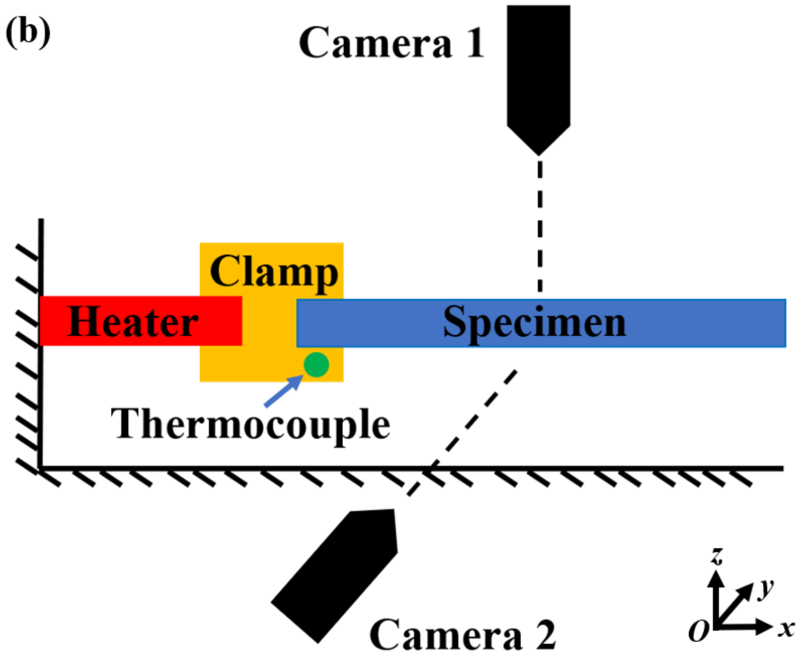
(b)
Camera 1
Clamp
Heater
Specimen
Thermocouple
Camera 2
z
y
O
x

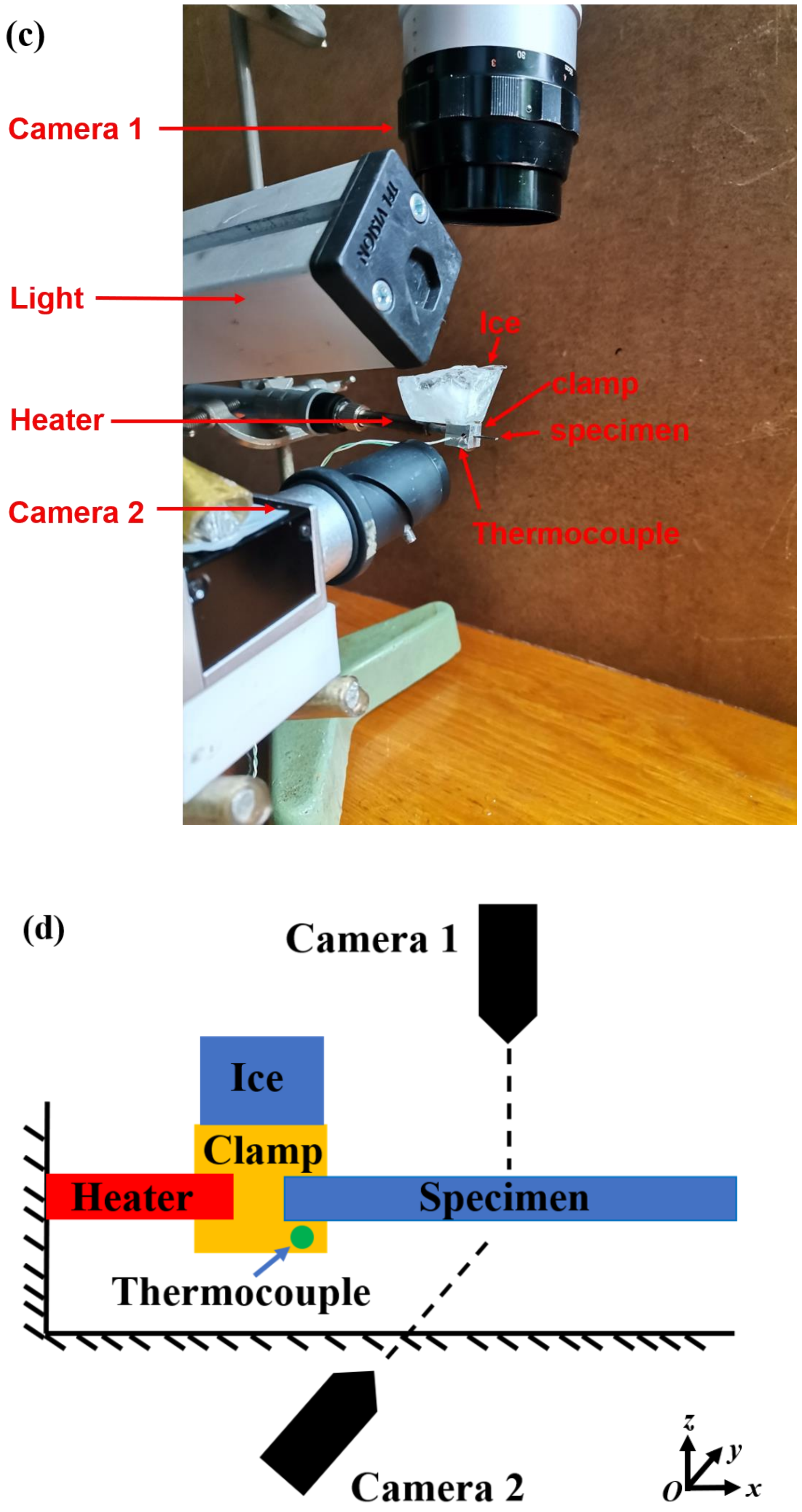

Figure 2.3 (a) Photo of the experimental setup of the heating and natural cooling system: a specimen is clamped at one end and the other end is free to deform; (b) Schematics of the heating and natural cooling system; (c) Photo of the experimental setup of the heating and ice cooling system: a piece of ice is put above the clamp; (d) Schematics of the heating and ice local cooling system.

The typical temperature evolutions measured by the thermocouple of the two different cooling modes are shown in Figure 2.4. The temperature of the specimen decreases slowly (temperature decreases to 30°C in about 600s) via the heat convection between the ambient and the whole specimen in the natural cooling mode as shown in Figure 2.4(a), while the temperature of the specimen decreases rapidly (temperature decreases to 30°C in about 10s) by the heat conduction through the clamp between the ice and the fixed end of the specimen as shown in Figure 2.4(b). Particularly, a period of natural cooling is necessary before the ice local cooling because this can reduce the ice consumption during the cooling process in the high temperature range (i.e., from the heating end temperature to the temperature well above the A_f).

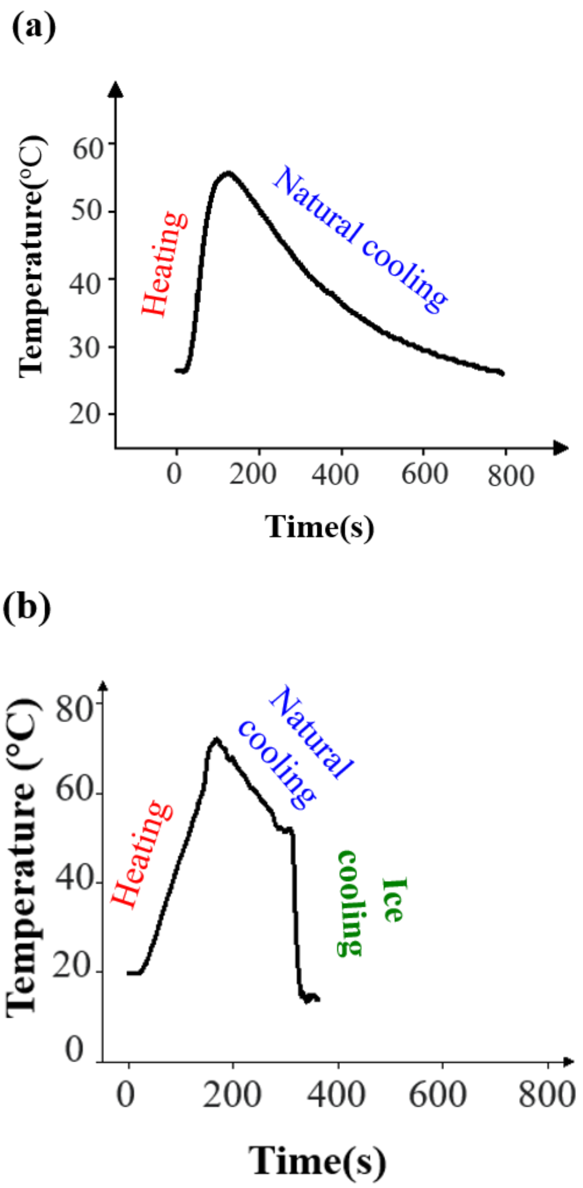

Figure 2.4 Temperature-time curves of the two different cooling modes: (a) Natural cooling; (b) Ice local cooling (A period of natural cooling is before the ice local cooling).

To observe the detailed deformation features of the Austenite-Martensite (A-M interfaces), an optical polarization microscope (AX70, Olympus, Japan) is used to observe the specimen's top surface along *z*-direction during the heating and cooling process as shown in Figure 2.5. The local strain distributions can also be determined by the technique of Digital Image Correlation (DIC software VIC-2D). The amplification of the microscope can be set from × 50 to × 1000.

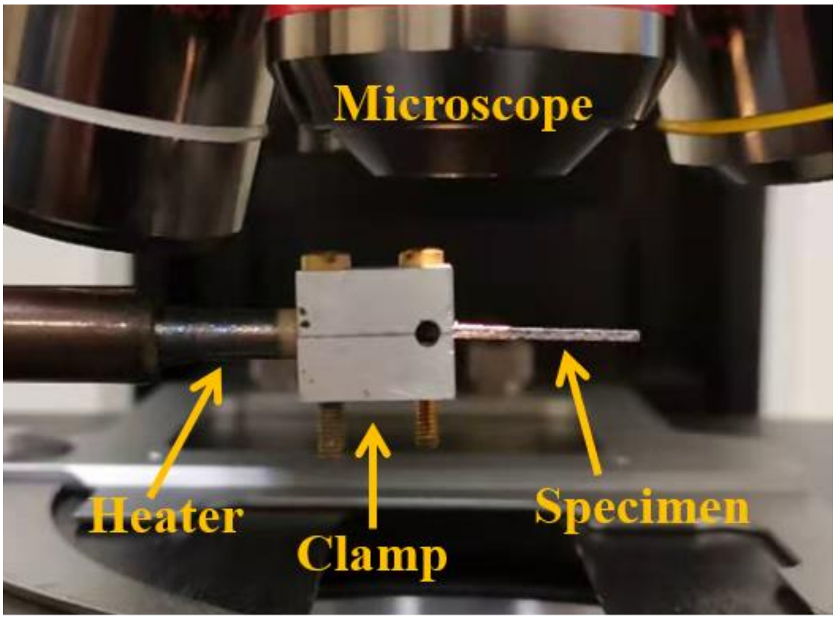

Figure 2.5 Detailed observation by the optical polarization microscope

2.2.2 Specimen preparation

Two types of $Ni_{50}Mn_{28}Ga_{22}$ (at. %) single variant rectangular bars (from ETO Magnetic GmbH) of different dimensions are tested. Both samples are in the state of 10M martensite phase at room temperature, with all faces of the specimens cut parallel to the {100} planes of the parent cubic austenite. The cross-sections of these two specimens are 2.5mm × 1mm (thin specimen) and 3mm × 2mm (thick specimen) respectively, and the gauge length after clamping for both specimens is around 10mm as shown in Figure 2.6.

(a) Thin specimen

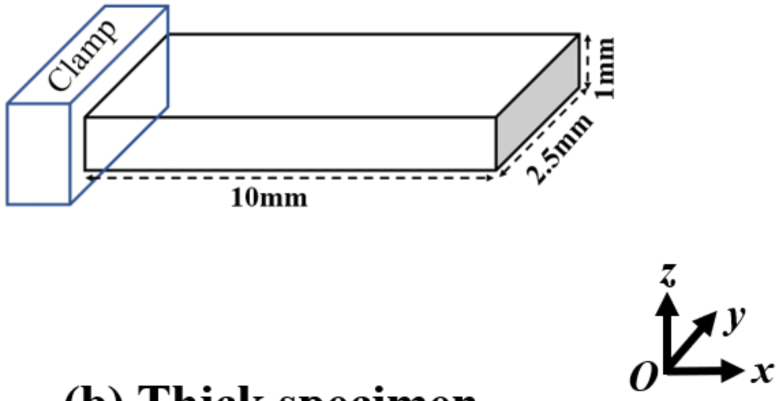

(b) Thick specimen

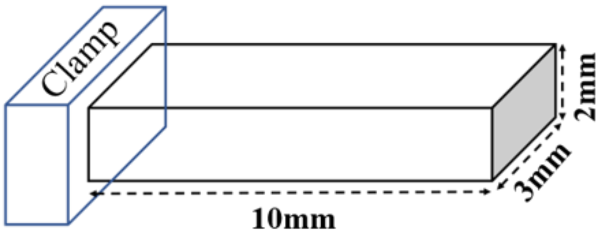

Figure 2.6 Schematic of two types of specimens: (a) thin specimen; (b) thick specimen.

Chapter 3

A thermal method for modulating the magnetic-field-induced strain oscillation

With proper magneto-mechanical driving forces (e.g., a high-frequency magnetic field plus a mechanical force), Ferromagnetic Shape Memory Alloy (FSMA) can provide a large cyclic deformation (strain oscillation amplitude up to 6%), which makes it a good candidate for high-frequency large-stroke actuators. Moreover, as a kind of shape memory alloys, FSMA's magneto-mechanical coupling behaviours are very sensitive to temperature, which allows researchers/engineers to modify (modulate) the strain oscillation amplitude for a wider range of applications by controlling the working temperature. This chapter reports systematic experiments on the strain amplitude modulation by a thermal method—utilizing compressed air (with controlled airflow velocity) passing through the FSMA specimen surface to control the heat transfer between the FSMA specimen and the ambient. It is found that the extremely weak or extremely strong ambient heat transfer can only have small strain oscillation amplitude while the maximum strain amplitude can be achieved only at a mild heat transfer condition (i.e., non-monotonic dependence of the strain amplitude on the ambient heat transfer). It is also demonstrated that the modulated strain amplitude is closely related to the working temperature, satisfying the balance between the heat generation (from the dissipative strain oscillation of the martensite reorientation) and the heat transfer to ambient (due to the temperature difference between the FSMA specimen and the ambient). With such understanding and constraints, three different schemes of modulating the strain amplitude by the thermal method are proposed and tested for their robustness/reliability. These results not only provide some guidelines/principles for designing FSMA actuators with flexible strain amplitude, but also demonstrate the delicate dynamics of the thermo-magneto-mechanical coupling that demand further theoretical/modelling study.

3.1 Introduction

Ferromagnetic Shape Memory Alloy (FSMA) is a smart material with multi-physics coupling as demonstrated by the large magnetic-field-induced deformation (up to 10% strain (Haldar and Lagoudas, 2018; Murray et al., 2000; Pagounis et al., 2014b; Seiner et al., 2014; Yu et al., 2018). When the magneto-mechanical driving forces are applied properly (satisfying some criteria) (Chen et al., 2013; Chernenko et al., 2004; He et al., 2011, 2012; Wang and Du, 2019), large cyclic recoverable deformation can be achieved (so-called superelasticity), making the material a good choice for large-stroke actuators. Particularly, the **large amplitude of strain oscillation** controlled by **high-frequency** magnetic field make FSMA unique candidate for advanced actuators (Kohl et al., 2014; Pagounis et al., 2014a; Techapiesancharoenkij et al., 2009; Yin et al., 2016) in comparison with other smart materials such as piezoelectric materials, magnetostrictive materials and traditional shape memory alloys. Several researchers have investigated the performance of the FSMA actuator prototypes and the associated magneto-mechanical governing parameters such as the magnetic-field frequency (Henry et al., 2002; Techapiesancharoenkij et al., 2009; Techapiesancharoenkij et al., 2008), the applied mechanical stress (Pascan et al., 2016; Pascan's thesis, 2015), and the system mechanical stiffness (Pascan et al., 2016; Pascan's thesis, 2015; Techapiesancharoenkij et al., 2011). In fact, besides these magneto-mechanical factors in governing the strain oscillation amplitude, there is another important factor: temperature, which is obvious when we examine the physical mechanisms of the magnetic-field-induced deformation of FSMA.

The large field-induced deformation of FSMA is caused from either the martensite reorientation with a magnetic field less than 1 Tesla (Haldar et al., 2014; Murray et al., 2000; Ullakko et al., 1996) or the martensitic phase transformation with a strong magnetic field larger than 2 Tesla (Haldar et al., 2014; Karaca et al., 2007). Due to the advantages of the relatively low loading field and the low hysteresis/dissipation (small twinning stress), the martensite reorientation is mainly adopted for the field-induced deformation of FSMA actuators. However, as recent studies revealed (Pascan et al., 2016; Pascan's thesis, 2015; Zhang et al., 2018a, b), although the twinning stress is low (0.2 MPa ~ 2 MPa), the dissipation heat fast accumulated during the high-frequency field-induced martensite reorientation can cause rapid temperature rise in FSMA, even triggering the phase transformation to significantly influence the output strain oscillation amplitude. Moreover, because the twinning stress is sensitive to temperature (particularly Type I twinning stress decreases with increasing temperature) (Straka et al., 2012), the temperature rise changing the twinning stress (i.e., changing damping capacity) can modify the strain oscillation during the actuation process of FSMA actuators. In other words, the temperature must be well controlled in order to achieve a reliable working state (a stable strain oscillation).

The recent experiments in our research group (Zhang et al., 2018a, b) utilized compressed airflow (controlling the airflow velocity) to pass through the surfaces of the FSMA specimen to tune the ambient heat transfer condition so to control the working temperature during the high-frequency strain oscillation. It was demonstrated that this thermal method can influence the temperature-govern processes (martensite reorientation and phase transformation) in both macroscopic behaviours (e.g., modifying the global output strain amplitude) and microstructure evolution (e.g., redistributing the volume fractions of different phases/variants). However, so far in literature, there is no accurate model for quantitative predictions on these thermo-magneto-mechanical coupling behaviours; even the basic design principles for FSMA actuators are not clear, for example, how to properly set thermal boundary condition to achieve the wanted stable working states?

This chapter firstly reports an experiment with gradually changing the ambient heat transfer condition (from ambient still air to strong ambient airflow) to systematically demonstrate the thermal effects on the strain oscillation and the associated working temperature. It is found that the extremely weak or the extremely strong ambient heat transfer can only have small strain oscillation amplitude while the maximum strain amplitude can be achieved only at a mild heat transfer condition (i.e., non-monotonic dependence of the strain amplitude on the ambient heat transfer). It is also demonstrated in this experiment that the strain amplitude can be modulated in a large range (from less than 2% strain amplitude to near theoretical maximum value 6% of the full martensite reorientation) and the working temperature is closely related to the modulated strain oscillation amplitude, which together satisfy the balance between the heat generation (from the dissipative strain oscillation of the martensite reorientation) and the heat transfer to ambient (due to the temperature difference between the FSMA specimen and the ambient). Further, another set of experiments with switching between two significantly different thermal conditions (i.e., the ambient airflow velocity changes largely and rapidly) was performed to verify the robustness/reliability of the dynamic transition between different working states. It was revealed that three qualitatively different types/schemes of the dynamic transitions can be identified, according to the participation and the relative importance of the two physical mechanisms in the dynamic transition (i.e., the temperature-dependent martensite reorientation and the temperature-induced phase transformation). Based on these dynamic experiments, some guidelines/principles of the thermal method for the strain-amplitude modulation are summarized and some challenging theoretical/modelling issues about the complicated multi-physics coupling dynamics are pointed out.

The remaining parts of this chapter are organized as the following. Section 3.2 describes the experimental procedures. Section 3.3 reports the results of the two sets of experiments (gradual transition and rapid/dynamic transition) and the associated theoretical thermal analysis and discussion. Finally, a summary is given in Section 3.4.

3.2 Material properties and Experiment setup

A $Ni_{50}Mn_{28}Ga_{22}$ (at. %) single crystal FSMA specimen (from ETO Magnetic GmbH) was used in the experiments of this study. The specimen was cut to a rectangular bar with all faces of the specimen parallel to the {100} planes of the parent cubic austenite (with a lattice parameter of a_0). The total length of the specimen L_{total} is 13 mm and the sectional area is 5×2 mm^2. The specimen is in the state of 10M martensite phase at room temperature. Note that the martensite variants are slightly monoclinic in this material, but in this work it is assumed that they are tetragonal with two long axes "*a*" and one short axis "*c*" for the simplicity of the analysis. The material characteristic phase transformation temperatures M_s, M_f, A_s and A_f were obtained as 38.6 °C, 36.3 °C, 44.8 °C and 46.8 °C respectively from a Differential Scanning Calorimetry (DSC) test.

To experimentally investigate the FSMA actuator performances, a thermo-magneto-mechanical loading system is developed as shown in Figure 2.1 (a) and (b) in last chapter. Before each test, the martensite specimen is fully compressed along *x*-axis (by applying a large mechanical compression stress, larger than 10 MPa) to obtain a single variant state with the short-axis (*c*-axis) along *x*-direction (so-called stress-preferred variant, shown as M_1 in Figure 2.1 (c)), so that all the tests can take the same reference state (i.e., zero strain) for calculations of the specimen deformation strain in this work. The specimen is installed between two magnetic poles with the long side along *x*-direction by two lightweight plexiglass holders. At the beginning of each test, an initial compressive stress σ_{ini} is applied on the specimen along *x*-direction by a compressed spring. Then a magnetic field (with magnetic flux density $\boldsymbol{B}$ cyclically varying between [-0.78, 0.78] Tesla with a triangular waveform) of frequency f_{mag} is applied horizontally by the electro-magnet to drive the martensite reorientation from M_1 to M_2 (so-called magnetic field preferred variant with the short axis along *y*-direction and the long axis *a* along *x*-direction) as shown in Figure 2.1 (c). During this martensite reorientation process, the length of the specimen gauge-section L_{gauge} (the gauge section is the part of the specimen between the upper and lower holders/clampers, initially L_{gauge} = 6.7 mm) changes due to the microscopic difference between lattice parameters *a* (for M_2) and *c* (for M_1) along *x*-direction, which causes the change in the spring length so that the spring compressive stress along *x*-direction changes at the same time. Thus, the interaction between the cyclic magnetic field (along *y*-direction) and the correspondingly evolving compressive stress (from the spring along *x*-direction) eventually leads to a cyclic deformation strain of FSMA (by cyclic martensite reorientation between the variants M_1 and M_2). In this experimental system, during the magneto-mechanical cyclic loading, the ambient heat transfer efficiency of the FSMA specimen can be controlled by applying an ambient airflow of different velocities to pass through the specimen surfaces.

During the actuation, the deformation of the specimen along *x*-direction is measured by a laser displacement sensor (Keyence LK-H027) at the upper holder, and the average temperature of the specimen is monitored by a thermocouple (K-type, 0.5 mm sheath diameter) at bottom of the specimen. Because the specimen holders are made of plexiglass of low thermal conductivity to reduce the heat conduction from the specimen ends to the fixtures, it is assumed that the heat convection via the specimen surface is the dominant path of the heat exchange rather than the heat conduction via the specimen ends. The heat transfer efficiency can be quantified by a characteristic heat relaxation time t_h which depends on the ambient airflow velocity (the details about the measurement of t_h can be found in Figure 2.2 and the associated test in last chapter). That means, a large airflow velocity leads to a high heat transfer efficiency corresponding to a short characteristic heat relaxation time t_h.

3.3 Experimental results and discussions

This section is divided into three subsections. In order to demonstrate the thermal effect on the magnetic-field-induced strain oscillation in FSMA, a test of high-frequency magnetic actuation with stepwise increasing heat transfer efficiency (increasing the velocity of ambient airflow) is reported in Subsection 3.3.1. To understand the physical mechanisms and the associated governing parameters on the thermal effect, a simple thermal analysis considering the heat balance are conducted in Subsection 3.3.2. Finally, based on the understanding, we design and test three typical schemes to modulate/control the output strain amplitude in Subsection 3.3.3, as examples to demonstrate the reliable thermal method to control the strain oscillation.

3.3.1 Ambient heat transfer effect on magnetic-field-induced strain oscillation

To investigate the heat transfer effect on the FSMA's high-frequency strain amplitude, a magnetic actuation test is conducted under a stepwise increasing heat transfer efficiency (applying an airflow passing through the specimen with gradually increasing velocity in several small steps). The frequency of the applied magnetic field (f_{mag}) is 110 Hz (accordingly the strain oscillation frequency $f_{strain} = 2\ f_{mag} = 220$ Hz), and the applied initial compressive stress (σ_{ini}) is 0.4 MPa. The strain and the temperature evolutions of the FSMA are shown in Figure 3.1(a) and the magnified views on the strain oscillation curves at some typical time instants are shown in Figure 3.1(b). It is seen that, at the beginning of the actuation (< 26 seconds) where the specimen is in the still air ambient (whose characteristic heat relaxation time t_h is 80.0 seconds as measured in last chapter), a large strain amplitude $\Delta\varepsilon$ (the strain difference between the maximum and the minimum nominal strains) around 6% can be obtained. At the same time, the specimen temperature increases from the room temperature (around 20 °C) to 37.8 °C which is within the range of the martensitic phase transformation (i.e., 36.3 °C = $M_f < T_{specimen} < A_f$ = 46.8 °C). Then, at around $t \approx 27$ s, a significant reduction in the strain amplitude occurs: $\Delta\varepsilon$ decreases from 6% to around 1.9%. This sudden strain reduction (so-called strain drop marked by a red arrow in Figure 3.1(a)) is caused by the martensite-to-austenite phase transformation induced by the temperature rise; with the in-situ observation on the specimen surface by an optical camera, we can see the appearance of a large non-active zone (of austenite phase which does not provide any cyclic deformation in such magnetic field) as shown in the schematics in Figure 3.1(b) at the time instant $t_1 \approx 40$ s. Detailed verification, analysis and discussion on the M→A phase transformation during the magnetic-field induced martensite reorientation can be found in the previous studies of my research group (Zhang et al., 2018a, b; Chen and He, 2020). After the strain drop, both the output strain amplitude $\Delta\varepsilon$ and the specimen temperature T reach stable states with the strain amplitude of 1.9% and the temperature of 37.8 °C as shown in the evolutions at the time instant t_1 in Figure 3.1; particularly, it is seen in the schematics of Figure 3.1(b) about the phase/variant distributions at the instant t_1 that only a part of the specimen cyclically changes between the M_1 and M_2 martensite variants during the cyclic magnetic field loading, while the rest part is austenite (non-active zone). In other words, during the strain drop, the specimen self-organizes its microstructure into different parts: the active part (providing cyclic deformation) and the non-active part (without contribution to output strain amplitude). The reason for such self-organization, and the mechanisms determining the volume fractions of the different parts will become clear in the following further tests and the analysis in Subsection 3.3.2.

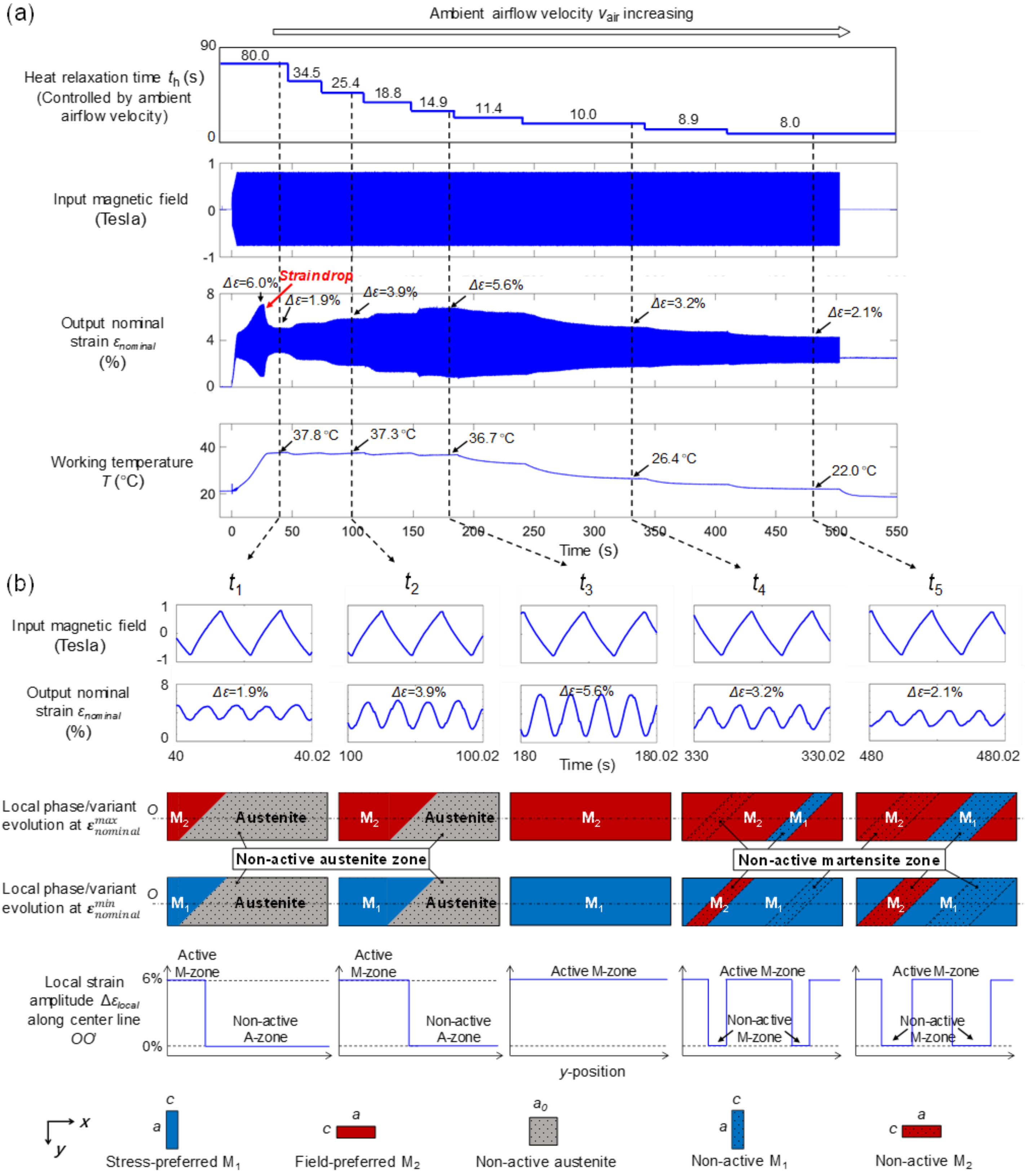

Figure 3.1 (a) The strain and temperature responses of FSMA under gradually increasing airflow velocity (i.e., gradually reducing the ambient heat relaxation time t_h); (b) the magnified views on the input magnetic field and the output strain evolutions and schematics of the local phase/variant evolutions at 5 typical time instants ($t_1 \sim t_5$).

As shown in Figure 3.1(a), when the characteristic heat relaxation time t_h is stepwise decreased from 80.0 s to 14.9 s (at the time instant t_3), the strain amplitude increases stepwise from 1.9% to 5.6%, nearly reaching the theoretically maximum strain amplitude (6%); at the same time the stepwise temperature change is slight (only 1.1 °C reduction from the instant t_1 to t_3 in Figure 3.1(a)). Such thermal effect on the output strain amplitude can be understood by the schematics of the evolutions of the phase/variants at the peak and valley of the deformation cycles (strain oscillations) at some typical instants (t_1~t_5) in Figure 3.1(b). For example, in comparison of the phase/variant distributions between the instants t_1 and t_2, the volume of the non-active Austenite zone is smaller at t_2; that is why the output strain amplitude becomes larger at t_2 (larger Martensite active zone taking cyclic reorientation between variants M_1 and M_2)—the higher efficiency (shorter t_h) of the heat transfer to ambient allows more dissipative Martensite reorientation process. Another key point is the slight temperature change: 37.8 °C to 37.3 °C from t_1 to t_2; both the temperature levels are within the range of the martensitic phase transformation, $M_f < T_{specimen} < A_f$, which allows the coexistence of both phases: Martensite and Austenite. In other words, according to the heat transfer condition (the level of t_h), the FSMA specimen adjusts its volume fractions of the two phases (the non-active Austenite without local strain oscillation and the active Martensite with 6% local strain oscillation amplitude) for the balance between the dissipation heat generated by the dissipative martensite reorientation (dissipative strain oscillation) and the heat transfer to ambient due to the temperature difference between the specimen and the ambient.

When the ambient heat transfer efficiency is high enough (i.e., t_h is short enough) as at the instant t_3 in Figure 3.1, the specimen is almost fully transformed into Martensite which takes a complete cyclic reorientation between M_1 and M_2 to provide a large output nominal strain amplitude of 5.6%. However, when the heat relaxation time t_h is further stepwise decreased to 8.0 s (at the time instant t_5), both the strain amplitude and the temperature decrease significantly as shown in Figure 3.1(a), where $\Delta\varepsilon$ = 2.1% and $T_{specimen}$ = 22.0 °C. This thermal effect on the strain amplitude is due to the temperature dependence of the martensite reorientation process: when the ambient heat transfer is strong (stronger than the dissipation heat generation of the martensite reorientation), the specimen temperature decreases significantly below M_f (e.g., T = 26.4 °C at t_4), making the martensite reorientation more difficult to proceed because the dissipative force (resistant force, so-called twinning stress) of the martensite reorientation increases with decreasing temperature as experimentally investigated in literature (Straka et al., 2012; Sozinov et al., 2016). In other words, the higher damping (higher dissipation) in the dynamic oscillating system leads to the lower output oscillation amplitude. In this case, even though the specimen is fully occupied by Martensite in the low temperature (lower than M_f), not all the Martensite zones are active. As shown in the schematics of t_4 and t_5 in Figure 3.1(b), some Martensite zones are non-active, always staying in the state of M_1 or M_2, without local strain oscillation. In comparison between the time instants t_4 and t_5, we can see that the output strain amplitude decreases from 3.2% to 2.1% with the increase in the volume fraction of the non-active Martensite zones.

The above thermal effects on the strain oscillation amplitude and the associated temperature are summarized in Figure 3.2 which indicates the dependences of the step-stable strain oscillation amplitude and the associated temperature on the characteristic heat relaxation time t_h. It is seen that, with decreasing t_h (i.e., increasing ambient airflow velocity), the stable strain amplitude $\Delta\varepsilon_{stable}$ changes non-monotonically while the stable temperature T_{stable} decreases monotonically. The maximum output strain is obtained at around t_h = 14.9 s where the temperature starts to decrease below M_f. That means, to achieve the maximum output strain amplitude, a proper ambient heat transfer condition is needed to tune the specimen working temperature close to (but lower than) the phase transformation temperature (M_f) so that the whole specimen is occupied by Martensite phase and the temperature-dependent twinning stress (dissipative force) is relatively low.

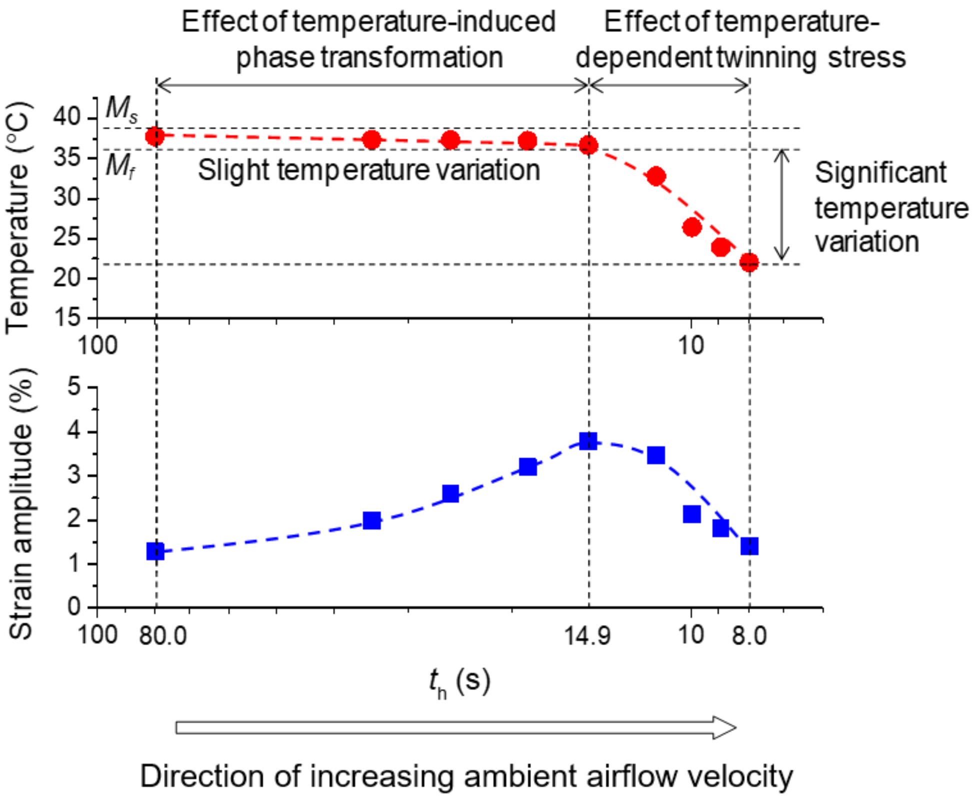

Figure 3.2 The dependence of the stable strain amplitude and the stable temperature of FSMA on the characteristic ambient heat relaxation time t_h. The dashed lines are for guiding eyes.

Taking the optimal t_h (=14.9 s for the maximum $\Delta\varepsilon_{stable}$) as a reference point, Figure 3.2 clearly indicates two different regions of the thermal effect: weak heat transfer condition ($t_h >$ 14.9 s) and the strong heat transfer condition ($t_h <$ 14.9 s). In the region of weak heat transfer, the temperature is always within the range of the phase transformation temperatures ($M_f < T_{specimen} < M_s$), and the strain amplitude is modulated/modified mainly by the self-adjustment of the volume fractions of the active Martensite and the non-active Austenite via the A↔M phase transformation. By contrast, in the region of strong heat transfer, the specimen temperature is below M_f and the amplitude modulation is due to the temperature dependence of the dissipative resistant force (twinning stress) of the martensite reorientation. Therefore, the overall thermal effect on the strain amplitude modulation is due to two mechanisms (the phase-fraction adjustment and the temperature dependence of twinning stress) whose contributions and relative importance depend on the specimen working temperature (above or below M_f). Nevertheless, the strain amplitude modulation by the two mechanisms of the thermal effect need to satisfy the heat balance: the balance between the dissipation heat generated by the dissipative martensite reorientation and the heat transfer to ambient, which are quantified and discussed in next subsection.

3.3.2 Simple thermal analysis

The heat balance of shape-memory-alloy structures has been well studied in literature (Zhang et al., 2018 a; He et al., 2010; He and Sun, 2010 a, b), based on which a simple thermal model for current FSMA system can be obtained as the following (detailed derivation can be found in Appendix A):

$$\frac{dT}{dt} = \frac{q_{Dissipation} - q_{Transfer}}{\lambda} \tag{1a}$$

where

$$q_{Dissipation} = 2\sigma_{tw} \cdot \Delta\varepsilon_{stable} \cdot f_{strain} \tag{1b}$$

$$q_{Transfer} = \frac{(T - T_0) \cdot \lambda}{t_h} \tag{1c}$$

Equation (1a) means that changing rate of the specimen temperature (T) is proportional to the net heat rate (the difference between the dissipation heat generation rate $q_{Dissipation}$ and the ambient heat transfer rate $q_{Transfer}$ (unit: $\text{J}\cdot\text{m}^{-3}\cdot\text{s}^{-1}$)) and is inversely proportional to the material's specific heat λ (unit: $\text{J}\cdot\text{m}^{-3}\cdot\text{K}^{-1}$); Eq. (1b) indicates that the dissipation heat generation rate $q_{Dissipation}$ due to the martensite reorientation is 2 times the product of the twinning stress σ_{tw}, the strain amplitude $\Delta\varepsilon$ in one oscillation cycle and the frequency of the strain oscillation (i.e., cycle number per second); Eq. (1c) shows that the heat transfer rate to ambient $q_{Transfer}$ is proportional to the material's specific heat and the temperature difference between the specimen (T) and the ambient (T_0), and is inversely proportional to the characteristic heat relaxation time t_h.

It is seen from Eq. (1a) that, when $q_{Dissipation} > q_{Transfer}$ (or $q_{Dissipation} < q_{Transfer}$), the specimen temperature T increases (or decreases). Only when $q_{Dissipation} = q_{Transfer}$, the system reaches stable states, i.e.,

$$2\sigma_{tw} \cdot \Delta\varepsilon_{stable} \cdot f_{strain} = q_{Dissipation} = q_{Transfer} = \frac{(T_{stable} - T_0) \cdot \lambda}{t_h} \tag{2}$$

In Eq. (2), all the parameters at the most right-hand and the most left-hand sides can be directly measured except the twinning stress σ_{tw}. According to the previous studies in literature (Murray et al., 2000; Techapiesancharoenkij et al., 2009; Henry et al., 2002; Ullakko et al., 1996), the martensite reorientation occurs via the motion of the twin boundaries of two different types (so-called Type I and Type II) with different twinning stresses denoted by $\sigma_{tw}{}^{I}$ and $\sigma_{tw}{}^{II}$, among which, only $\sigma_{tw}{}^{I}$ depends on temperature (Straka et al., 2012):

$$\sigma_{tw}{}^{I} \approx 0.2 - 0.04 \cdot (T - A_s) \qquad \text{MPa} \tag{3a}$$

$$\sigma_{tw}{}^{II} \approx 0.2 \qquad \text{MPa} \tag{3b}$$

where A_s denotes the austenite starting temperature of the phase transformation. Our previous study (Pascan's thesis, 2015; Pascan et al., 2015) demonstrated that both types of twin boundary motions contribute to the FSMA dynamic deformation; so the effective twinning stress σ_{tw} should include the contributions of both $\sigma_{tw}{}^{I}$ and $\sigma_{tw}{}^{II}$ as:

$$\sigma_{tw} = \nu \cdot \sigma_{tw}{}^{I} + (1-\nu) \cdot \sigma_{tw}{}^{II} \tag{4}$$

where ν denotes the fraction of Type I twin boundary motion contributing to the dynamic deformation. As Type II twin boundary motion is easier than Type I twin and plays a more important role in the temperature rise of the dynamic actuation (Pascan et al., 2015), ν is assumed to be a small value here ($\nu = 0.1$). Therefore, combining Eqs. (3) and (4) and the measureable parameters/variables ($\Delta\varepsilon_{stable}$, T_{stable}, T_0, λ, f_{strain}, and t_h.), we can quantify the step-stable rates of the dissipation heat generation and the heat transfer to ambient to verify the heat balance of Eq. (2) as shown in Figure 3.3(a). It is seen that the heat balance is satisfied quite well, keeping in mind that there might be some errors in the temperature measurement as the temperature sensor (thermocouple) is attached at the specimen's end rather than direct contact to the gauge section (the middle part of the specimen), and that some minor heat generation due to eddy current generated by high-frequency magnetic field has been ignored, which were experimentally measured and discussed in literature (Pascan et al., 2016; Zhang et al., 2018 a).

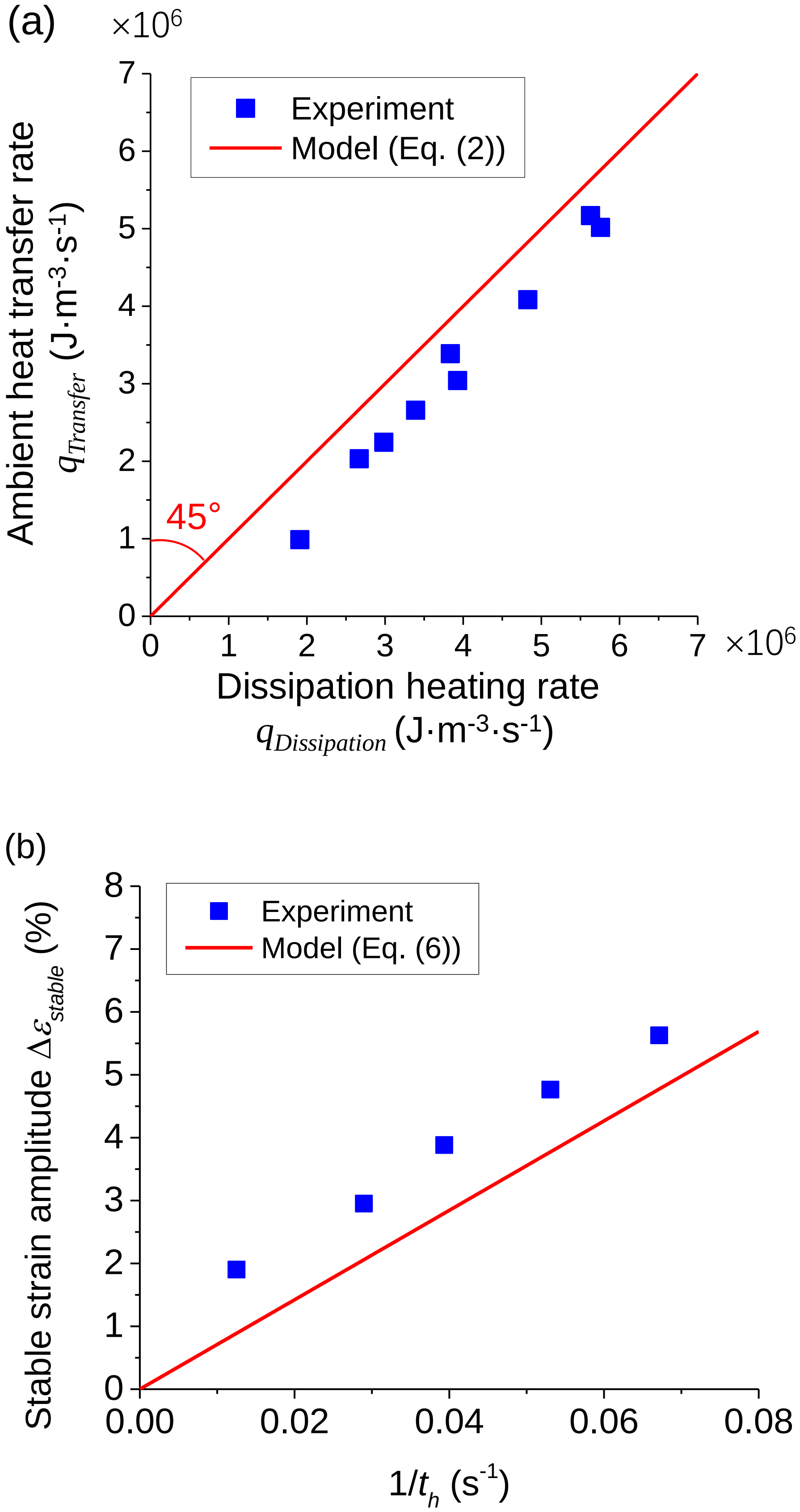

Figure 3.3 (a) Comparison between the experimental results and the heat balance model Eq. (2) (the red line); (b) Comparison of the strain amplitude $\Delta\varepsilon$ versus $1/t_h$ between experiment and theoretical model (Eq. (6)).

So, we can utilize this balance equation to estimate strain amplitude modulation, such as the relation between the strain amplitude $\Delta\varepsilon$, working temperature T and the characteristic heat relaxation time t_h. For example, in the region of weak heat transfer ($t_h > 14.9$ s) in Figure 3.2, the specimen temperature is very close to M_f, i.e.,

$$T_{stable} \approx M_f \tag{5}$$

Combining Eqs. (2) ~ (5), we have

$$\Delta\varepsilon_{stable} = C \cdot \frac{1}{t_h} \tag{6}$$

where

$$C = \frac{(M_f - T_0) \cdot \lambda}{2 f_{strain} \cdot \left[0.2 - 0.04 \cdot \nu \cdot (M_f - A_s) \right]}$$

Equation (6) of the simple inversely proportional relation well captures the t_h-dependence of the strain amplitude as shown in Figure 3.3(b).

However, it is noted that the heat balance equation (Eq. (2)) alone can not predict the two response variables (T_{stable} and $\Delta\varepsilon_{stable}$) without a mechanical force balance equation considering the magneto-mechanical driving forces and the dynamic inertial effect. So, a complete model on the dynamic strain oscillation of the FSMA is still demanded and it is a challenging task involving the complicated non-smooth processes, such as the martensite reorientation with dissipative twinning stress (like dry friction) and the A-M phase transformation with thermo-mechanical coupling. Nevertheless, the heat balance equation is helpful in understanding the thermal effects, particularly the relation between T_{stable} and $\Delta\varepsilon_{stable}$ as shown in Figure 3.4 which is discussed and utilized to design some reliable schemes/methods for the strain amplitude modulation in next subsection.

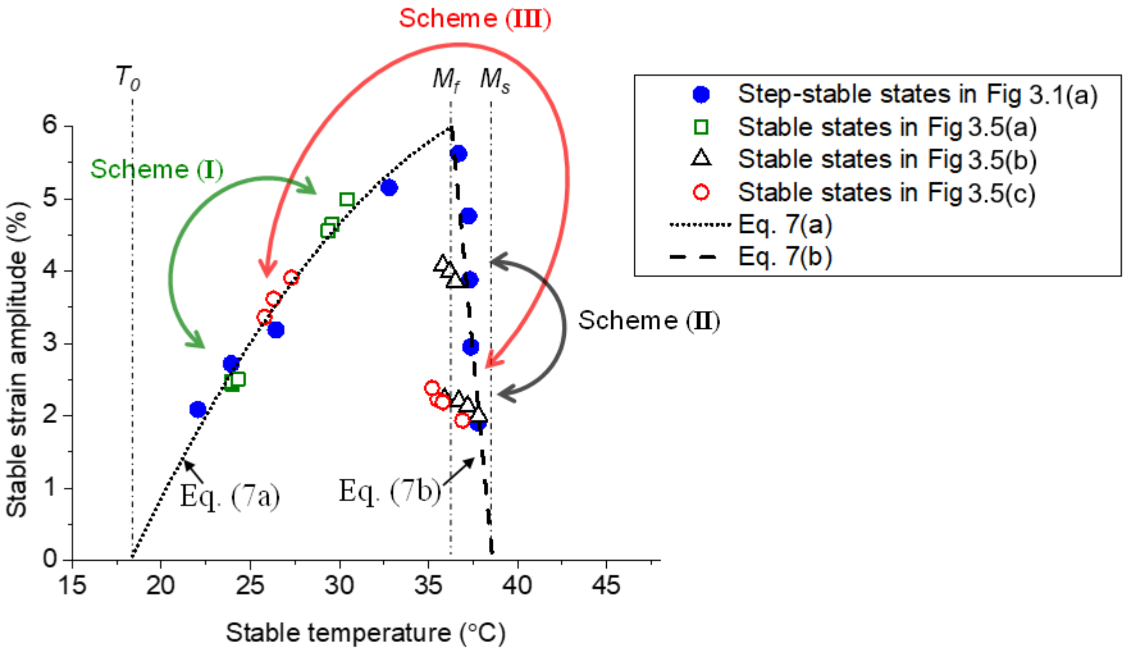

Figure 3.4 The working states with certain relations between the stable strain amplitude and the stable temperature in a given magneto-mechanical loading condition (f_{mag}=110 Hz and σ_{ini}= 0.4 MPa) with varying ambient heat transfer efficiency. The Eqs. 7(a) and 7(b) are respectively plotted as black dotted and dashed lines. The blue solid circles are from the step-stable states in Figure 3.1(a); the green open squares, the black open triangles and the red open circles are the results of the cyclic stable-state transitions of the Schemes (I), (II) and (III) as shown in Figure 3.5(a), (b) and (c), respectively.

3.3.3 Typical schemes of strain amplitude modulation

Based on the summarized thermal effect in Figure 3.2 we can plot Figure 3.4 to show the FSMA's working states (the stable strain amplitude and the corresponding working temperature) under the given magneto-mechanical loading (whose key parameters f_{mag} =110 Hz and σ_{ini} = 0.4 MPa in current test). Figure 3.4 implies that the output strain amplitude $\Delta\varepsilon$ can vary in a wide range from a small value (near 0%) to near the theoretical maximum value of martensite reorientation (close to 6%), and the working temperature T is within the range from T_0 (the ambient airflow temperature around 18 °C) to the characteristic temperature M_s of the martensitic phase transformation.

But FSMA can not work at any arbitrary combinations of $\Delta\varepsilon$ and T, i.e., the working state must satisfy certain relations between $\Delta\varepsilon$ and T. For example, when $T < M_f$, the strain amplitude $\Delta\varepsilon$ significantly increases with increasing temperature T because the dissipative twinning stress (resistant force) decreases with increasing T (and no phase transformation involvement below M_f). By contrast, when the temperature is above M_f, the strain amplitude modulation is accompanied with only slight temperature change via the phase-fraction adjustment by phase transformation (note: theoretically, the martensite volume fraction can change from 0% to 100% for the martensitic phase transformation within the small temperature difference $M_s - M_f$ = 38.6 °C – 36.3 °C = 2.3 °C like in the DSC test). Therefore, by proper ambient airflow control (changing t_h), the output strain amplitude can be modulated from 0% to 6% at both the temperature ranges, $[T_0, M_f]$ and $[M_f, M_s]$. In other words, for achieving a certain strain amplitude, there exist two possible working temperature levels, each within one of the two temperature ranges $[T_0, M_f]$ and $[M_f, M_s]$, which can be approximately described by the following two equations:

$$\Delta\varepsilon = -0.01\,T^2 + 0.89\,T - 12.91 \qquad \text{where } T_0 < T < M_f \tag{7a}$$

$$\frac{(M_s - T)}{0\% - \Delta\varepsilon} = \frac{(M_s - M_f)}{0\% - 6\%} \;\rightarrow\; \Delta\varepsilon = 6\% \cdot \frac{(M_s - T)}{(M_s - M_f)} \qquad \text{where } M_s > T > M_f \tag{7b}$$

where Eq. (7a) is determined by data fitting (to a quadratic equation) and Eq. (7b) is a linear dependence of the strain amplitude on the temperature between M_s and M_f. So, combining the above two equations (Eqs. (7a) and (7b)) and the heat balance equation Eq. (2), we can design a working state (i.e., choosing a combination of T and $\Delta\varepsilon$) and determine the setting of a proper heat transfer condition (the level of t_h) to achieve the designed working state. The tests in Figure 3.1 have already demonstrated the successful strain amplitude modulation with gradually tuning t_h (see the data of blue solid circles in Figure 3.4). But, in most advanced engineering applications, it might be demanded to change from one working state to another rapidly and reliably. To verify the robustness of the amplitude modulation of the system, another new tests are performed by changing t_h suddenly (i.e. changing the airflow velocity rapidly, with the operation time less than 2 seconds) as shown in Figure 3.5 where three typical tests demonstrate the system switch between two working states by cyclically controlling the level of t_h.

As discussed in Eq. (7a) and (7b), there are two temperature ranges (two relations between the strain amplitude $\Delta\varepsilon$ and temperature T) which are governed by two different physical mechanisms (temperature-dependent dissipative twinning stress and the phase-fraction adjustment). So, basically we have three different schemes for a given amplitude modulation (for example, switching between output strain amplitudes $\Delta\varepsilon_1$ and $\Delta\varepsilon_2$); in other words, we can choose different working temperatures for the transition between two stable working states S_1 (T_1 and $\Delta\varepsilon_1$) and S_2 (T_2 and $\Delta\varepsilon_2$). As indicated by three solid arrowed curves in Figure 3.4, we have three qualitatively different settings: (I) let both T_1 and T_2 be less than M_f, setting both T_1 and T_2 according to Eq. (7a), i.e., with two different levels of strong airflow (short t_h) for the two working states; (II) let both T_1 and T_2 be higher than M_f, setting both T_1 and T_2 according to Eq. (7b), i.e., with two different levels of weak airflow (large t_h) for the two working states; (III) let T_1 and T_2 be in different temperature ranges (e.g., $T_1 < M_f$ and $T_2 > M_f$). The three schemes have different dynamic transition features as shown in Figure 3.5(a), (b) and (c), respectively.

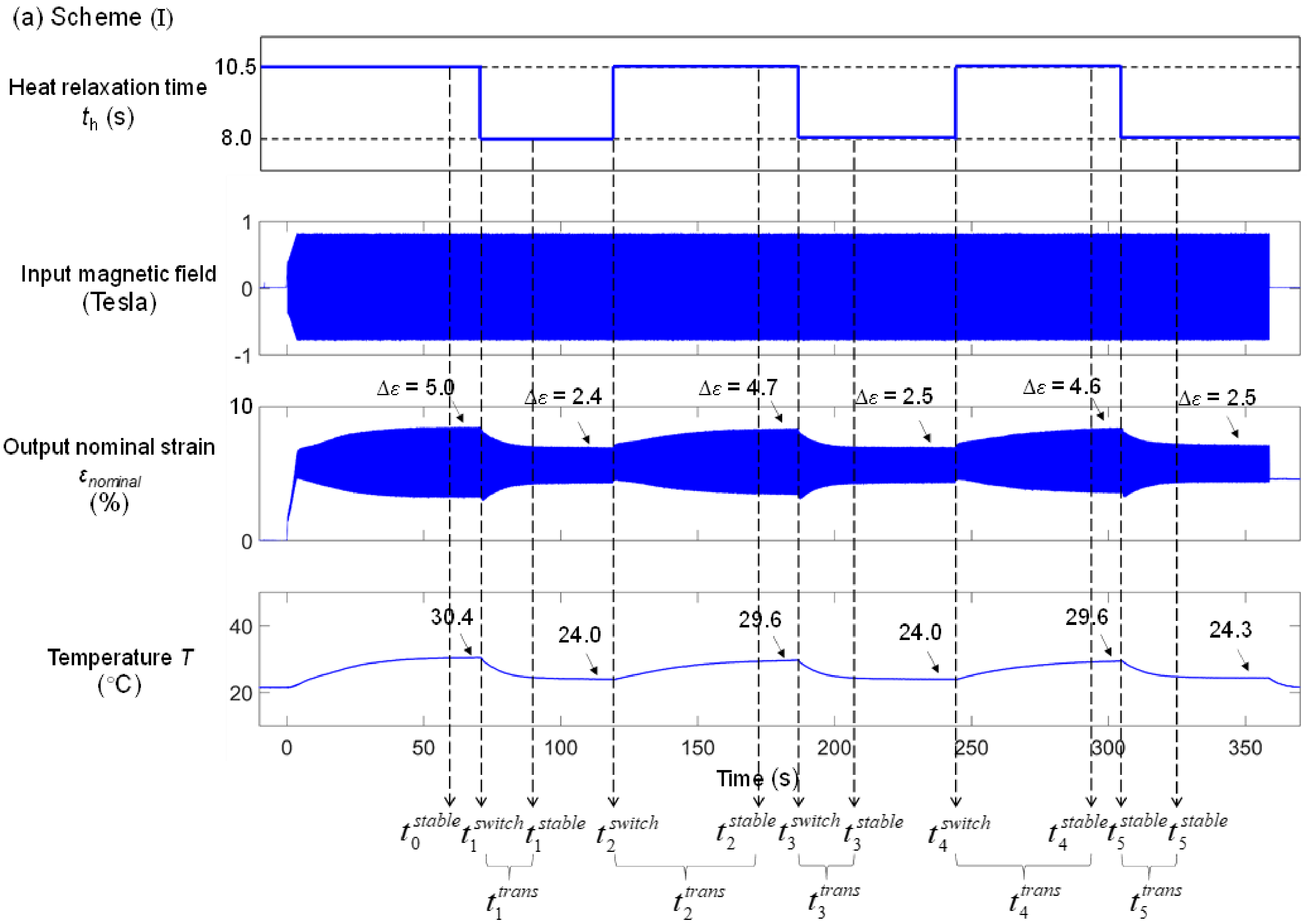
(a) Scheme (I)
Heat relaxation time
t_h (s)
10.5
8.0
Input magnetic field
(Tesla)
1
0
-1
Output nominal strain
$\varepsilon_{nominal}$
(%)
10
0
$\Delta\varepsilon$ = 5.0
$\Delta\varepsilon$ = 2.4
$\Delta\varepsilon$ = 4.7
$\Delta\varepsilon$ = 2.5
$\Delta\varepsilon$ = 4.6
$\Delta\varepsilon$ = 2.5
Temperature T
(°C)
40
20
30.4
24.0
29.6
24.0
29.6
24.3
0
50
100
150
200
250
300
350
Time (s)
t_0^{stable}
t_1^{switch}
t_1^{stable}
t_2^{switch}
t_2^{stable}
t_3^{switch}
t_3^{stable}
t_4^{switch}
t_4^{stable}
t_5^{stable}
t_5^{stable}
t_1^{trans}
t_2^{trans}
t_3^{trans}
t_4^{trans}
t_5^{trans}

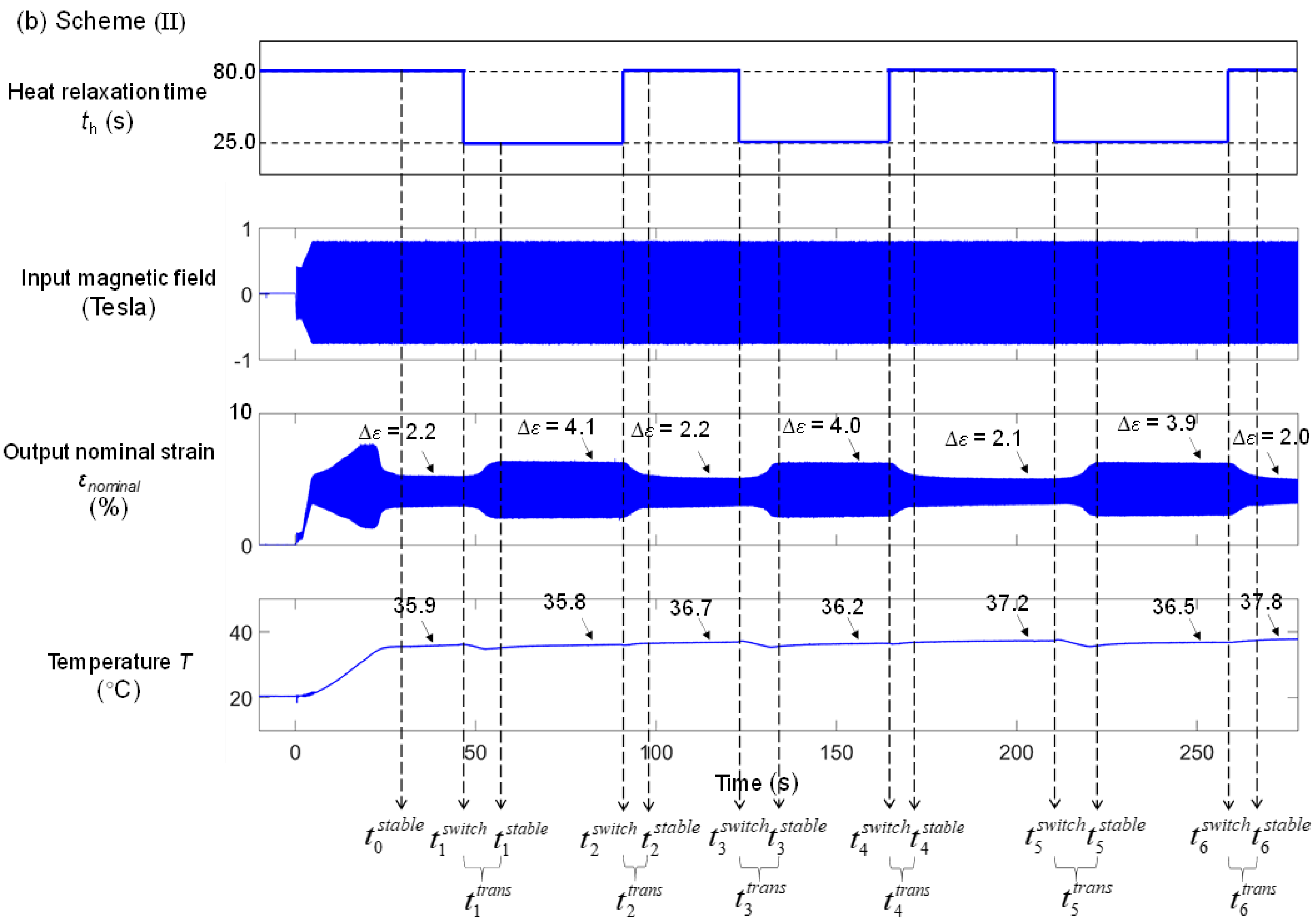

(b) Scheme (II)

Heat relaxation time
t_h (s)
80.0
25.0
Input magnetic field
(Tesla)
1
0
-1
Output nominal strain
$\varepsilon_{nominal}$
(%)
10
0
$\Delta\varepsilon = 2.2$
$\Delta\varepsilon = 4.1$
$\Delta\varepsilon = 2.2$
$\Delta\varepsilon = 4.0$
$\Delta\varepsilon = 2.1$
$\Delta\varepsilon = 3.9$
$\Delta\varepsilon = 2.0$
Temperature T
(°C)
40
20
35.9
35.8
36.7
36.2
37.2
36.5
37.8
0
50
100
150
200
250
Time (s)
t_0^{stable}
t_1^{switch}
t_1^{stable}
t_2^{switch}
t_2^{stable}
t_3^{switch}
t_3^{stable}
t_4^{switch}
t_4^{stable}
t_5^{switch}
t_5^{stable}
t_6^{switch}
t_6^{stable}
t_1^{trans}
t_2^{trans}
t_3^{trans}
t_4^{trans}
t_5^{trans}
t_6^{trans}

(c) Scheme (III)

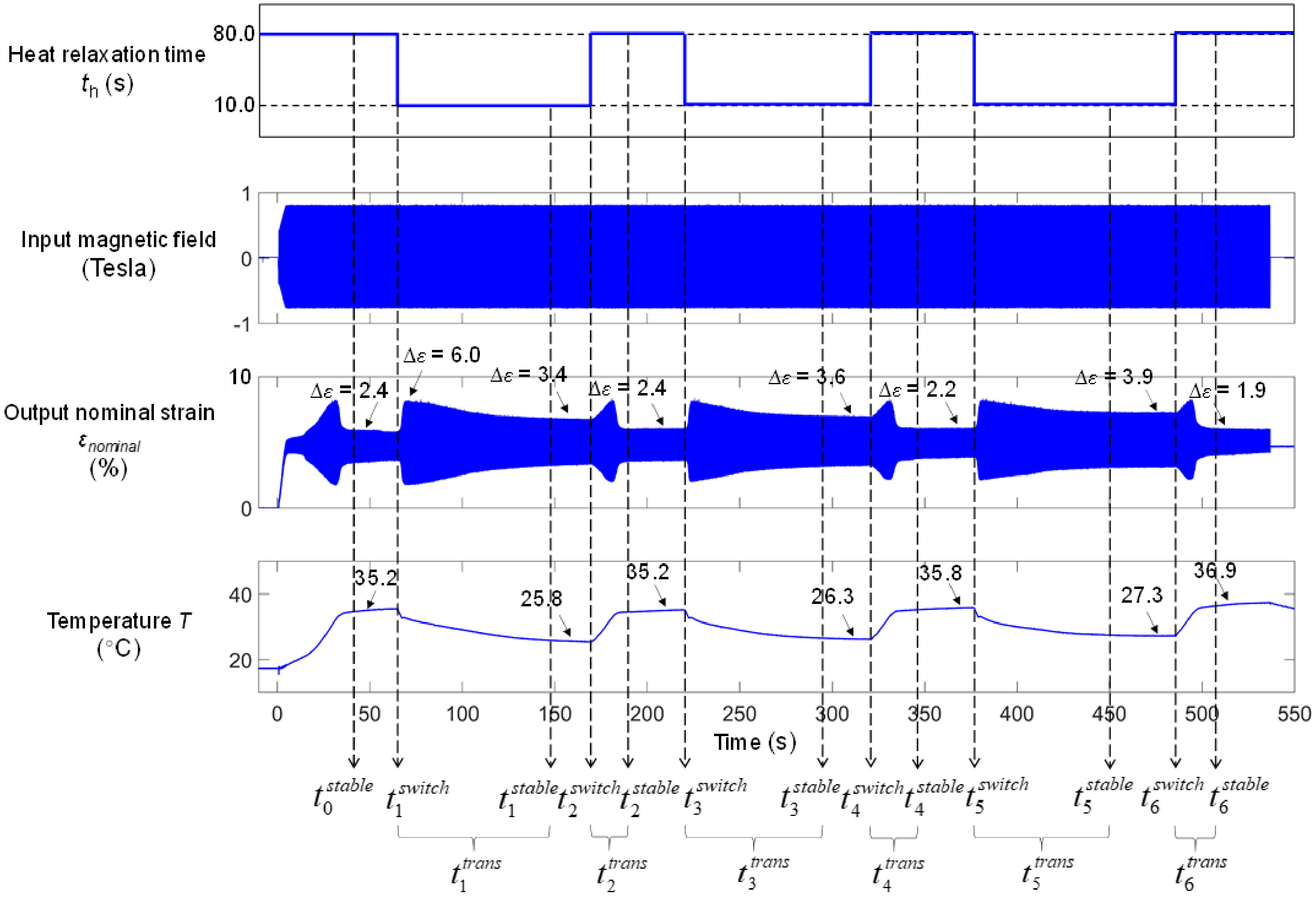
Heat relaxation time
t_h (s)
80.0
10.0
Input magnetic field
(Tesla)
1
0
-1
Output nominal strain
$\varepsilon_{nominal}$
(%)
10
0
$\Delta\varepsilon$ = 2.4
$\Delta\varepsilon$ = 6.0
$\Delta\varepsilon$ = 3.4
$\Delta\varepsilon$ = 2.4
$\Delta\varepsilon$ = 3.6
$\Delta\varepsilon$ = 2.2
$\Delta\varepsilon$ = 3.9
$\Delta\varepsilon$ = 1.9
Temperature T
(°C)
40
20
35.2
25.8
35.2
26.3
35.8
27.3
36.9
0
50
100
150
200
250
300
350
400
450
500
550
Time (s)
t_0^{stable}
t_1^{switch}
t_1^{stable}
t_2^{switch}
t_2^{stable}
t_3^{switch}
t_3^{stable}
t_4^{switch}
t_4^{stable}
t_5^{switch}
t_5^{stable}
t_6^{switch}
t_6^{stable}
t_1^{trans}
t_2^{trans}
t_3^{trans}
t_4^{trans}
t_5^{trans}
t_6^{trans}

Figure 3.5 Cyclic transitions of different stable states driven by switching the ambient heat transfer efficiency (a) Scheme (I) with cyclic switching t_h between 10.5 s and 8.0 s, (b) Scheme (II) with cyclic switching t_h between 80.0 s and 25.0 s, and (c) Scheme (III) with cyclic switching t_h between 80.0 s and 10.0 s.

In Figure 3.5(a) of the scheme (I) with cyclic changing t_h between 10.5 s and 8.0 s, the stable strain amplitude switches between around 4.7% and around 2.4% while the two stable working temperatures are around 30 °C and 24 °C which are significantly less than M_f to avoid the participation of Austenite. The two stable working states, S_1 = (~4.7%, ~30 °C) and S_2 = (~2.4%, ~24 °C) satisfy the relation of Eq. 7(a) as shown in Figure 3.4 (see the data of green squares). As the temperature dependence of the resistant twinning stress governs this strain amplitude modulation, the working-state dynamic transition mainly depends on the temperature difference between T_1 and T_2 (here $\Delta T \approx 6$ °C) during the controlled heat transfer (particularly controlled by t_h). It is seen in Figure 3.5(a) and Table 1 that the time of the transition from S_1 to S_2 is around 20 s (e.g., $t_1^{trans} = t_1^{stable} - t_1^{switch} \approx 19$ s for the transition during the ambient heat transfer of t_h = 8.0 s), while the time of the reverse transition from S_2 to S_1 is around 50 s (e.g., $t_2^{trans} = t_2^{stable} - t_2^{switch} \approx 53$ s for the transition during t_h = 10.5 s); in other words, the longer the t_h of the ambient heat transfer, the longer the state transition time. And the transition time is larger than its corresponding t_h in current test.

In Figure 3.5(b) of the scheme (II) with cyclic changing t_h between 80.0 s and 25.0 s, the system switches between the two states: S_1 = (~2.2%, $T_1 \approx M_f$) and S_2 = (~4.1%, $T_2 \approx M_f$) as summarized in Figure 3.4 (see the data of black triangles)—there are scattering/errors in the temperature measurements on T_1 and T_2, whose reason might be that the dynamic-changing active zones at the specimen's gauge section are not directly measured/contacted by the sensor/thermocouple which is attached at the end of the specimen. As the temperature change (the difference between T_1 and T_2) is not large, both the forward (S_1 to S_2) and the reverse (S_2 to S_1) transition times are small (around 12 s and 9 s respectively) and much less than the corresponding t_h.

In Figure 3.5(c) of the scheme (III) with cyclic changing t_h between 80.0 s and 10.0 s, the system switches between the two states: S_1 = (~2.4%, $T_1 \approx M_f$) and S_2 = (~3.4%, $T_2 \approx 25.8$ ^{o}C < M_f). Different from the schemes (I) and (II) whose transition between two stable strain amplitudes is smooth (monotonic), the scheme (III) has non-monotonical change in the strain amplitude during the transition—the strain amplitude passes the maximum martensite-reorientation value (6%) during the switch between S_1 and S_2. More interestingly, the forward transition time from S_1 to S_2 is much longer than that of the reverse transition from S_2 to S_1, e.g., $t_1^{trans} \approx$ 82s significantly larger than $t_2^{trans} \approx$ 20s. Such complicated dynamic transition features are attributed to the coupling of the two mechanisms (the temperature-dependence of the twinning stress and the phase-fraction adjustment). Full understanding and quantitative prediction on such transition phenomena demand advanced dynamic models for the thermo-magneto-mechanical coupling behaviours.

Comparing the performances of these three schemes in Table 3.1 about the transition times and in Figure 3.6 about the data scattering of the modulated strain amplitudes, we can see that Scheme (II) has the fastest response/transition and small scattering in the strain amplitudes, but it has a limited range of the working temperature related to the material's characteristic phase transformation temperature (M_f and M_s). By contrast, Scheme (I) has a wider working temperature range (from T_0 to M_f) while its scattering in strain amplitude is small; moreover, there is no austenite participation in Scheme (I) making the microstructure avoid the complex A-M interface and the compatibility problem, which might influence the material's fatigue behaviour. Normally, Scheme (III) would not be suggested for engineering applications because it has non-smooth strain amplitude change (always passing a peak strain amplitude 6% during the transition) and the transition time is the longest among the three schemes.

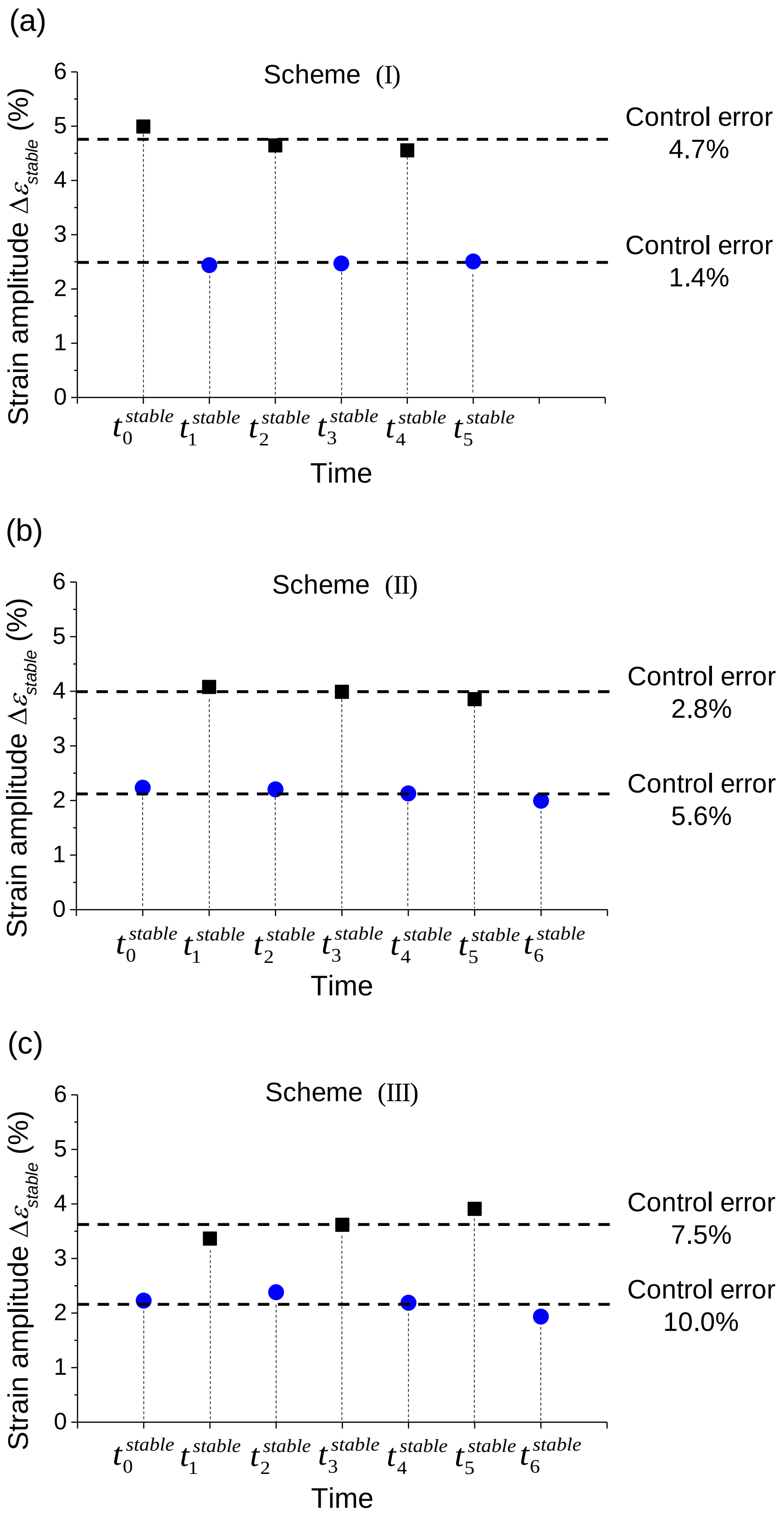

Figure 3.6 The strain amplitude scattering in Schemes I, II and III. The control error is defined as $\frac{\Delta\varepsilon^{\max} - \Delta\varepsilon^{\min}}{2\Delta\varepsilon^{mean}}$.

Table 3.1 The typical dynamic transition times in Schemes (I), (II) and (III).

	Transition time (s)					
Scheme	t_1^{trans}	t_2^{trans}	t_3^{trans}	t_4^{trans}	t_5^{trans}	t_6^{trans}
I	19	53	21	49	20	\
II	12	9	12	9	13	10
III	82	20	74	18	73	19

3.4 Summary

In this chapter, the thermal effect on the magnetic-field-induced strain oscillation of magnetic shape memory alloy is investigated by the systematic experiments with stepwise gradually changing thermal boundary condition (from still ambient air to strong airflow) and the dynamic experiments of cyclic rapid switching between different levels of the ambient heat transfer efficiency (characterized the heat relaxation time t_h). There are abundant interesting phenomena, such as the *non-monotonic* t_h-dependence of the strain oscillation amplitude (Figure 3.2), the *inverse proportional* relation between the strain amplitude and t_h in the region of weak heat transfer (Figure 3.3(b)), and the necessary passage through the maximum strain amplitude (6%) during the state transition crossing the critical temperature M_f (see Scheme (III) in Figure 3.4 and Figure 3.5(c)). All these phenomena can be basically understood with the two physical mechanisms: the temperature dependence of the martensite-reorientation resistant force (twinning stress) and the phase-fraction adjustment of the martensitic phase transformation. As the two mechanisms involve non-smooth processes of multi-physics coupling, advanced models (with quantitative prediction and/or detailed simulation) are demanded for both fundamental understanding and engineering designs.

This work is focused on the thermal method to modulate the strain oscillation amplitude, studying the system performance under a given magneto-mechanical loading. It is expected that different magneto-mechanical loadings (e.g., changing the frequency) would change the strain amplitude. But the qualitative features of the thermal methods (e.g., the dynamic transition features of Schemes I, II and III in Figures 3.4 and 3.5) would be the same, while quantitative changes are anticipated, e.g., the maximum strain amplitude of the necessary passage of Scheme III might be less than 6% if the magneto-mechanical forces do not allow full martensite reorientation. To provide a full picture of the system performance under various Thermo-Magneto-Mechanical loadings, more careful experiments are needed in the future.

Chapter 4

Self-accommodation versus Two-way memory in Ni-Mn-Ga single crystal

Self-accommodation is an important concept in the one-way shape memory behaviour of Shape Memory Alloys (SMA) whose global shape keeps unchanged during the cooling-induced transformation from the high-symmetry austenite phase to the low-symmetry martensite phase (consisting of different martensite variants/twins). While the self-accommodation martensite structures have been observed in various SMA polycrystals, there is no experiment to verify it in any SMA single crystal. In this chapter, systematic experiments are performed to measure the global shape change of different specimens (bars) of Ni-Mn-Ga SMA single crystal under different heating-cooling cycles. In addition to the global shape change, the local strain distributions in the specimen are measured with DIC technique (Digital Image Correlation) so that the detailed evolution of the martensite twins can be characterized and combined with simple theoretical compatibility analysis. To keep stress-free, the specimen is free standing by clamping only one end. At the clamping end, we can also put a low-temperature ice to quickly cool down the specimen, so-called local cooling or inhomogeneous cooling with strong thermal gradient along the specimen's length direction, compared to the natural cooling (approximately homogenous cooling mainly via the heat convection between the specimen's surfaces and the ambient). It is found that non-self-accommodation configuration (a martensite twin or a single martensite variant) with a significant global shape change dominates in the naturally cooling-induced martensite formation in the thin specimen; by contrast, the thick specimen has more space to allow the simultaneous formation of multiple twins, leading to only a small global shape change like self-accommodation. More interesting is that the local cooling with a strong thermal gradient can guarantee only one Austenite-Martensite interface propagating through the specimen so that non-self-accommodation configuration (a martensite twin or a single martensite variant) dominates again. That means, a stress-free two-way memory of the SMA single crystal can be achieved by proper selection of the specimen geometry and the cooling scheme.

4.1 Introduction

Ni-Mn-Ga magnetic Shape Memory Alloy (SMA) is well known for its magnetic-field-induced large deformation which has been intensively studied by researchers (Bruno et al., 2017; Chen et al., 2013; Chen et al., 2014; Chmielus et al., 2008; Faran and Shilo, 2016; He et al., 2011, 2012; Heczko O. et al., 2000; Kiefer and Lagoudas, 2008; Murray et al., 2000; R.D. James et al., 1995; Seiner et al., 2011; Straka et al., 2008; Ullakko et al., 1996; Yu et al., 2020; Zhang et al., 2018a, b). Recently, my research group studied the interaction between the magnetic-field induced martensite reorientation and the associated self-dissipation-heating-induced phase transformation to design special actuators working in different temperature ranges (Chen and He, 2020; Zhang et al., 2020), which implies non-trivial formation of martensite twin structures during the temperature-induced phase transformation in the Ni-Mn-Ga SMA single crystal that deserves further exploration.

Ni-Mn-Ga SMA single crystal is able to take the phase transformation between a high-symmetry phase (cubic austenite phase (A-phase)) and a low-symmetry phase — martensite phase (M-phase) that is approximately “tetragonal” (Arndt et al., 2006; Haldar et al., 2014; Karaca et al., 2012; Karaca et al., 2007; Pinneker et al., 2014; Pinneker et al., 2013). Because the martensite phase has several variants (here there are 3 different tetragonal martensite variants with the different orientations of the characteristic atomic lattice/unit-cell as shown in Figure 1.1), the material’s states at low temperatures (lower than the material characteristic phase transformation M_f) can be a single martensite variant, a martensite twin (consisting of two martensite variants) or a mixture of multiple twins, among which some special combinations of different twins/variants are called self-accommodation configurations whose overall macroscopic shape is approximately the same as that of the high-temperature state — austenite phase. That means, the cooling-induced martensitic phase transformation with the self-accommodation configuration would not lead to any global deformation. Because the self-accommodation mechanism is important in understanding the Shape Memory Effect — so-called "one-way memory" (Bhattacharya, 1992; Bhattacharya, 2003; Cisse et al., 2016; Sehitoglu et al., 2012), many observations and discussions on the self-accommodation in different SMA polycrystals were reported, such as CuAlNi polycrystal SMA (Aydogdu et al., 2002), Ti-Nb polycrystal (Chai et al., 2009), NiTi polycrystal (Miyazaki S. et al., 1989; Waitz, 2005; Waitz et al., 2008), and the associated theoretical explanations and modelling in (Chemisky et al., 2011; Hirth and Pond, 2011; Madangopal, 1997; Madangopal et al., 1991; Madangopal et al., 1993a; Madangopal et al., 1993b; Teramoto et al., 2020). However, in literature, there is no systematic experiment to verify whether self-accommodation can occur in SMA **single crystals**.

For the verification in this chapter, systematic experiments are performed to measure the global shape change of different specimens (bars) of Ni-Mn-Ga SMA single crystal under different heating-cooling cycles. In addition to the global shape change, the local strain distributions in the specimen are measured by the DIC technique (Digital Image Correlation) combined with the in-situ observation on specimen's surfaces by two optical cameras. Based on the local strain measurements and the theoretical compatibility analysis, the detailed evolution of the martensite twins can be characterized. To realize the pure thermally driving phase transformation without mechanical stress, the specimen was clamped at only one end and the other end is free to elongate/contract as shown in Figure 2.3. Firstly, the specimen's temperature was increased to trigger the martensite → austenite (M → A) phase transformation; then it was cooled to transform back to martensite phase where the specimen's overall elongation and the associated martensite structure — self-accommodation without global shape change or non-self-accommodation with significant shape change — can be characterized. The experiment was performed on two different specimens (thin and thick plates) by two different cooling schemes: (1) Natural cooling (just stop heating to let the specimen cool down) that is approximately homogenous cooling mainly via the heat convection between the specimen's surfaces and the ambient. (2) Ice local cooling (put a piece of low-temperature ice at the clamping end to cool down the specimen quickly), which is inhomogeneous cooling with strong thermal gradient along the specimen's length direction. It is found that the cooling-induced martensite structure can be a single variant, a twin or multiple twins (approximately the self-accommodation configuration) depending on the specimen's geometry and the cooling mode. That means, a stress-free two-way memory can be achieved by proper selection of the specimen and the heating-cooling scheme.

The remaining parts of this chapter include the following sections: the experimental procedure and the experimental result are reported respectively in Sections 4.2 and 4.3. Then the conditions for the two-way memory versus the one-way memory (self-accommodation) are discussed in Section 4.4. Finally, the summary and conclusions are given in Section 4.5.

4.2 Material properties and experimental procedure

The tested specimens of $Ni_{50}Mn_{28}Ga_{22}$ (at. %) single variant (from ETO Magnetic GmbH) are rectangular bars with all faces approximately along the {100} planes of the parent cubic austenite. Two different types of specimens are tested, whose cross-sections are 2.5mm × 1mm (thin specimen) and 3mm × 2mm (thick specimen); the gauge length after clamping for both specimen types is around 10mm as shown in Figure 2.6. The two types of specimens have different characteristic phase transformation temperatures: M_f = 45 ^{o}C, M_s =48 ^{o}C, A_s = 52 ^{o}C, A_f = 55 ^{o}C for the thin specimen; M_f = 30 ^{o}C, M_s = 33.5 ^{o}C, A_s = 41 ^{o}C, A_f = 46 ^{o}C for the thick specimen. But both are in the state of martensite phase at room temperature (around 20 ^{o}C < M_f).

The setup of the experiment is shown in Figure 2.3 where a specimen is clamped at one end while the other end is free to deform. To monitor the deformation of the specimen, two optical cameras (CMOS: acA2000-340km, Basler, Germany) equipped with a Nikkor lens are used to observe the specimen's top surface (Camera 1) and one of the side surfaces (Camera 2). To observe the detailed deformation features of the Austenite-Martensite (A-M interfaces), a microscope (AX70, Olympus, Japan) is used as in Figure 2.5. Based on these optical observations and the technique of Digital Image Correlation (DIC of the software VIC-2D), the local strain distributions (and in turn the distributions of the martensite variants) can be determined.

At the beginning of the experiment, the specimen is martensite phase at room temperature (20 ^{o}C < M_f). For a clear demonstration, the initial state of the specimen can be set to be a single martensite variant (for example, M_1 single variant, which can be achieved by a compression along the specimen's length direction, i.e., *x*-direction). No matter which single variant is set at the initial state, the heating by the heater at the specimen's clamping end triggers the M → A transformation with an A-M interface nucleated at the clamping end, which propagates towards the specimen's free end. A thermocouple (K-Type of sheath diameter of 0.5 mm) is put at the clamping end to monitor the local temperature evolution. When the heater turns off, the measured temperature at the clamping end decreases from the maximum level (T_{max}) as shown in the 1st cooling mode (natural cooling) in Figure 2.4(a); the process of the natural cooling to room temperature usually takes several minutes. To speed up the cooling process, we can put a piece of low-temperature ice at the clamping end, and the measured temperature drops quickly as shown in the 2nd cooling mode (ice local cooling) in Figure 2.4(b). Depending on the maximum heating temperature T_{max} and the cooling mode, the martensite formation in the specimen demonstrates various patterns as shown in the following section.

4.3 Experimental Results

The observations on the thin and the thick specimens are reported in the following Sections 4.3.1 and 4.3.2, respectively. In each of these two sections, the two cooling modes ("natural cooling" and "ice local cooling") are studied.

4.3.1 Martensite formation in thin specimen

The different martensite formations in the thin specimen by the two cooling modes are described in the following two subsections 4.3.1.1 and 4.3.1.2, respectively. Particularly in Section 4.3.1.1 for the "natural cooling", the effect of the maximum heating temperature $T_{\max}$ is demonstrated.

4.3.1.1 Martensite formation in thin specimen by **“natural cooling”**

When the maximum heating temperature at the specimen’s clamping end ($T_{\max}$) is not high (around 56 ^{o}C, just a little higher than the material characteristic phase transformation temperature A_f), the propagating A-M interface (the phase transformation front) cannot reach the specimen’s free end whose temperature is not high enough to start the M → A transformation as shown in Figure 4.1, 4.5 and 4.7, so-called Case (I) — “Partial specimen under transformation”. By contrast, when $T_{\max}$ is high enough (around 100 ^{o}C, much higher than A_f), the whole specimen is transformed into austenite phase as shown in Figure 4.8, Case (II) — “Whole specimen under transformation”. The cooling-induced martensite formations in these two cases are significantly different and reported in the following Sections 4.3.1.1.1 and 4.3.1.1.2, respectively.

4.3.1.1.1 Case (I) — “Partial specimen under transformation”

For a clear demonstration, the initial martensite state of the specimen was set to be the single variant M_1, M_2, and M_3 as shown in the following Sections (A), (B), and (C) respectively. In current case — “Partial specimen under transformation”, only part of the specimen near the clamping end takes the M → A phase transformation; so, the part near the free end of the specimen always remains at the initial state (the single martensite variant) which has significant influence on the cooling-induced martensite formation in the transforming part near the clamping end as shown in the following detailed observations.

Section (A): Initial state M_1

As shown in Figure 4.1, at the beginning of the heating-cooling cycle, the specimen was occupied by M_1 whose strain components $\varepsilon_{xx} \approx -4\%$, $\varepsilon_{yy} \approx 2\%$, and $\varepsilon_{zz} \approx 2\%$ (taking A-phase as the reference) as shown in the DIC strain maps from the two cameras at the states t_1 and t_2; these values agree with the theoretically calculated strain magnitudes with the characteristic lengths of the A-phase and Martensite variants (the variant’s short axis $c \approx 0.561$ nm, long axis $a \approx 0.595$ nm and the austenite characteristic length $a_0 \approx 0.584$ nm as shown in Figure 1.1) (Heczko et al., 2002; Straka et al., 2008). The heating triggered the nucleation and growth of the A-phase via a propagating A-M interface as shown in the strain maps (t_3) and (t_4), where A-phase occupied around a half of the specimen while the single martensite variant M_1 (the initial state) still occupied the other half near the specimen's free end. When the heating was stopped and the specimen cooled down naturally to make A-phase shrink back and disappear at the clamping end as shown by the strain maps at t_5 ~ t_8, during which the half of the specimen near the clamping end changed to a martensite twin M_1:M_2 with the volume ratio 2:1 whose strain components are $\varepsilon_{xx} \approx -2\%$, $\varepsilon_{yy} \approx 0\%$ and $\varepsilon_{zz} \approx 2\%$ (see the measurements of the local strain maps/profiles by the two cameras). The method to determine the twin's composition (M_1:M_2) with the strain maps can be found in Appendix B. More interesting is that the twin M_1:M_2 (2:1) was not stable, but evolved into the single variant M_1 identified by the measured local strain components $\varepsilon_{xx} \approx -4\%$, $\varepsilon_{yy} \approx 2\%$ and $\varepsilon_{zz} \approx 2\%$ (see strain maps/profiles near the clamping end at t_8 ~ t_{10}). This evolution can be seen as a detwinning process: the major variant of the twin (the variant with a larger volume fraction, here M_1) grew at the expense of the minor variant (M_2).

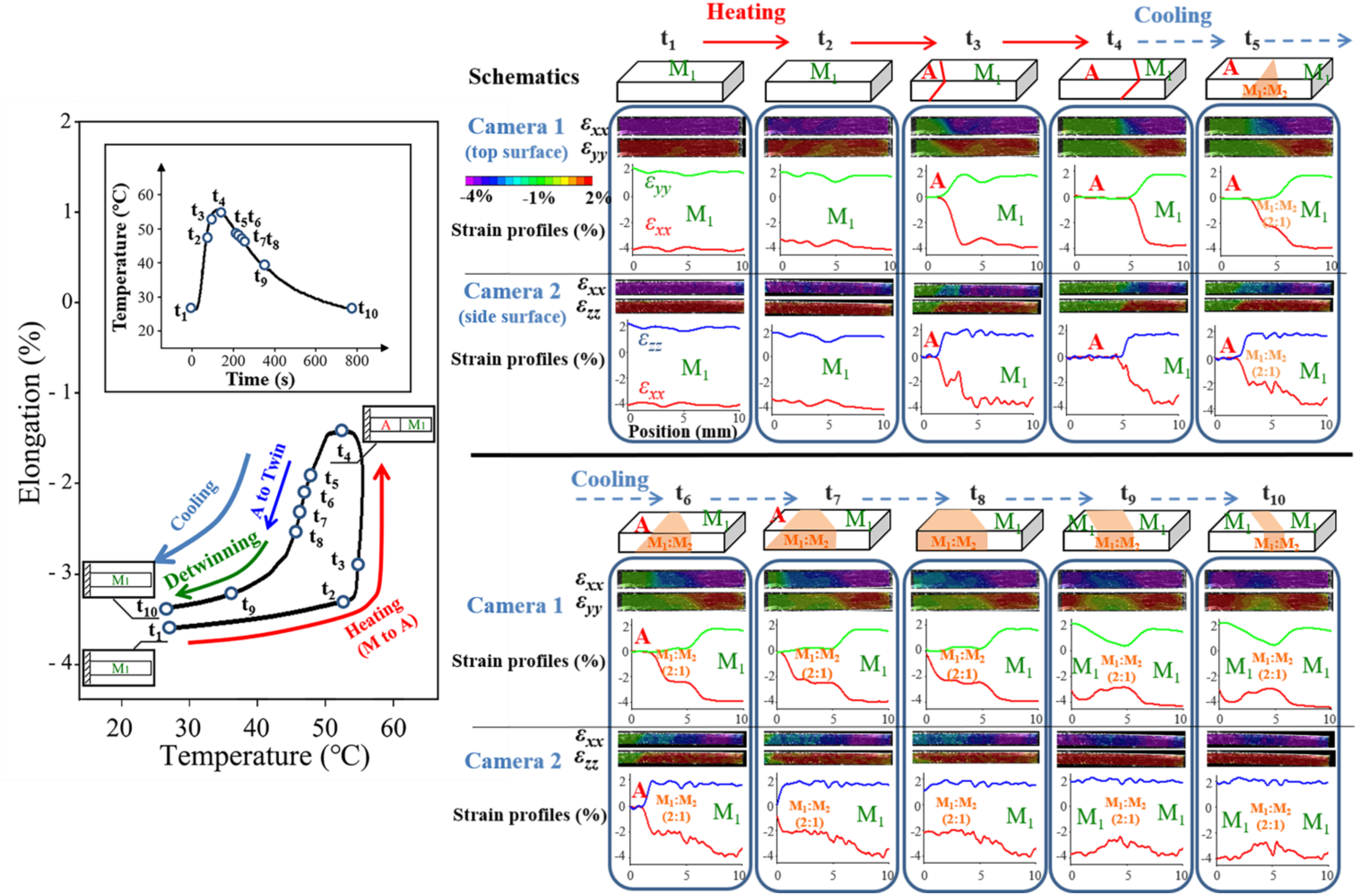

Figure 4.1 The specimen's global elongation and the associated local strain evolution observed by the two optical cameras (in terms of DIC strain maps and the typical strain profiles at the specimen's middle line along the length direction) during the heating-cooling cycle of Case (I) "Partial specimen under transformation" with the initial martensite state of the single variant M_1 in the thin specimen. The transition zone consisting of the twin M_1:M_2 (with the volume ratio 2:1) between A-phase and M_1 was clearly captured during the cooling process.

It is also seen in the strain map and the strain profile at t_{10} that a small region of the twin M_1:M_2 still remains at the final cooled martensite state, making the final state (t_{10}) have a small strain difference from the initial state (t_1) as shown in the specimen's elongation-temperature curve where $\varepsilon_{xx} \approx -3.6\%$ at t_1 while $\varepsilon_{xx} \approx -3.4\%$ at t_{10}. Nevertheless, as shown by the elongation-temperature curve, the heating-cooling cycle leads to the specimen's cyclic deformation between −3.4% and −1.4%, i.e., a cyclic strain magnitude around 2% (note: only around a half of the specimen participated in the thermally induced cyclic A ↔ M transformation in this case of "partial specimen under transformation").

In order to see more clearly the deformation feature at the A-M interface and the associated twin formation and detwinning, the above experiment is repeated by three continuous heating-cooling cycles shown in Figure 4.2, 4.3 and 4.4 respectively, where a microscope focused on a small region of the specimen's top surface demonstrated the different A-M interface structures in the heating and cooling processes. During the heating of the 1st cycle (Figure 4.2), a small "triangular" transition zone consisting of twin M_1:M_2 (volume ratio 2:1, whose average strains $\varepsilon_{xx} \approx -2\%$ and $\varepsilon_{yy} \approx 0\%$) was observed between the A-phase and the single variant M_1 (see the DIC strain maps (i) ~ (vi)); by contrast, during the cooling, the transition zone (twin M_1:M_2) grew up at the expense of A-phase (see (vii) ~ (xi)) which agreed with the full-field DIC strain maps of the whole specimen (states t_5 ~ t_8 in Figure 4.1 where the transition zone also grew up). Finally, the twin was detwinned into the single variant M_1 (see (xi) and (xii)).

However, the twin M_1:M_2 is not the unique possible composition of the transition zone for separating A phase from the single variant M_1; the heating process of the 2nd cycle shows another composition of the transition zone (see (i) ~ (v) in Figure 4.3: a small triangular transition zone consisting of twin M_1:M_3 (volume ratio 2:1, whose average strains $\varepsilon_{xx} \approx -2\%$ and $\varepsilon_{yy} \approx 2\%$).

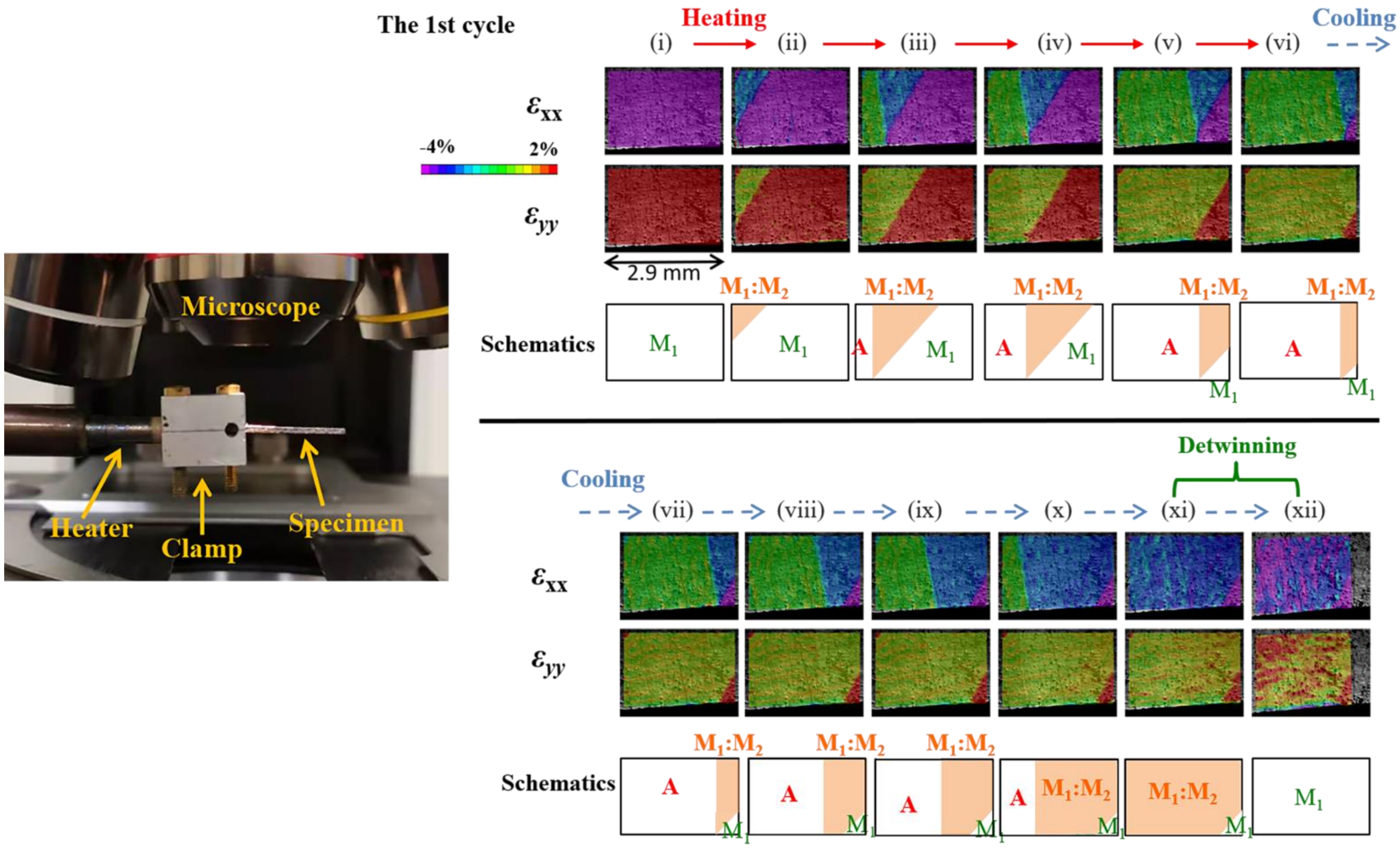

Figure 4.2 The observation by the microscope (in terms of DIC strain maps) on the local strain evolution during the 1st cycle of the three continuous heating-cooling cycles of Case (I) “Partial specimen under transformation” with the initial martensite state M_1 in the thin specimen. A small transition zone of the twin M_1:M_2 (volume ratio 2:1) separating A-phase from M_1 during the heating process; then the transition zone grew up and was detwinned into M_1 during the cooling process.

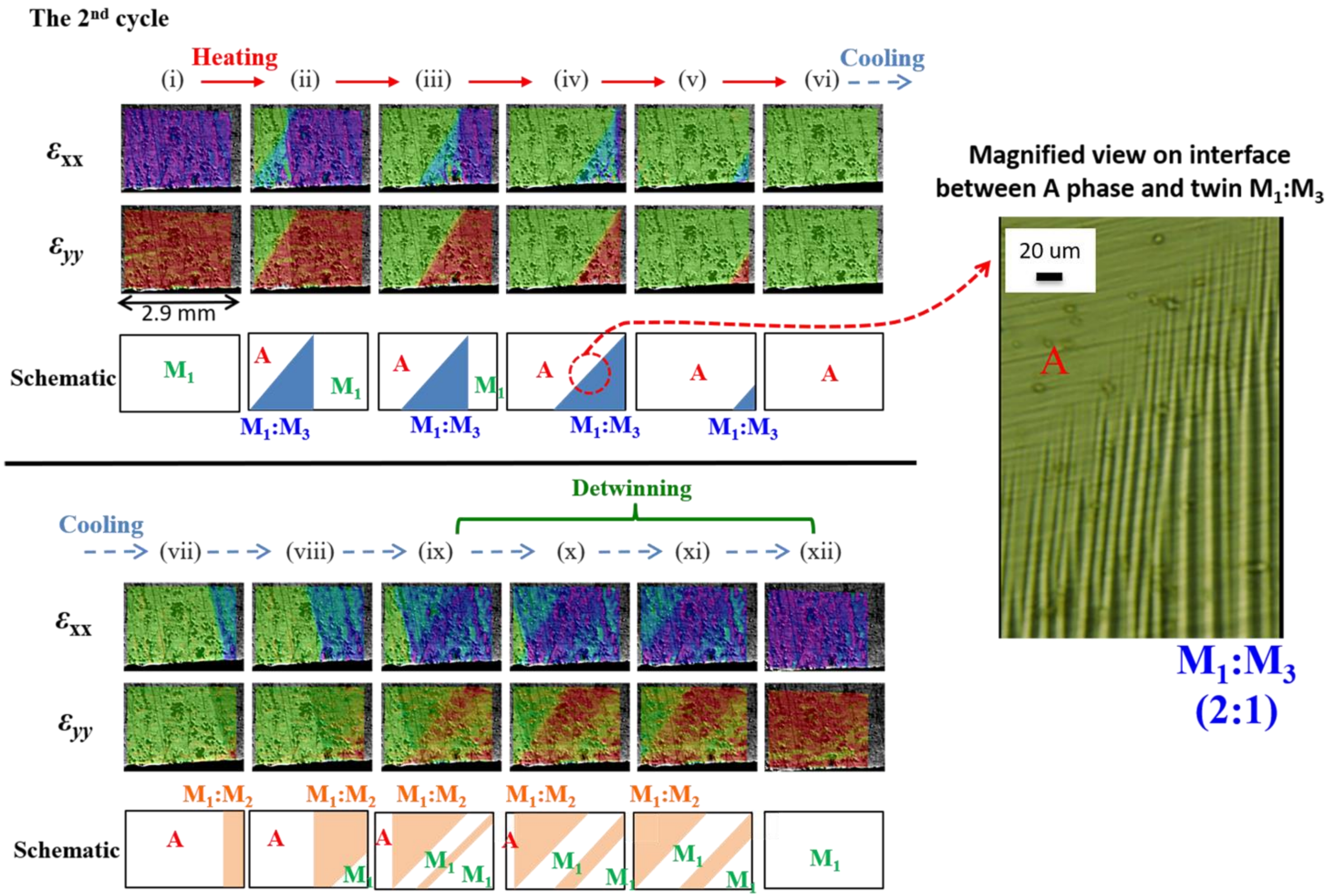

Figure 4.3 The observation by the microscope on the local strain evolution during the 2nd cycle of the three continuous heating-cooling cycles of Case (I) "Partial specimen under transformation" with the initial martensite state M_1 in the thin specimen. A small transition zone of twin M_1:M_3 (volume ratio 2:1) separated A-phase from M_1 during the heating process; the transition zone consisted of a laminate of the twin as shown by the magnified view. During the cooling process, a different twin was formed (M_1:M_2), grew up and was detwinned into M_1.

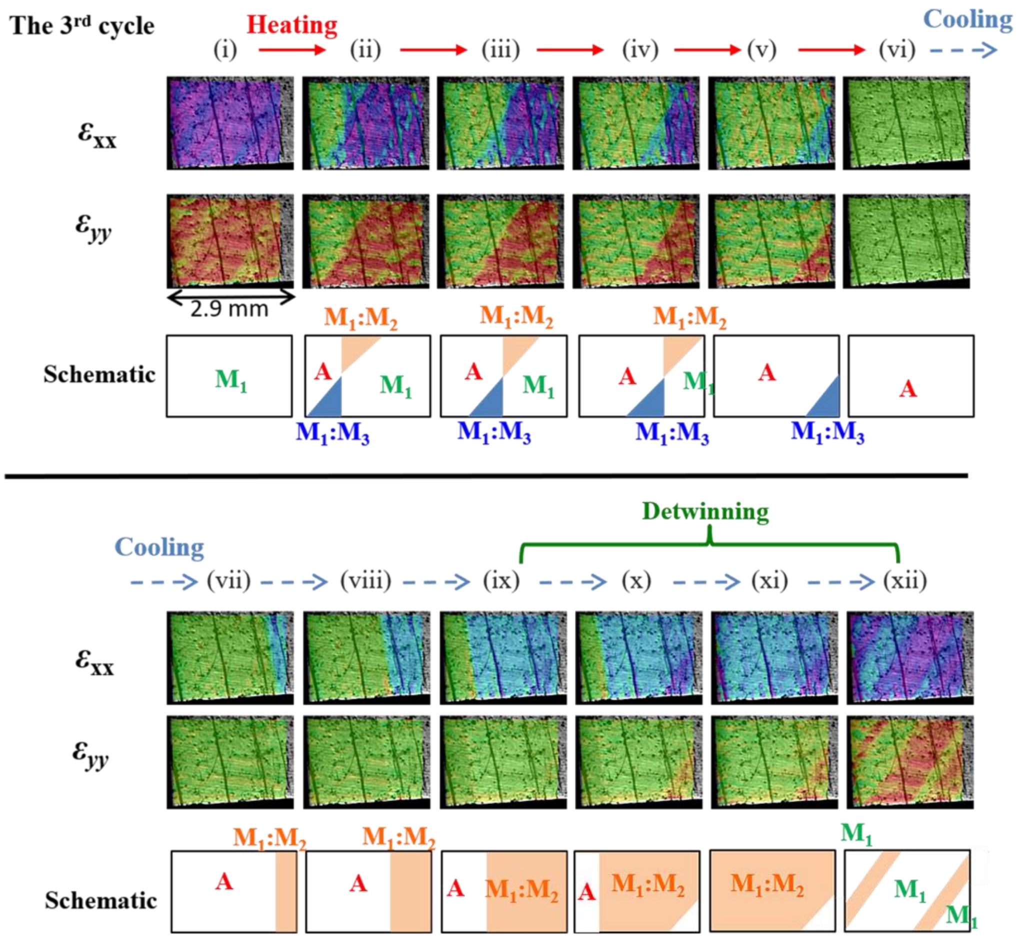

Figure 4.4 The observation by the microscope on the local strain evolution during the 3rd cycle of the three continuous heating-cooling cycles of Case (I) “Partial specimen under transformation” with the initial martensite state M_1 in the thin specimen. An “X” type A-M interface consisting of two different transition zones (twins M_1:M_2 and M_1:M_3) were formed during the heating process. During the cooling process, there was only one transition zone of the twin (M_1:M_2) that grew up and was detwinned into M_1.

With the magnified view in Figure 4.3, we can see that the transition zone is a laminate of the fine twins, which are numerous sharp “needles” penetrating into the region of A-phase. More interesting is that, during cooling-induced A → M transformation, the transition zone changes to the twin M_1:M_2 (2:1) as shown in (vii) ~ (xii) where the A-phase shrank while the transition zone M_1:M_2 grew up and was detwinned into M_1 simultaneously. It is easy to apply a compatibility analysis to verify that both the twin M_1:M_2 (2:1) and the twin M_1:M_3 (2:1) can be compatible with A-phase as shown in Appendix C where the theoretical predictions (d) and (b) of Figure C1 correspond respectively to the experimentally observed orientations of the interface between A-phase and the twin M_1:M_2 (2:1) in the pattern (iii) in Figure 4.2 and the interface between A-phase and the twin M_1:M_3 (2:1) in (iii) in Figure 4.3. In fact, these two twins can co-exist at the transition zone as shown in the heating process of the 3rd cycle (see (i) ~ (iv) in Figure 4.4) where an “X” type interface was observed (detailed theoretical analysis on the X-interface can be found in (Ruddock, 1994; Seiner et al., 2008). But, in the cooling process, only one twin appeared (M_1:M_2) which might help facilitate the detwinning into M_1 as shown in (vii) ~ (xii) in Figure 4.4.

Remark 1: The above results with the two optical cameras for the full-field observations on the whole specimen and the microscope for detailed observations on the austenite-martensite interface structures show the importance of compatibility: the transition zone between the A-phase and the single variant M_1 can have different compositions, but it must satisfy the compatibility requirements, i.e., only the compatible twins predicted in Figure C1 of Appendix C appeared in the experiments. In other word, the compatibility governs the phase transformation, particularly the martensite formation. As the transition zone has to be compatible also with the initial state (here M_1) of the untransformed region (the part near the free end of the specimen), the composition of the transition zone (i.e., the composition of the twin) was influenced by the initial martensite state as shown in Figure 4.1 ~ 4.4 where the initial state M_1 is the major component of the twin in the transition zone, i.e., M_1 has a larger volume fraction in the twins M_1:M_2 = 2:1 and M_1:M_3 = 2:1.

Section (B): Initial state M_2

To further verify the initial-state effect, the above heating-cooling cycle is repeated on the specimen with a different initial martensite state: the single martensite variant M_2 whose strain components $\varepsilon_{xx} \approx 2\%$, $\varepsilon_{yy} \approx -4\%$ and $\varepsilon_{zz} \approx 2\%$ (achieved by a compression along *y*-direction) as shown in Figure 4.5 where the specimen after the heating-cooling cycle returned to the same martensite variant as the initial state M_2 with a cyclic deformation (see the DIC strain maps $t_0 \sim t_{10}$ and the elongation-temperature curve). Different from the observed transition zone in Section (A), the current transition zone between A-phase and the single variant M_2 is a twin M_2:M_3 (with the volume ratio 2:1, whose average strain components $\varepsilon_{xx} \approx 2\%$, $\varepsilon_{yy} \approx -2\%$ and $\varepsilon_{zz} \approx 0\%$) as shown in the strain maps and the strain profiles at $t_6 \sim t_8$ in Figure 4.5.

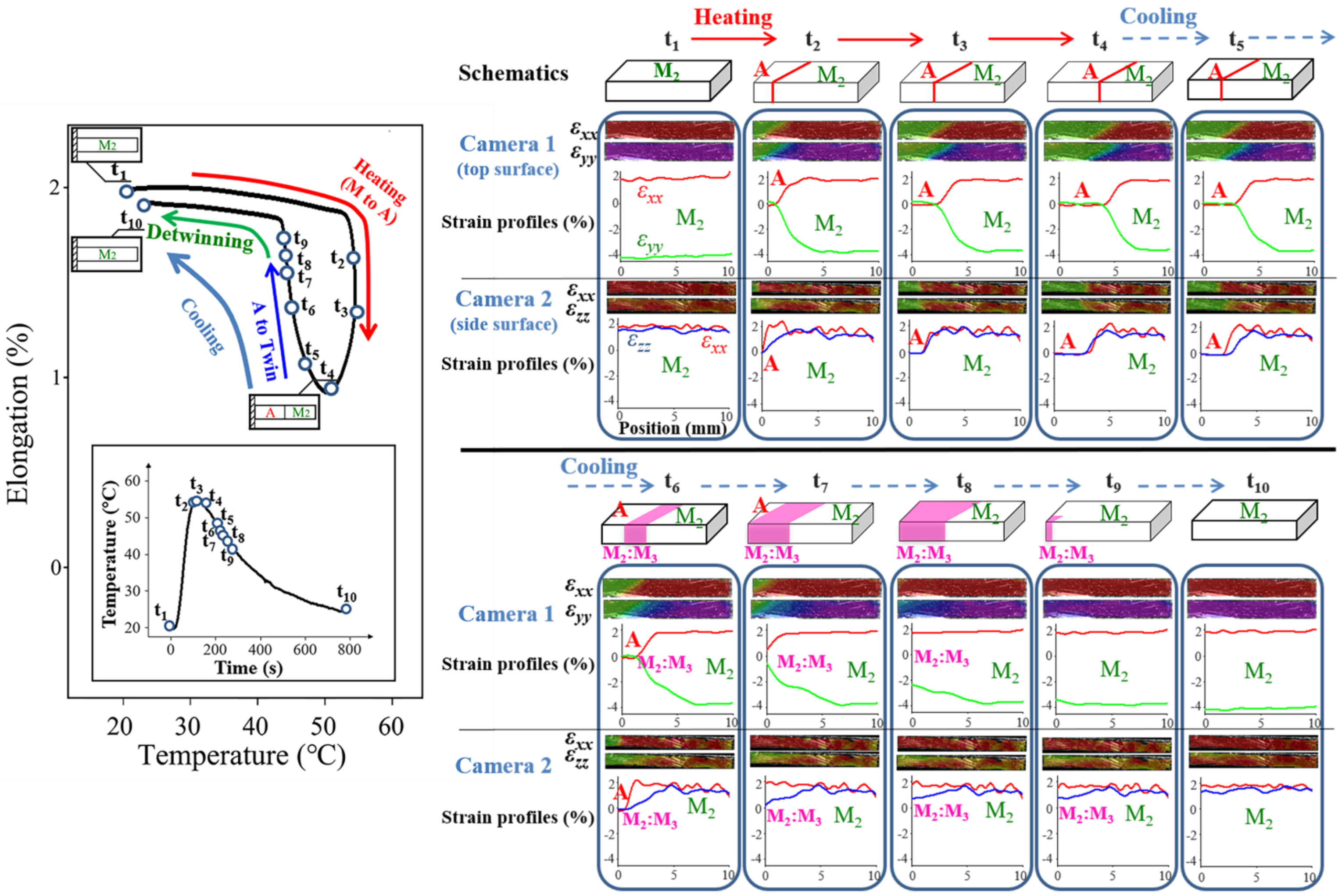

Figure 4.5 The specimen's global elongation and the local strain evolution during the heating-cooling cycle of Case (I) "Partial specimen under transformation" with the initial martensite state of M_2 in the thin specimen. The heating-cooling cycle led to the cyclic A-M phase transformation with a significant cyclic deformation and the single variant M_2 occupied the specimen at both the initial and final states of the cycle.

More clear pictures of the transition zone are shown in Figure 4.6 about the observation by the microscope. It is seen, in the strain maps (ii) ~ (iv) during the heating and (viii) ~ (x) during the cooling, that the transition zone has some coarse spikes (arrows) pointing to the region of the single variant M_2 while the boundary between A-phase and the transition zone is quite smooth, which in fact is a laminate of fine twins M_2:M_3 as shown by the magnified view in Figure 4.6. Such transition zone agrees with the theoretical prediction (e) in Figure C1 of Appendix C. The similar features of the twin laminates shown by the magnified views in Figure 4.3 and Figure 4.6 imply that although the composition of the transition zone is different (M_1:M_3 in Figure 4.3 and M_2:M_3 in Figure 4.6), the compatible mechanism is the same: the numerous sharp needles near A-phase region to reduce the elastic mismatch while the coarse laminates (or big spikes) far away from A-phase to reduce the number of twin boundaries, i.e., reducing the interfacial energy of the twin boundaries.

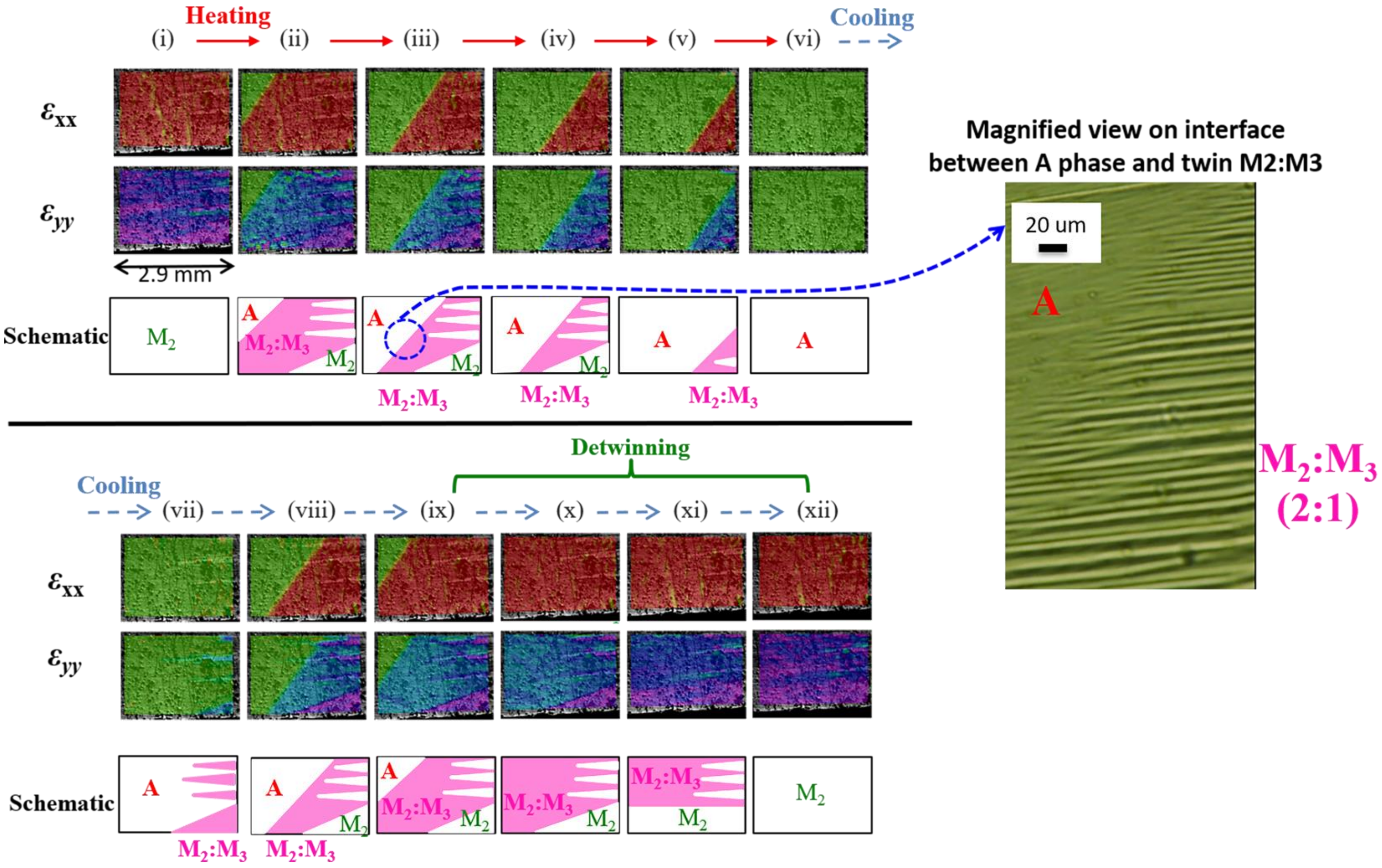

Figure 4.6 The observation by the microscope on the local strain evolution during the heating-cooling cycle of Case (I) “Partial specimen under transformation” with the initial martensite state of M$_2$ in the thin specimen. The transition zone consisting of the twin M$_2$:M$_3$ (with volume ratio 2:1) had a fine-needle pattern near the region of A-phase (shown by the magnified view) and a coarse-arrow pattern near the region of M$_2$.

Section (C): Initial state M_3

To complete the study on the initial-state effect, the same heating-cooling cycle was also performed with the initial martensite state M_3 as shown in Figure 4.7 where the response is similar to that with initial state M_2 in Figure 4.5 in Section (B): both make the specimen elongation (strain ε_{xx}) vary between 0% and 2% because the atomic lattices of both M_2 and M_3 have a long axis along the x-direction, which is contrast to the case of the initial state M_1 in Figure 4.1 of Section (A) where the specimen's elongation varies between 0% and −4%. Moreover, the composition of the transition zone in Figure 4.5 and Figure 4.7 is almost the same — a combination of M_2 and M_3, but with a different volume ratio — the twin M_3:M_2 = 2:1 for the initial state M_3 (see state t_6 in Figure 4.7) while the twin M_2:M_3 = 2:1 for the initial state M_2 (see state t_7 in Figure 4.5). Comparing these compositions with those for the initial state M_1 (M_1:M_2 = 2:1 or M_1:M_3 = 2:1 in Fig. 2), we can see that the initial state (the single variant in the untransformed region) is always the major component of the twin in the transition zone.

Remark 2: The above results with the different initial states not only illustrate the important role of the compatibility in the martensite formation, but also imply that the specimen has no strong microstructure defect or microstructure training effect. In other words, the specimen has no intrinsic preference for any one of the martensite variants M_1, M_2 and M_3. Their appearance in the transforming region (at the half specimen near the clamping end) depends on the initial state of the untransformed region (the other half near the free end). That means, we can utilize this "partial-transformation" method to control the cooled-down martensite formation to achieve a stress-free two-way memory — leading to the cyclic elongation (with the initial state M_2 or M_3) or the contraction along x-direction (with initial state M_1).

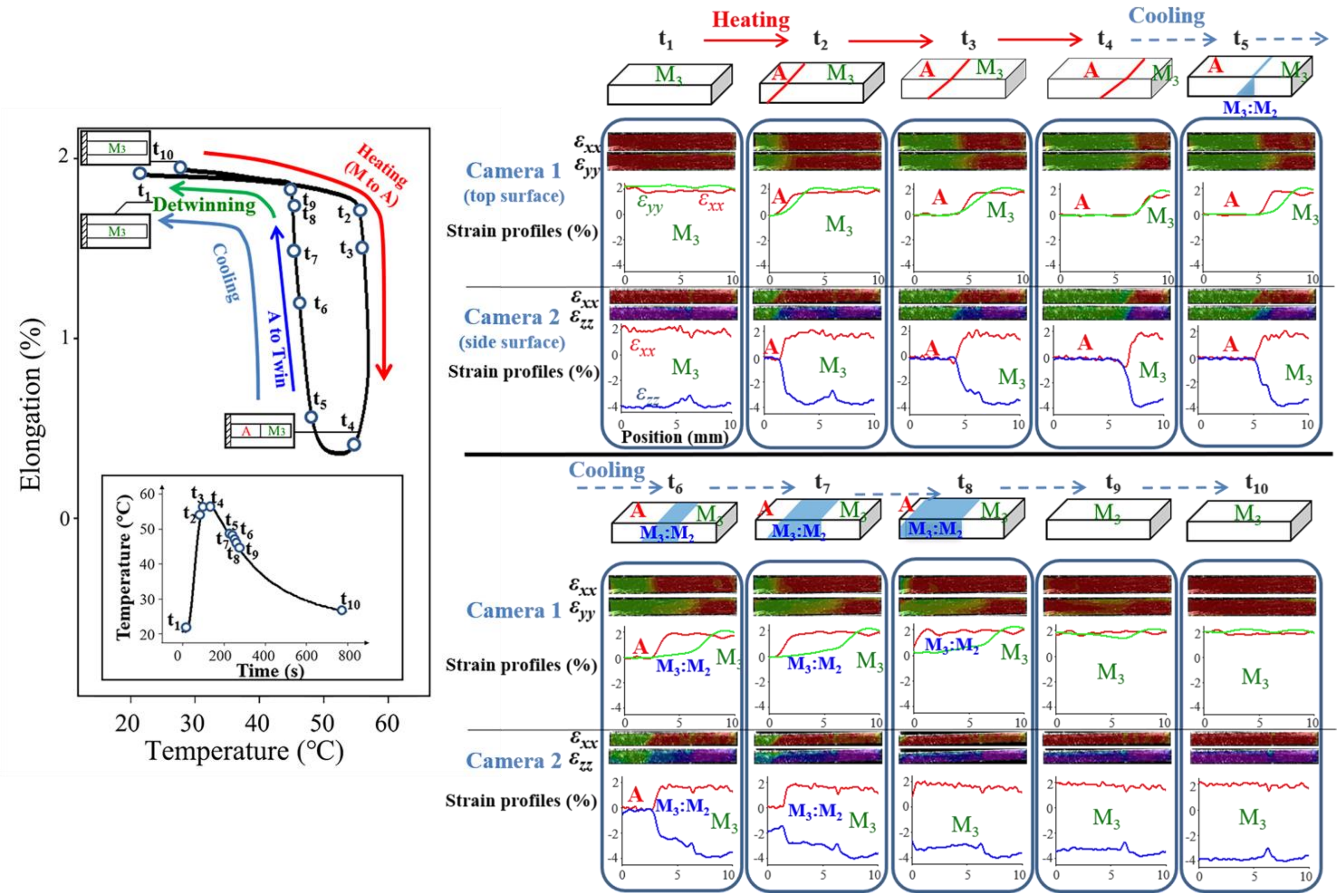

Figure 4.7 The specimen's global elongation and the local strain evolution during the heating-cooling cycle of Case (I) "Partial specimen under transformation" with the initial martensite state of M_3 in the thin specimen. The transition zone of the twin M_3:M_2 (with volume ratio 2:1) was clearly captured during the cooling process. The heating-cooling cycle led to the cyclic A-M phase transformation with a significant cyclic deformation and the single variant M_3 occupied the specimen at both the initial and final states of the cycle.

4.3.1.1.2 Case (II) — “Whole specimen under transformation”

When we performed the heating process with a higher temperature at the clamping end (e.g., $T_{max} \approx 100$ °C), the whole specimen was transformed to A-phase, in spite of the initial martensite states at low temperature. So, in this case, only the cooling process is interesting and shown in Figure 4.8 where the whole specimen was initially occupied by A-phase (see the state t_1 with the strains $\varepsilon_{xx} \approx \varepsilon_{yy} \approx \varepsilon_{zz} \approx 0\%$). Then, the heater was turned off and the specimen naturally cooled down to trigger the A → M phase transformation via the nucleation and growth of a martensite twin M_3:M_1 (with volume ratio 2:1) as shown in the strain maps (t_2) ~ (t_5). It is seen that the interface between the A-phase and the twin M_3:M_1 is almost parallel to the *x*-direction, which satisfies the compatibility requirement as predicted in (a) in Figure C1 in Appendix C. Because the average strain ε_{xx} of the twin M_3:M_1 is around zero, the transformation (A → twin M_3:M_1) has little contribution to the specimen’s elongation (see t_1 ~ t_5 in the elongation-temperature curve in Figure 4.8). When the twin almost occupied the whole specimen (see the state t_5 of Figure 4.8), a domain near the specimen’s free end (at the position $x \approx 7$ mm) took the detwinning process (M_3:M_1 twin → M_3): the major component of the twin (i.e., M_3) grew at the expense of the minor component (M_1). Then, another domain with detwinning into M_3 appeared near the clamping end (see the states t_6 and t_7 of Figure 4.8). The two domains of M_3 grew up and merged to occupy the whole specimen as shown in t_7 ~ t_{10} of Figure 4.8, contributing to a significant elongation: the specimen’s average ε_{xx} increased from 0% to near 1.6% as shown by the elongation-temperature curve in Figure 4.8.

Remark 3: The above result of the “whole specimen under transformation” demonstrates that even though without the initial martensite effect, the cooling-induced A → M phase transformation is still via two steps: A → twin (here M_3:M_1) → single variant (the twin’s major component M_3).

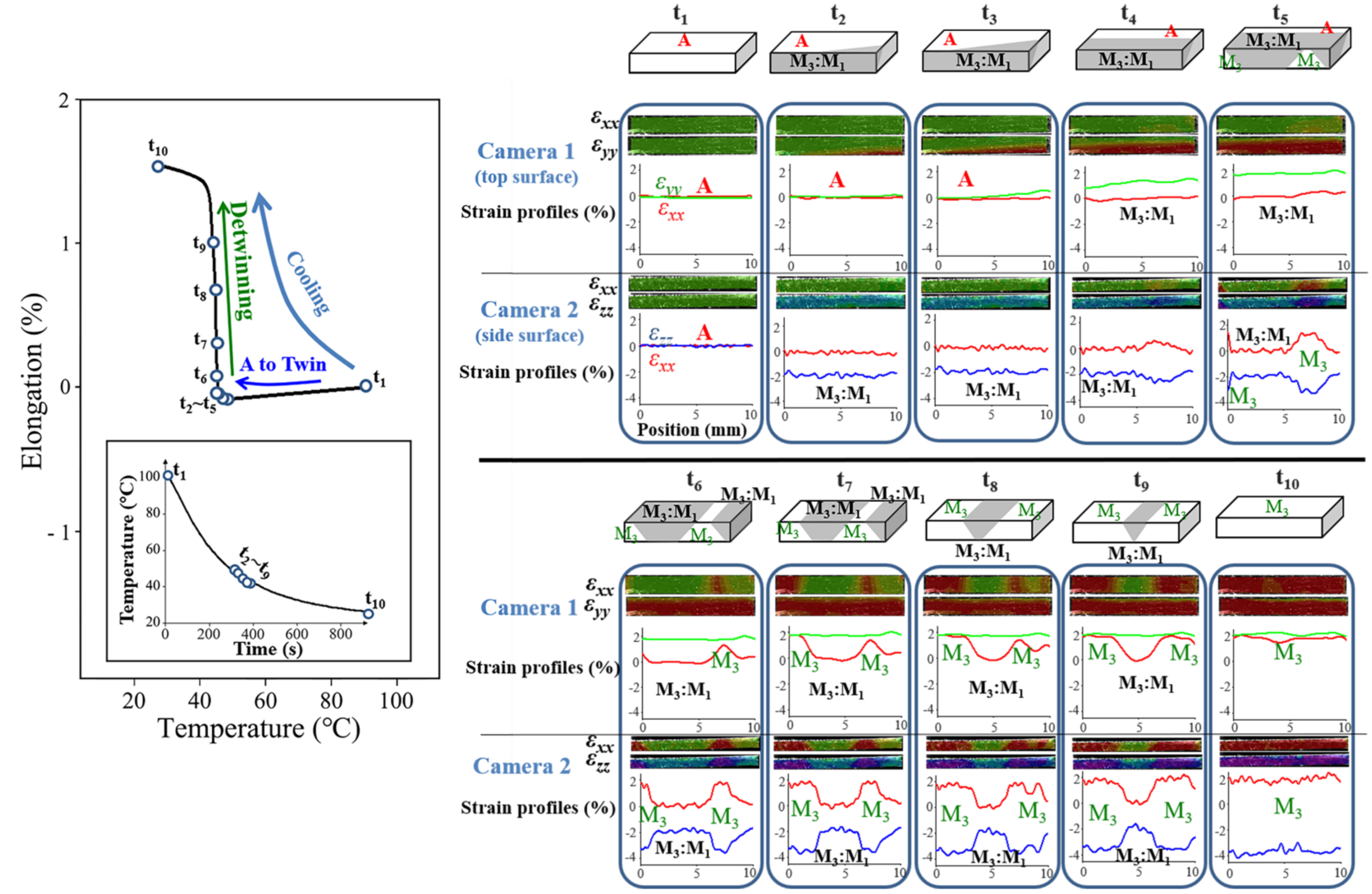

Figure 4.8 The specimen’s global elongation and the local strain evolution during the natural cooling of Case (II) “Whole specimen under transformation” in the thin specimen. The A → M transformation was via two steps: A → twin M_3:M_1 (with volume ratio 2:1) and the detwinning into the single variant M_3. The specimen’s global elongation was mainly due to the detwinning at $t_5 \sim t_{10}$.

4.3.1.2 Martensite formation in thin specimen by “ice local cooling”

The above natural cooling (with the heat transfer from the specimen to the ambient mainly via the specimen’s surfaces) leads to the A-twin interface parallel to *x*-direction (see t_4 and t_5 in Figure 4.8); by contrast, the ice cooling at the clamping end makes the heat transfer mainly along the *x*-direction (i.e., a strong thermal gradient along *x*-direction) and generates a A-twin interface propagating along the *x*-direction as shown in Figure 4.9.

As shown in the temperature-time curve in Figure 4.9, when the specimen (initially A phase) naturally cooled down to near 55 ^{o}C (at the state t_1), a piece of ice was put at the clamping end to decrease the specimen’s temperature quickly; within 10 seconds the A → M transformation (A → twin and detwinning) was triggered to generate the specimen’s elongation near 2% (see t_2 ~ t_9 in the temperature-time curve and the elongation-temperature curve in Figure 4.9). At the beginning of the transformation, a twin M_3:M_2 (2:1) appeared at the clamping end, whose strain components ε_{xx} = 2%, ε_{yy} = 0% and ε_{zz} = –2% as shown in the strain maps at t_2 of Figure 4.9. Then, the twin grew up to occupy the whole specimen (see t_2 ~ t_5) and most of the twin was detwinned into a single variant M_3 (see t_5 ~ t_{10}) with only a small residual part of the twin. As shown in the elongation-temperature curve in Figure 4.9, it is the A→twin transformation rather than the detwinning that contributes to the major elongation of the specimen (average strain ε_{xx}).

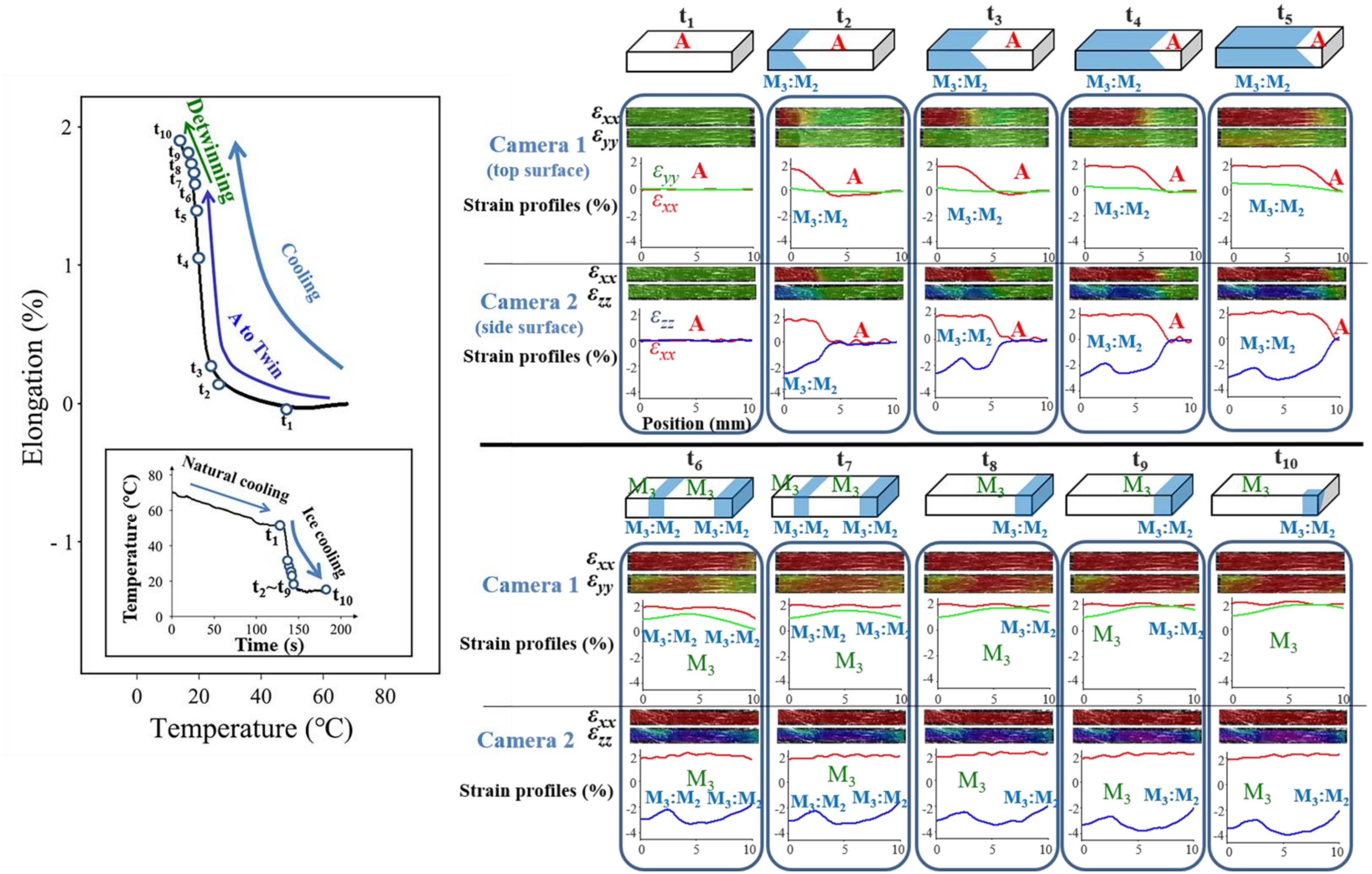

Figure 4.9 The specimen's global elongation and the local strain evolution during the ice local cooling process of the "whole specimen under transformation" in the thin specimen. The A → M transformation was via two steps: A → twin M_3:M_2 (with volume ratio 2:1) and the detwinning into the single variant M_3. The specimen's global elongation was mainly due to the A → twin transformation.

Remark 4: Comparing the twin formation in the ice cooling process (M_3:M_2 = 2:1) with that in the natural cooling in Section 4.3.1.1.2 (M_3:M_1 = 2:1), we can see that the different cooling mode can influence the A-twin interface orientation, the propagating direction and the associated twin composition. Because the twin composition is different in the two cooling modes, the significant elongation of the specimen occurs in different stages: the transformation A → twin (M_3:M_2) contributes to the main elongation in the ice cooling (Figure 4.9) while the stage of detwinning (from the twin M_3:M_1 to M_3) makes the main contribution in the natural cooling (Figure 4.8). On the other hand, there is a common feature in these two cooling processes: the single martensite variant resulted from the detwinning is the major component of the twins; because M_3 is the major component of the twins (M_3:M_2 = 2:1 and M_3:M_1 = 2:1), both the cooling processes have the same final state (M_3).

4.3.2 Martensite formation in thick specimen

To verify the specimen's geometric effect on the martensite formation, we applied the two cooling modes ("natural cooling" and "ice local cooling") on the thick specimen, which are described by the two following subsections, respectively.

4.3.2.1 Martensite formation in thick specimen by "natural cooling"

As shown in Figure 4.10, the thick specimen of initial A-phase (state t_1) at high temperature (around 85 ^{o}C) was naturally cooled down to room temperature, transforming into a complicated configuration consisting of multiple martensite twins (state t_{10}). At the beginning of the phase transformation, two twins M_2:M_1 (2:1) and M_3:M_1 (2:1) appeared with the A-twin interfaces parallel to *x*-direction (see state t_2). But another twin (M_3:M_2 = 2:1) was soon nucleated at the specimen's free end and grew up at the expense of A phase and a part of the previously nucleated twins M_2:M_1 and M_3:M_1 (see t_3-t_6 in Figure 4.10).

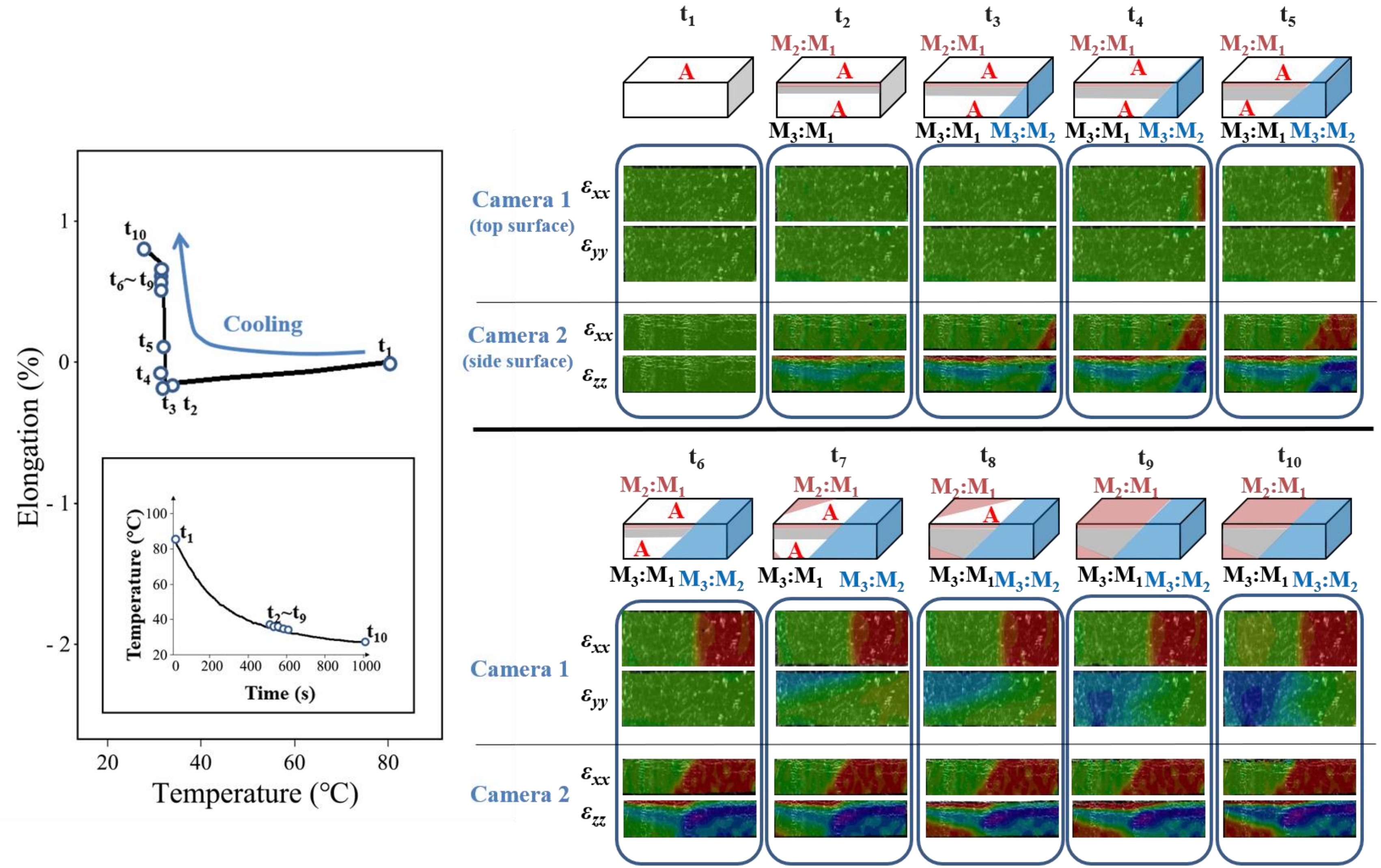

Figure 4.10 A typical evolution pattern in the thick specimen during the natural cooling process: Multiple twins, M_2:M_1 (2:1), M_3:M_1 (2:1) and M_3:M_2 (2:1) were formed.

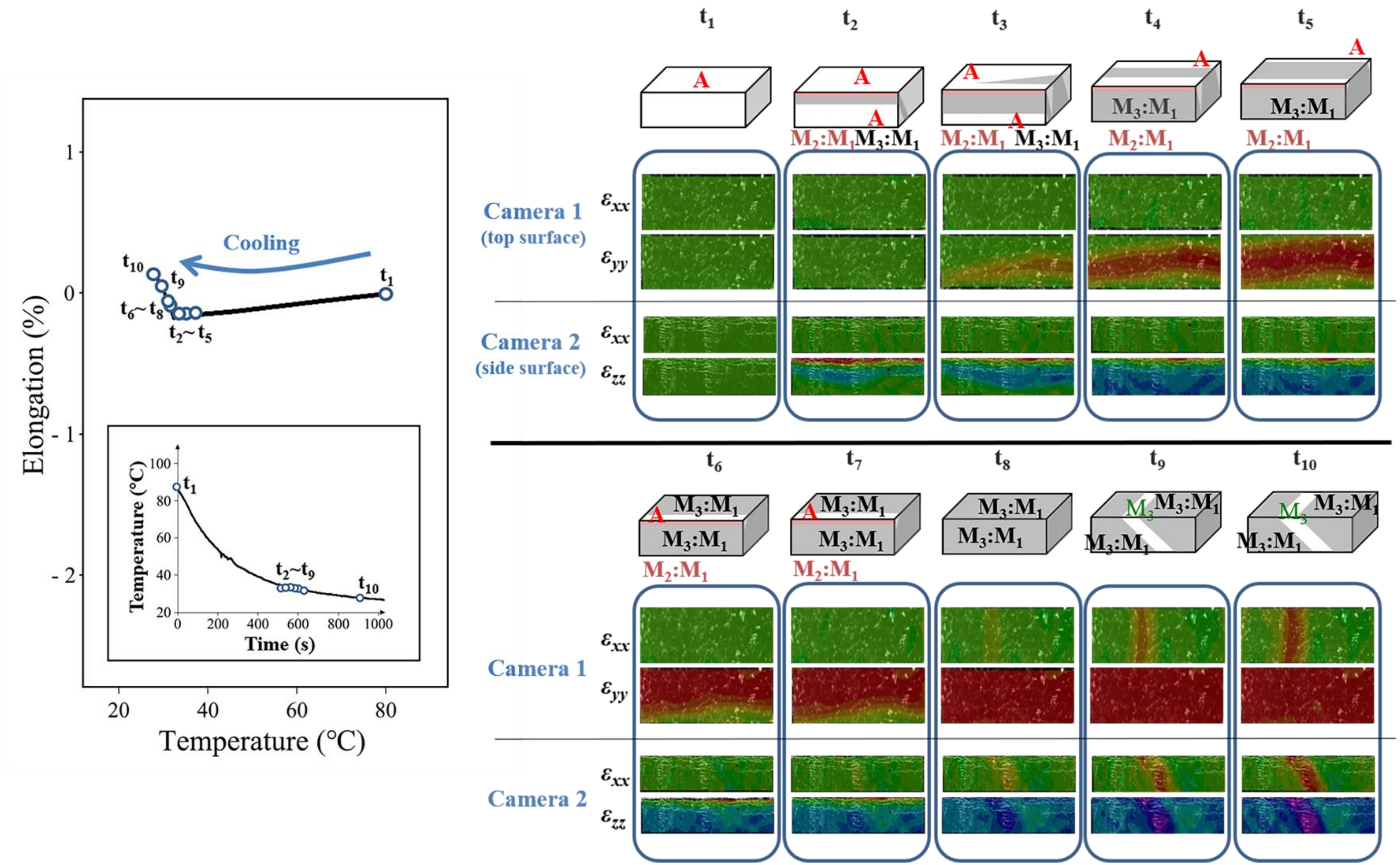

Figure 4.11 Another typical pattern in the thick specimen during the natural cooling process: Two twins M_2:M_1 (2:1) and M_3:M_1 (2:1) were firstly nucleated; after competition, only one twin dominated with little detwinning.

Then, another domain of the twin M_2:M_1 (2:1) appeared at the specimen's top surface near the clamping end (t_7 ~ t_9). During the twins' nucleation and grown-up, no obvious detwinning was observed. Finally, these twins shared the specimen in a complicated pattern and the specimen's global elongation was less than 1% (see the state t_{10}). However, this complicated pattern was not the unique configuration observed in the experiments on the thick specimen. Another pattern is shown in Figure 4.11 where the same two twins (M_2:M_1 = 2:1 and M_3:M_1 = 2:1) were nucleated at the beginning of the transformation at state t_2. Then, the twin M_3:M_1 grew up from the specimen's free end to the clamping end and occupied almost the whole specimen while the twin M_2:M_1 gradually disappeared (see the states t_3 ~ t_7). When the last regions of the A-phase and the twin M_2:M_1 disappeared (t_7 ~ t_9), the detwinning process started (from twin M_3:M_1 to single variant M_3). However, the detwinning was soon arrested within a small region (see state t_{10}). At the end of the natural cooling process, the specimen was mainly occupied by the twin M_3:M_1 with a small domain of the single variant M_3, making the specimen's elongation very small (close to zero as shown by the elongation-temperature curve in Figure 4.11).

Remark 5: Compared to the thin specimen, the thick specimen has more space to allow the nucleation and the growth of the multiple martensite twins in the natural cooling process. That means, the ambient heat convection cools all the specimen's surfaces simultaneously, making possible the simultaneous nucleation of multiple twins. When the multiple twins meet one another, their further evolution is prohibited, so-called "interlocking" (Zreihan et al., 2019) and the detwinning to single variant becomes difficult. Then, the overall average strain of the specimen is small. Such behaviour is somehow like self-accommodation — with little change in the global shape during the cooling-induced martensitic phase transformation.

4.3.2.2 Martensite formation in thick specimen by “ice cooling”

By contrast to the natural cooling studied above, the ice local cooling at the specimen’s clamping end makes the transformation happen in order (in sequence from the clamping end to the free end) rather than simultaneous transformation at multiple locations in the specimen. As shown in Figure 4.12, when the ice cooling was applied, the temperature at the clamping end dropped significantly and the twin M_1:M_2 = 2:1 was nucleated (see the state t_2). When the twin grew up by the A-twin interface propagating towards to the free end, the twin at the region near the clamping end was detwinned into the single variant M_1 (see the states t_3 ~ t_5). Finally at the end of the cooling, M_1 occupied the whole specimen, leading to the elongation strain near −4% as shown by the elongation-temperature curve in Figure 4.12. Similarly, such twin formation is not the unique evolution pattern in the thick specimen in the ice local cooling process. Another twin formation is shown in Figure 4.13 where the twin M_3:M_2 (2:1) rather than M_1:M_2 was nucleated. It is seen at t_2 ~ t_4 that the twin M_3:M_2 (2:1) grew up without detwinning into the single variant M_3, probably due to another twin M_2:M_3 (2:1) nucleated at the specimen’s free end as shown by the final state (t_5) in Figure 4.13. Because both the variants M_2 and M_3 have their long axes along *x*-direction, both the twins M_3:M_2 (2:1) and M_2:M_3 (2:1) contribute to the specimen’s elongation during the A → twin transformation, even though detwinning does not occur.

Remark 6: The comparison between the natural cooling and the ice local cooling in the thick specimen (Section 4.3.2.1 and Section 4.3.2.2) indicates that the strong local cooling (with a large temperature gradient along the specimen’s length direction) can keep only one A-M interface propagating through the specimen to avoid complex multiple-twin formation. Such single A-M interface normally leads to the formation of only one martensite twin.

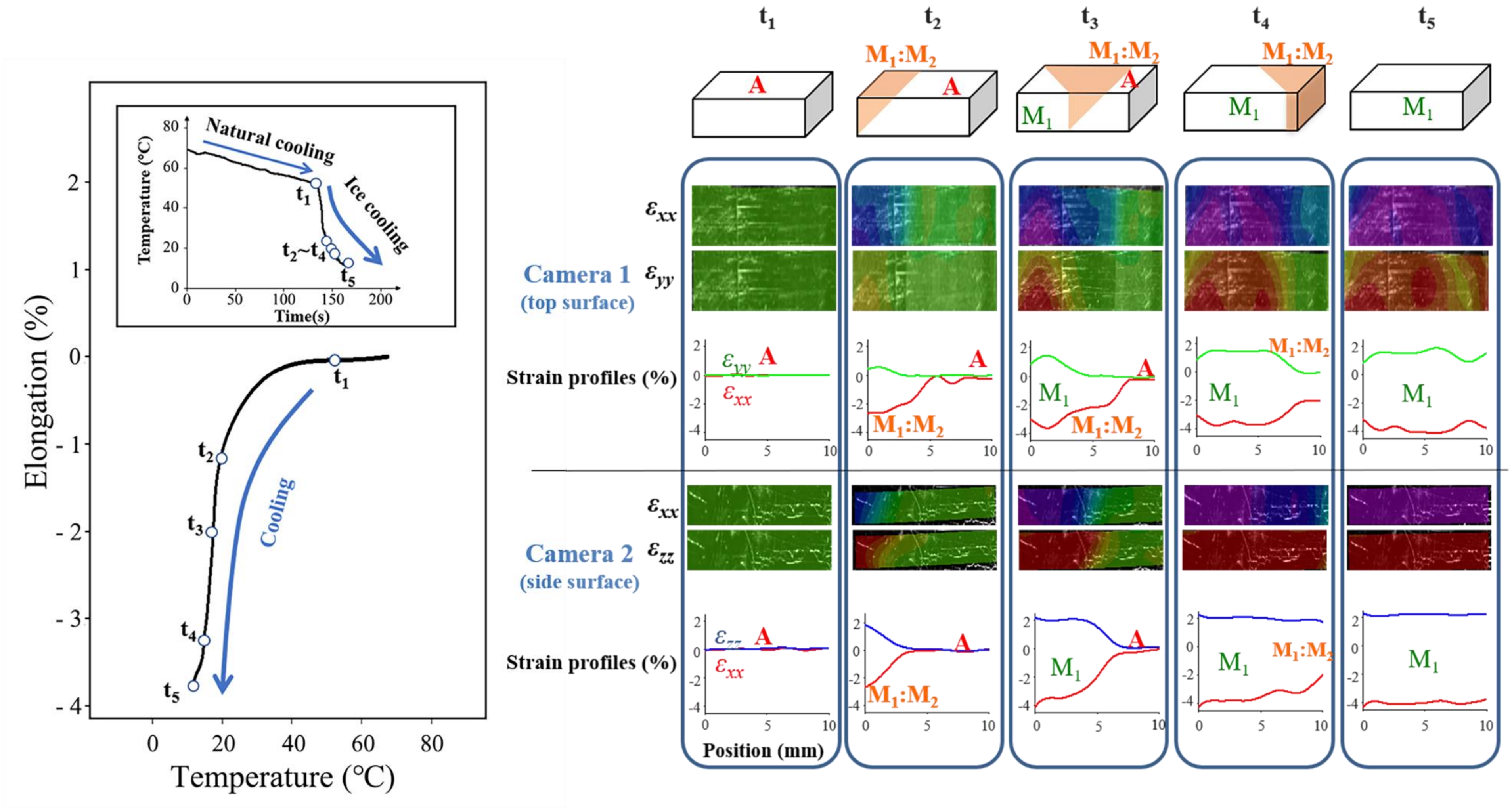

Figure 4.12 A typical evolution pattern in the thick specimen during the ice local cooling process: only one twin, M_1:M_2 (2:1) was nucleated and grew up via an A-twin interface propagating along the specimen's length direction; finally the major component of the twin (here the single variant M_1) dominated by the detwinning.

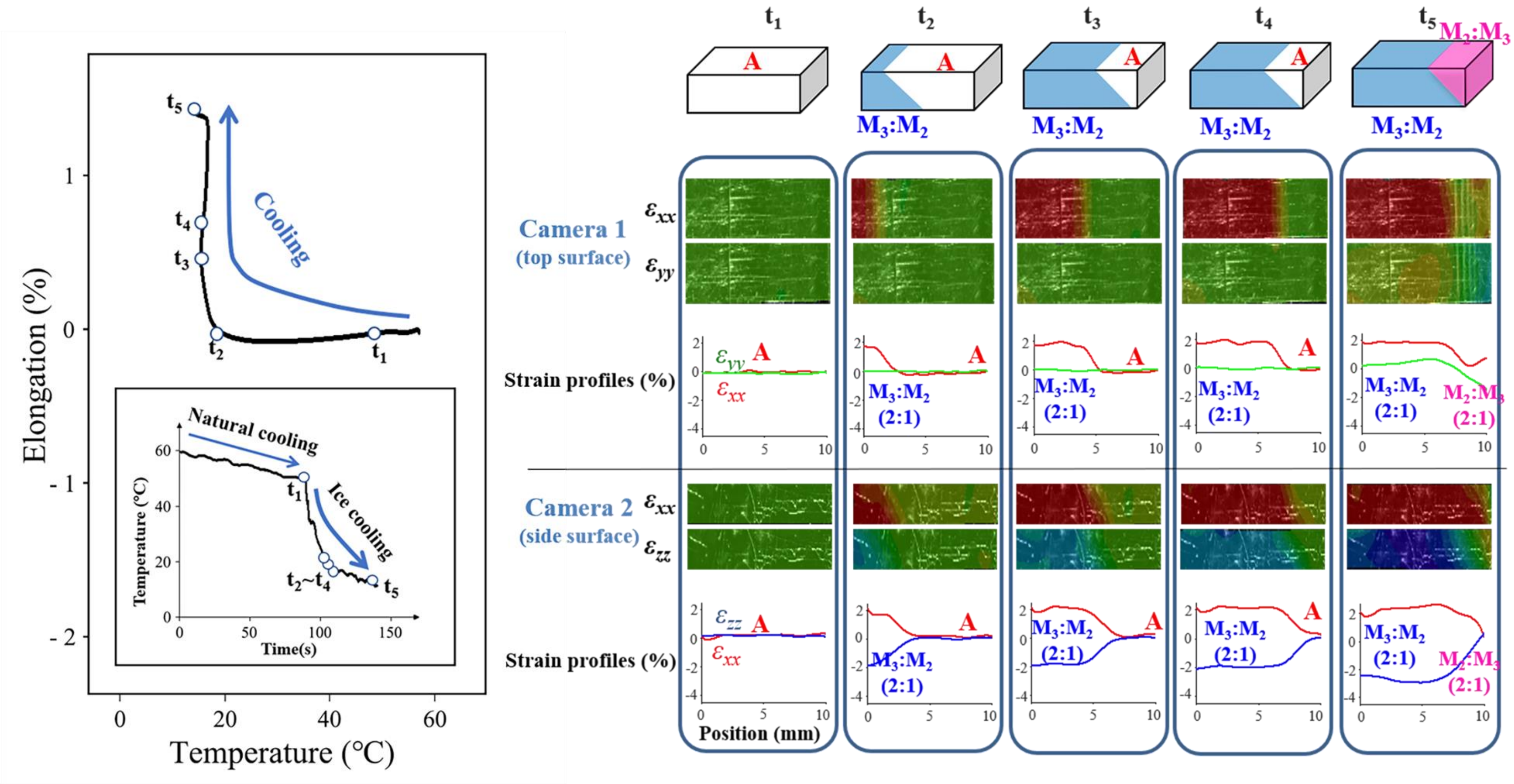

Figure 4.13 Another typical evolution pattern in the thick specimen during the ice local cooling process: one twin, M_3:M_2 (2:1) was firstly nucleated at the specimen's clamping end and grew up via an A-twin interface propagating along the specimen's length direction; but it was arrested by the nucleation of another twin, M_2:M_3 (2:1) at the specimen's free end.

4.4 Discussion

Current experiments reported in Section 4.3 show that the martensitic phase transformation always starts with the A → twin transformation where the martensite twin has a specific composition: two different martensite variants with the volume ratio 2:1 or 1:2, because a single martensite variant of tetragonal symmetry cannot be compatible directly with the austenite phase of cubic symmetry. These compatible twins and the associated A-twin interface's orientations can be determined by a simple compatibility analysis as shown in Appendix C where we can see in Figure C1 that there are totally six possible compositions. In fact, all these six twins (M_1:M_2, M_1:M_3, and M_2:M_3 with the volume ratios 2:1 or 1:2) have been observed in current experiments; and only these six twins were observed at the A-M interfaces. That means, the compatibility plays an important role in the twin formations in both types of specimens and in both cooling modes.

After the A → twin transformation during the cooling, the twin can be detwinned into a single martensite variant in certain situations, for example in the thin specimen (Figs. 2 ~ 10) for both the cases of "partial" and "whole" specimen under transformation. Such automatic detwinning was the first time to be reported systematically. In literature, the detwinning or the martensite reorientation in the material (Ni-Mn-Ga) was reported in the experiments with a mechanical stress or a magnetic field (Karaca et al., 2006; Pagounis et al., 2014; Pascan et al., 2015; Peng et al., 2015; Smith et al., 2014; Zhang et al., 2018a, b). But in current experiments without any directional driving forces (without stress or magnetic field), the detwinning occurred automatically after the cooling-induced A → twin transformation. One of the possible reasons for such automatic detwinning is the laminate structure of the fine twins as shown by the magnified views in Figure 4.3 and Figure 4.6. Because the neighbouring twin boundaries in the laminate are so close to each other, the merging and annihilation of the twin boundaries (so to reduce the interfacial energy) can provide the driving forces for this automatic detwinning (Heczko et al., 2018; James et al., 1995; Stupkiewicz et al., 2007; Waitz et al., 2008; Zhang et al., 2009). Such interface merging has an analogy in NiTi polycrystals where the neighbouring fronts of Lüders bands can merge and release latent heat to cause a large local temperature change (He and Sun, 2010; Iadicola and Shaw, 2004; Zhang et al., 2010). Further exploration of the detwinning mechanism might need higher-resolution observation on the fine twin structures and the associated compatibility and energy analysis (Balandraud and Zanzotto, 2007; Ball and James, 1987; Chulist et al., 2019; O'Handley R.C. et al., 2003; Ruddock, 1994).

Some researchers might think that the detwinning could be due to the microstructure defects (created during the material's manufacturing) or specific training effect (Chmielus et al., 2008), which prefers a certain martensite variant. For example, in the references (Novák et al., 2006; Wang et al., 2000; Yuan et al., 2019), although the cooling-induced deformation in SMA single crystals was clearly observed, the articles' authors attributed it to imperfection or training effect without further detailed verification/discussion. And some theoretical researchers usually model the stress-free cooling-induced martensitic phase transformation in single crystal by assuming "self-accommodation" (Seiner et al., 2008; Zhou et al., 2020). However, the current experiments in Section 4.3 have demonstrated that the "self-accommodation" is **not** an intrinsic necessary configuration in the cooling-induced martensitic phase transformation, and that the specimens tested in the current experiments have no strong preference on a certain variant; for example, the thin specimen can be cooled down to be M_1, M_2 and M_3 in Figure 4.1~ 4.9. Even though microstructure defects are unavoidable during the material manufacturing, their effect is not important as the influences of the compatibility and the associated interfacial energy, which govern the twin formation and the detwinning. All the observed A-twin interface orientations and the twins' composition agree with the theoretical compatibility predictions in Figure C1, and the detwinning process occurs by the growth of the major component of the twin at the expense of the minor component (the variant with the smaller volume ratio), i.e., the nearest neighbouring twin boundaries merging each other leads to the disappearance of the minor component. Therefore, the observed martensite formation — twin formation and the detwinning can be understood/explained by the compatibility and the interfacial energy rather than the vague microstructure defects.

On the other hand, the "self-accommodation" can be achieved as implied by the comparison of the twin formation between the thin specimen and the thick specimen under the natural cooling (Figure 4.8 for the thin specimen and Figure 4.10 and Figure 4.11 for the thick specimen). Although the thickness of the thick sample (2 mm) is just two times that of the thin sample (1 mm), the thick specimen provides enough space for the nucleation and growth of multiple twins, and the interaction between the twins prohibited the detwinning process, leading to a small level in the specimen's overall elongation. We can imagine that, by contrast to the slim specimens/bars tested in current experiments, a bulk single crystal under homogenous cooling would have much more space to allow all the possible compatible twins to appear simultaneously leading to the approximately unchanged global shape, similar to the self-accommodation configuration. Moreover, the self-accommodation is more easily achieved in usual SMA polycrystals where the numerous non-transformable grain boundaries provide geometric constraints to prefer an unchanged global shape as in the references (Aydogdu et al., 2002; Madangopal, 1997; Miyazaki S. et al., 1989; Waitz, 2005) where the self-accommodation configurations have been observed in several types of polycrystalline SMAs. However, when the grain size of the polycrystals is too small to provide space for multiple twins, the self-accommodation would not be possible (Gu et al., 2018; Schryversa et al., 2002; Teramoto et al., 2020; Waitz et al., 2008). Therefore, the self-accommodation configuration is mainly from geometric effects. For the slim SMA single crystals like the thin specimen in current experiments, the cooling-induced martensite structure is far from the self-accommodation configuration.

Even though the single crystal specimen is not so slim, controlling the cooling mode can avoid the simultaneous nucleation of multiple twins so that the resulted martensite structure can be far from self-accommodation as shown in Figure 4.12 and Figure 4.13 where the thick specimen is under the ice local cooling with a strong thermal gradient along the specimen's length direction. In that situation, only four possible twins can be formed, M_3:M_2 (with the volume ratio 1:2 or 2:1), M_1:M_2 (2:1) and M_1:M_3 (2:1) whose A-twin compatible interfaces are not parallel to *x*-direction as shown in Figure C1 in Appendix C. Among the four possible twins, two were observed in current experiments (M_1:M_2 in Figure 4.12 and M_3:M_2 in Figure 4.13). That means, we can control the cooling mode (e.g., ice local cooling) to make the martensite structure far from self-accommodation: the cooled martensite structure consists of only one twin (or one single variant by further detwinning) rather than multiple twins; but we are not able to predict which twin will eventually win out.

Once the non-self-accommodation martensite structure (twin or single variant) is achieved, the heating-cooling cycle triggering the A ↔ M transformation can lead to cyclic global deformation; that means, the so-called stress-free two-way memory can be realized without any special training process. Particularly, when the complete transformation process takes place (i.e., A → twin → single variant) as shown in Figure 4.12 (with final state M_1) and in Figure 4.9 (with final state M_3), the specimen's elongation can change between 0%

(austenite phase) and −4% (with final cooled state M_1) or +2% (with final cooled state M_3). Because we cannot predict which twin or which single martensite variant will eventually win out, it is better to call it a three-way memory as there are three characteristic levels of the specimen's elongation during the heating-cooling cycle, 0% (austenite phase), −4% (single variant M_1 whose short axis "c" is along the *x*-direction) and +2% (single variant M_2 or M_3 which has a long axis along the *x*-direction). That means, in the same specimen by the same cooling mode, the cooling-induced A → M phase transformation can make the specimen elongate or contract, which is not predictable or controllable. In order to control the deformation mode (elongation or contraction), the current experiments about the case of "partial specimen under transformation" (Section 4.3.1.1.1) provide a method: let only part of the specimen take the cyclic phase transformation; then the initial state (the single martensite variant) of the untransformed part of the specimen would govern the cooling-induced martensite formation in the transforming part of the specimen via the compatibility requirement so to control the specimen's deformation mode as shown in Figure 4.1 where the initial state M_1 leads to the specimen's contraction during cooling, Figure 4.5 and Figure 4.7 where the initial state M_2 and M_3 trigger elongation during cooling.

4.5 Summary and conclusions

This chapter reports the experiments on single crystal Ni-Mn-Ga bars of different geometric sizes under different heating-cooling cycles. It is demonstrated that while the self-accommodation martensite structure (without global shape change during cooling) is very common in usual polycrystalline SMAs, it is hardly found in usual slim SMA single crystals like the specimens in current study. In the current experiments, the cooling-induced austenite → martensite transformation can have a large global shape change, which implies the potential applications of the stress-free two-way memory. Although the observed non-self-accommodation martensite structures can be explained with the compatibility analysis, there are still challenging tasks for researchers/engineers to predict/control the cooling-induced martensite structures because the same specimen under the same cooling mode can have different final states (e.g., Figure 4.12 and Figure 4.13) which all satisfy the compatibility. To better grasp the material's behaviour, further researches are demanded, such as the observation with higher resolution and more advanced modelling for the microstructure evolution kinetics. Some preliminary conclusions from the current experiments are listed in the following:

1. The cooling-induced austenite → martensite phase transformation in Ni-Mn-Ga single crystal can take place via two steps: (1) austenite → martensite twin(s); (2) detwinning into single martensite variant. Whether the 2nd step (detwinning) can happen depends on the detailed evolution situations; for example, when multiple twins are nucleated in the 1st step, the detwinning would be weakened or prohibited due to the "interlocking" (inter-constraints) between the twins (Figure 4.10 and Figure 4.11).

2. Non-self-accommodation configuration (a martensite twin or single variant) with a significant global shape change dominates in the cooling-induced martensitic formation in the slim specimen whose limited space avoids multiple-twin nucleation (Figure 4.8 and Figure 4.9).

3. Localized cooling with a strong thermal gradient guarantees the sequential phase transformation by a single A-twin interface propagating through the whole specimen, leading to the non-self-accommodation configuration with a significant global shape change (Figure 4.12 and Figure 4.13).

4. The deformation mode (elongation or contraction) of the stress-free two-way memory can be controlled by the method of the "partial specimen under transformation" via the compatibility influence of a transition zone (a particular twin) between the austenite phase and the initial single martensite variant (Figure 4.1 ~ 4.7).

Chapter 5

Conclusions and perspectives

5.1 Conclusions

Two sets of systematic experiments are performed in this thesis, and their results show that there exists a close relationship between the martensite reorientation and the temperature-induced phase transformation in Ni_2MnGa single crystal.

The first set of the systematic experiments investigates the thermal effect on the magnetic-field-induced strain oscillation of Ni_2MnGa single crystal by stepwise gradually changing thermal boundary condition (from still ambient air to strong airflow). And the dynamic experiments of cyclic rapid switching between different levels of the ambient heat transfer efficiency are also performed. The results reveal that the energy dissipation of the high-frequency martensite reorientation can increase the specimen temperature at weak ambient heat transfer, leading to the phase transformation to austenite phase. The phase transformation can in turn modulate the strain oscillation amplitude by the phase-fraction adjustment.

The second set of the systematic experiments investigates the martensitic phase transformation of the Ni_2MnGa single crystal bars of different geometric sizes under different heating-cooling cycles. It is demonstrated that while the self-accommodation martensite structure (without global shape change during cooling) is very common in usual polycrystalline SMAs, it is hardly found in slim specimens of Ni_2MnGa single crystals. Moreover, the martensite reorientation indeed occurred during the cooling-induced phase transformation without any directional driving force (without stress or magnetic field), leading to a large global shape change.

The interaction between the martensite reorientation and the temperature-induced phase transformation of Ni_2MnGa single crystals will encourage the researchers to better explore the material behaviors and inspire various potential engineering applications.

5.2 Perspectives

The first set of the experiments of this thesis presents a thermal control method on strain modulation of FSMA actuator. Based on this method, further experimental work can be developed under various thermo-magneto-mechanical loadings (changing frequency, field amplitude, ambient temperature, etc.). Besides, more advanced models are also demanded by adding the force balance equation to the present models of the thesis in order to better describe the dynamical behaviors of the specimen. All these experimental and theoretical work are helpful for both fundamental understanding and engineering designs of FSMA actuators.

The second set of the experiments implied that both the specimen geometry and the cooling scheme (thermal gradient) have effects on the self-accommodation properties of Ni_2MnGa single crystal. To verify the specimen geometry's influence, more specimens with variety of the geometries can be used to repeat the heating and cooling test, from the thin films to the rectangular bars with large volumes. This work can inspire that a good selection of specimen geometry can induce a stress-free two-way memory effect in Ni_2MnGa single crystal. Moreover, the thermal gradient effects can be investigated in different thermal gradient values and directions. As there are only two cooling schemes (natural cooling and ice cooling), liquid nitrogen with a much better cooling efficiency than ice can also be used to cool down the specimen locally, for a comparison with the other two cooling schemes. As the ice local cooling only provides a large thermal gradient along the length direction of the specimen in this thesis, it will be very interesting to investigate whether the large thermal gradient along the width direction or the thickness direction can also induce different twins compared to natural cooling scheme.

The spontaneous detwinning phenomenon during the stress-free cooling-induced phase transformation in Ni_2MnGa single crystal should be deeply explored in order to find the driving force for this automatical martensite detwinning without directional driving force. As the temperature is the only variable of the test, the infrared camera can be used to monitor the local temperature distribution of the specimen during the cooling process to verify whether the temperature (thermal gradient) can influence the martensite detwinning. Besides, more precise characterization instruments, such as X-ray Diffraction (XRD) and scanning electron microscopy (SEM) with electron backscatter diffraction (EBSD), can be used to identify which kind of twin boundaries (Type I or Type II twin boundary) is dominant during the cooling-induced phase transformation because there is a magnitude difference of the twinning stress (or the driving forces) between Type I and Type II twin boundaries. If the driving force of the spontaneous martensite detwinning is identified, not only the physical mechanism of this phenomenon can be well understood, but also the potential engineer applications can be reliably developed.

Appendix A One-dimensional heat balance model

The FSMA rectangular bar in Chapter 3 can be approximately viewed as a one-dimensional (1D) bar with a diameter 2R as shown in Figure A1, where the specimen temperature is assumed to be uniform and heated/cooled by the dissipation heat in the specimen and the heat transfer to the ambient respectively.

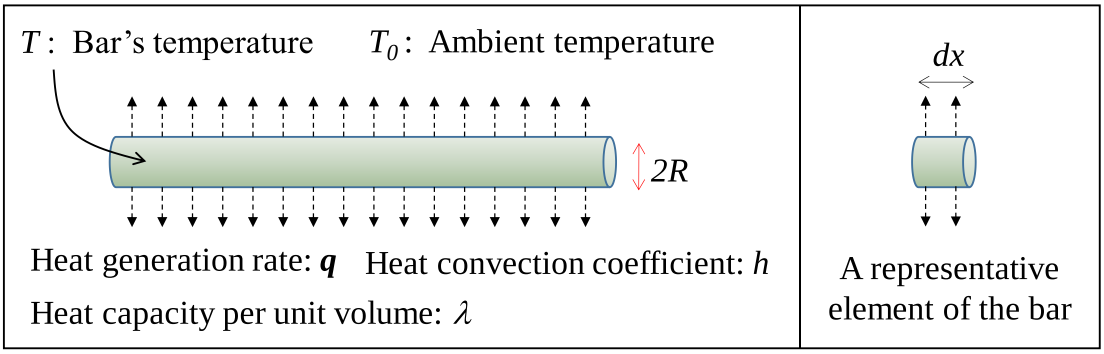

Figure A1. Schematic of the heat balance model of 1D bar.

For a representative element volume $dv = \pi R^2 \cdot dx$ where dx is the length of the element, the temperature variation is governed by the dissipation heat rate $q_{Dissipation}$ in the element volume and the heat convection via the element's surface area $dA = 2\pi R \cdot dx$ as

$$\lambda \cdot dv \cdot dT = q_{Dissipation} \cdot dv \cdot dt - h \cdot (T - T_0) \cdot dA \cdot dt \tag{A1}$$

where T, T_0, λ, and h denote the specimen temperature, the ambient temperature, the material heat capacity per unit volume, and the heat convection coefficient, respectively. Eq. (A1) can be reduced to

$$\frac{dT}{dt} = \frac{q_{Dissipation} - q_{Transfer}}{\lambda} \tag{A2}$$

where

$$q_{Transfer} = \frac{2h \cdot (T - T_0)}{R} \tag{A3}$$

When there is no dissipation heat generation (i.e., $q_{Dissipation} = 0$), Eq. (A2) reduces to

$$\frac{dT}{dt} = \frac{2h \cdot (T - T_0)}{R \cdot \lambda} \tag{A4}$$

whose solution is

$$T = T_0 + (T_{\mathrm{initial}} - T_0) \cdot e^{-\frac{t}{t_h}} \tag{A5}$$

where T_{initial} denote the specimen temperature at $t = 0$ second, and

$$t_h = \frac{R\lambda}{2h} \tag{A6}$$

Equation (A5) and (A6) provide the method to characterize the ambient heat transfer efficiency in Appendix A. With Eq. (A6), Eq. (A3) can be written as

$$q_{Transfer} = \frac{\lambda \cdot (T - T_0)}{t_h} \tag{A7}$$

where all the parameters/variables are measurable.

When there is the heat generation of the martensite reorientation, the heat generation rate $q_{Dissipation}$ is non-zero and can be written as

$$q_{Dissipation} = 2\sigma_{tw} \cdot \Delta\varepsilon \cdot f_{strain} \tag{A8}$$

where σ_{tw}, $\Delta\varepsilon$, and f_{strain} represent the effective twinning stress of the martensite reorientation, the strain amplitude, and the strain frequency, respectively. So, Eqs. (A2), (A8) and (A7) are used in the discussion of Section 3.3.2, corresponding to Eqs. 1(a), 1(b) and 1(c) respectively.

Appendix B Determination of twin's composition via local strains

The three martensite variants M_1, M_2 and M_3 with their short axes along x, y and z respectively are shown in Figure 1.1 where the variant's short axis $c \approx 0.561$ nm, long axis $a \approx 0.595$ nm and the austenite characteristic length $a_0 \approx 0.584$ nm. Therefore, the martensite variants have the deformation strains of –4% and +2% along their short- and long-axis directions respectively, taking austenite phase as the reference. That means the characteristic transformation strains of the three variants are: M_1 ($\varepsilon_{xx} \approx -4\%$, $\varepsilon_{yy} \approx 2\%$, and $\varepsilon_{zz} \approx 2\%$), M_2 ($\varepsilon_{xx} \approx 2\%$, $\varepsilon_{yy} \approx -4\%$, and $\varepsilon_{zz} \approx 2\%$) and M_3 ($\varepsilon_{xx} \approx 2\%$, $\varepsilon_{yy} \approx 2\%$, and $\varepsilon_{zz} \approx -4\%$). As shown by the DIC strain maps in Figures 4.1 ~ 4.13, some regions of the specimen are not transformed to these three single variants, but their combinations. So, we need to determine the volume fractions of M_1, M_2 and M_3 (denoted as f_1, f_2 and f_3) based on the measured local strain components. At the temperature lower than the characteristic phase transformation temperature M_f, the material is in martensite state; so there is a relation between f_1, f_2 and f_3:

$$f_1 + f_2 + f_3 = 1 \tag{B1}$$

Usually two principle strain components can be measured by one camera; for example, the DIC strain maps and profiles of surfaces observed by Camera 1 in Figure 4.1 or by a microscope in Figure 4.2 show the two components ε_{xx} and ε_{yy} of the local strains. Two equations can be derived with these two strain components:

$$\begin{cases} -0.04 f_1 + 0.02 f_2 + 0.02 f_3 = \varepsilon_{xx} & \text{(B2)} \\ 0.02 f_1 - 0.04 f_2 + 0.02 f_3 = \varepsilon_{yy} & \text{(B3)} \end{cases}$$

Combining Eqs. (B1), (B2) and (B3), we obtain the volume fractions:

$$\begin{cases} f_1 = \dfrac{0.02 - \varepsilon_{xx}}{0.06} \\ f_2 = \dfrac{0.02 - \varepsilon_{yy}}{0.06} \\ f_3 = \dfrac{0.02 + \varepsilon_{xx} + \varepsilon_{yy}}{0.06} \end{cases} \tag{B4}$$

Similarly, for the two components ε_{xx} and ε_{zz} of the strain maps measured by Camera 2 in Figure 4.1, two equations can be derived:

$$\begin{cases} -0.04 f_1 + 0.02 f_2 + 0.02 f_3 = \varepsilon_{xx} & \text{(B5)} \\ 0.02 f_1 + 0.02 f_2 - 0.04 f_3 = \varepsilon_{zz} & \text{(B6)} \end{cases}$$

By solving equations (B1), (B5) and (B6), the volume fractions can be obtained:

$$\begin{cases} f_1 = \dfrac{0.02 - \varepsilon_{xx}}{0.06} \\ f_2 = \dfrac{0.02 + \varepsilon_{xx} + \varepsilon_{zz}}{0.06} \\ f_3 = \dfrac{0.02 - \varepsilon_{zz}}{0.06} \end{cases} \tag{B7}$$

Example: The strain maps of (iii) in Figure 4.2 show that, between A-phase and the single variant M$_1$, there is a triangular transtional zone with the strain components $\varepsilon_{xx} \approx -2\%$, $\varepsilon_{yy} \approx 0\%$. Then, Eq. (B4) gives the volume fractions: $f_1 = 2/3$, $f_2 = 1/3$ and $f_3 = 0$. Therefore, this transition zone consists of only two variants M$_1$ and M$_2$ with the volume ratio 2:1, denoted as M$_1$:M$_2$ (2:1).

Appendix C Compatible austenite-twin interfaces

The following compatibility analysis is based on the previous results in (Bhattacharya, 2003; Zhang et al. 2018b). The Bain matrix of the three different tetragonal variants M_1, M_2 and M_3 (whose short axes respectively along *x*, *y* and *z*) are:

$$U_1 = \begin{pmatrix} \beta & 0 & 0 \\ 0 & \alpha & 0 \\ 0 & 0 & \alpha \end{pmatrix} \quad U_2 = \begin{pmatrix} \alpha & 0 & 0 \\ 0 & \beta & 0 \\ 0 & 0 & \alpha \end{pmatrix} \quad U_3 = \begin{pmatrix} \alpha & 0 & 0 \\ 0 & \alpha & 0 \\ 0 & 0 & \beta \end{pmatrix}$$

where $\alpha = \frac{a}{a_0} = 1.0188$ and $\beta = \frac{c}{a_0} = 0.9606$ (a, c and a_0 are the lattice paremeters of the material as shown in Figure 1.1). The compatible interfaces between austenite phase and martensite twins can be obtained by solving the following two equations, so-called twinning equation and the austenite-martensite interface equation:

$$\begin{cases} QU_j - U_i = a \otimes n & \text{(C1)} \\ Q'(\lambda QU_j + (1-\lambda)U_i) = I + b \otimes m & \text{(C2)} \end{cases}$$

where $\boldsymbol{U_i}$ and $\boldsymbol{U_j}$ are the Bain matrix of the *i*th and the *j*th martensite variants; $\boldsymbol{I}$ is an identity second-order tensor representing the Bain matrix of the A-phase; $\boldsymbol{Q}$ represents the rotation of the variant $\boldsymbol{U_i}$ with respect to the variant $\boldsymbol{U_j}$ when the twin is formed; $\boldsymbol{Q'}$ represents the rotation of the martensite twin (consisting of the *i*th and the *j*th martensite variants) with respect to the A-phase; $a \otimes n$ is a dyadic product of a non-zero vector $\boldsymbol{a}$ and a unit vector $\boldsymbol{n}$; the vector $\boldsymbol{n}$ represents the normal of the twinning plane in the reference cubic coordinate system while the vector $\boldsymbol{a}$ is the shearing vector. $\boldsymbol{m}$ is the normal of the A-M interface while the vector $\boldsymbol{b}$ is the shear vector; λ and $(1-\lambda)$ are the fractions of the *i*th and the *j*th martensite variants.

The solutions to the two equations provide all the possible compatible interfaces between austenite phase and martensite twins, which are listed in Table C1, and schematically drawn in Figure C1 for the *x*-*y* plane that were observed by Camera 1 and by the microsope in the experimental results Figures 4.1 ~ 4.13.

Table C1 Theroretical compatible interfaces between austenite phase and martensite twins

Martensite variant- pair $M_i : M_j$	λ (fraction of M_i)	***n*** (normal of fine twin)	***m*** (normal of A-M interface)	Trace of A-M interface (on observation surface)
M_1:M_3	32%	$\frac{1}{\sqrt{2}}[1\ \ 0\ \ 1]$	$\frac{1}{\sqrt{2}}[0\ \ 1\ \ \pm1]$	horizontal (Fig. C1(a))
		$\frac{1}{\sqrt{2}}[1\ \ 0\ -1]$	$\frac{1}{\sqrt{2}}[0\ \ 1\ \ \pm1]$	
	68%	$\frac{1}{\sqrt{2}}[1\ \ 0\ \ 1]$	$\frac{1}{\sqrt{2}}[\pm1\ \ 1\ \ 0]$	45° (Fig. C1(b))
		$\frac{1}{\sqrt{2}}[1\ \ 0\ -1]$	$\frac{1}{\sqrt{2}}[\pm1\ \ 1\ \ 0]$	
M_1:M_2	32%	$\frac{1}{\sqrt{2}}[1\ \ 1\ \ 0]$	$\frac{1}{\sqrt{2}}[0\ \ \pm1\ \ 1]$	horizontal (Fig. C1(c))
		$\frac{1}{\sqrt{2}}[-1\ 1\ \ 0]$	$\frac{1}{\sqrt{2}}[0\ \ \pm1\ \ 1]$	
	68%	$\frac{1}{\sqrt{2}}[1\ \ 1\ \ 0]$	$\frac{1}{\sqrt{2}}[\pm1\ \ 0\ \ 1]$	vertical (Fig. C1(d))
		$\frac{1}{\sqrt{2}}[-1\ 1\ \ 0]$	$\frac{1}{\sqrt{2}}[\pm1\ \ 0\ \ 1]$	
M_3:M_2	32%	$\frac{1}{\sqrt{2}}[0\ \ 1\ \ 1]$	$\frac{1}{\sqrt{2}}[1\ \ \pm1\ \ 0]$	45° (Fig. C1(e))
		$\frac{1}{\sqrt{2}}[0\ -1\ \ 1]$	$\frac{1}{\sqrt{2}}[1\ \ \pm1\ \ 0]$	
	68%	$\frac{1}{\sqrt{2}}[0\ \ 1\ \ 1]$	$\frac{1}{\sqrt{2}}[1\ \ 0\ \ \pm1]$	vertical (Fig. C1(f))
		$\frac{1}{\sqrt{2}}[0\ -1\ \ 1]$	$\frac{1}{\sqrt{2}}[1\ \ 0\ \ \pm1]$	

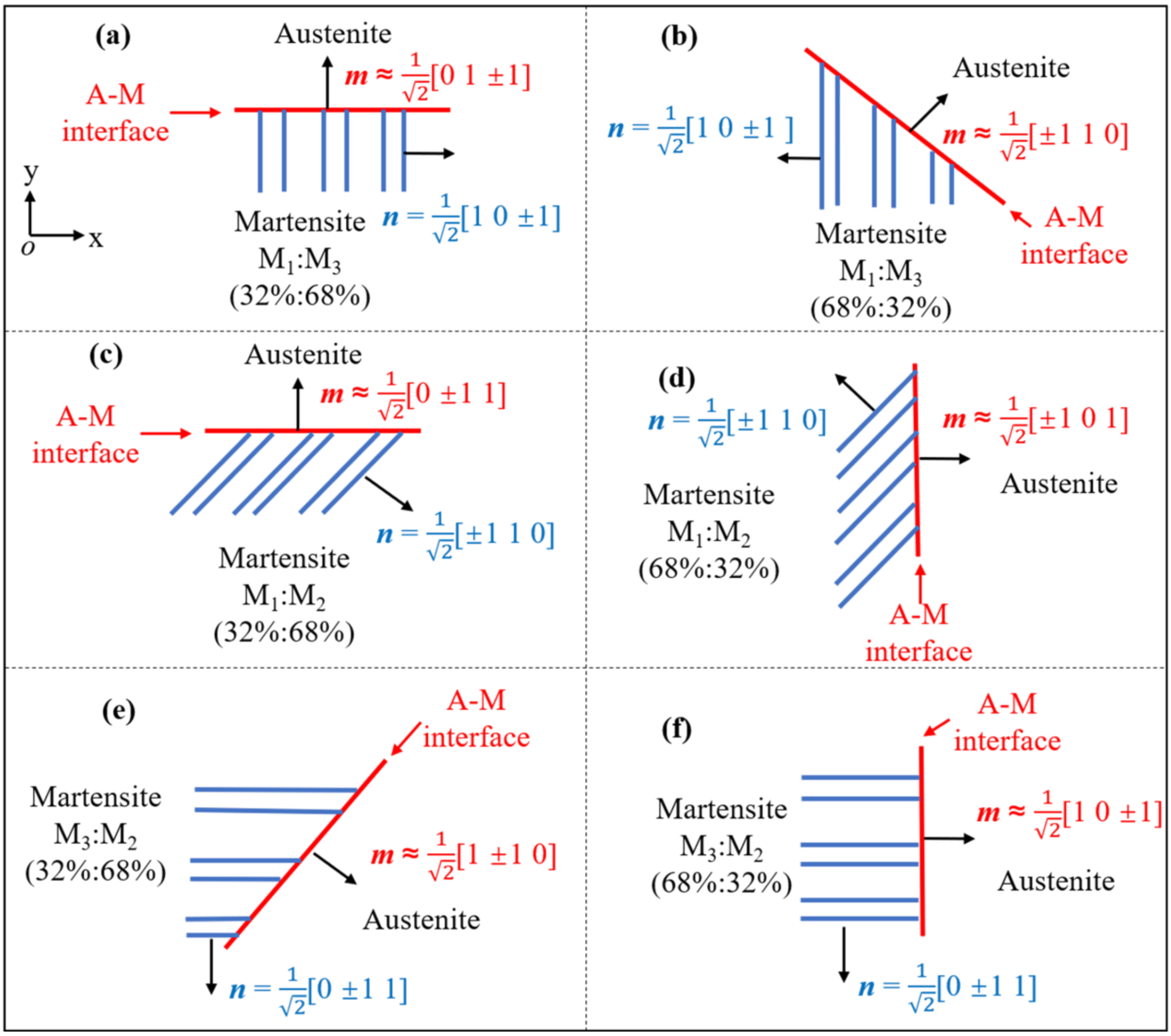

Figure C1 The schematics of the theroretical compatible interfaces between austenite phase and martensite twins

Appendix D Microscope observation of the thick specimen

The microscopic observation is also repeated during the heating and cooling cycles in the thick sample in the case of "partial specimen under transformation". Three different cycles are performed, in which the initial conditions are single variant M_1, M_2 and M_3 respectively (The single variant M_1, M_2 and M_3 are obtained by compressive stress (>10 MPa) along x-, y- and z-directions respectively). The local strain maps ε_{xx} and ε_{yy} and the corresponding schematics of the three cycles are shown in Figure D1, D2 and D3 respectively. The results are similar to the slim specimen (in Section 4.3.1.1.1) showing that the thick specimen has no intrinsic preference for any one of the martensite variants M_1, M_2 and M_3. Their appearance in the transforming region (at the half specimen near the clamping end) depends on the initial state of the untransformed region (the other half near the free end).

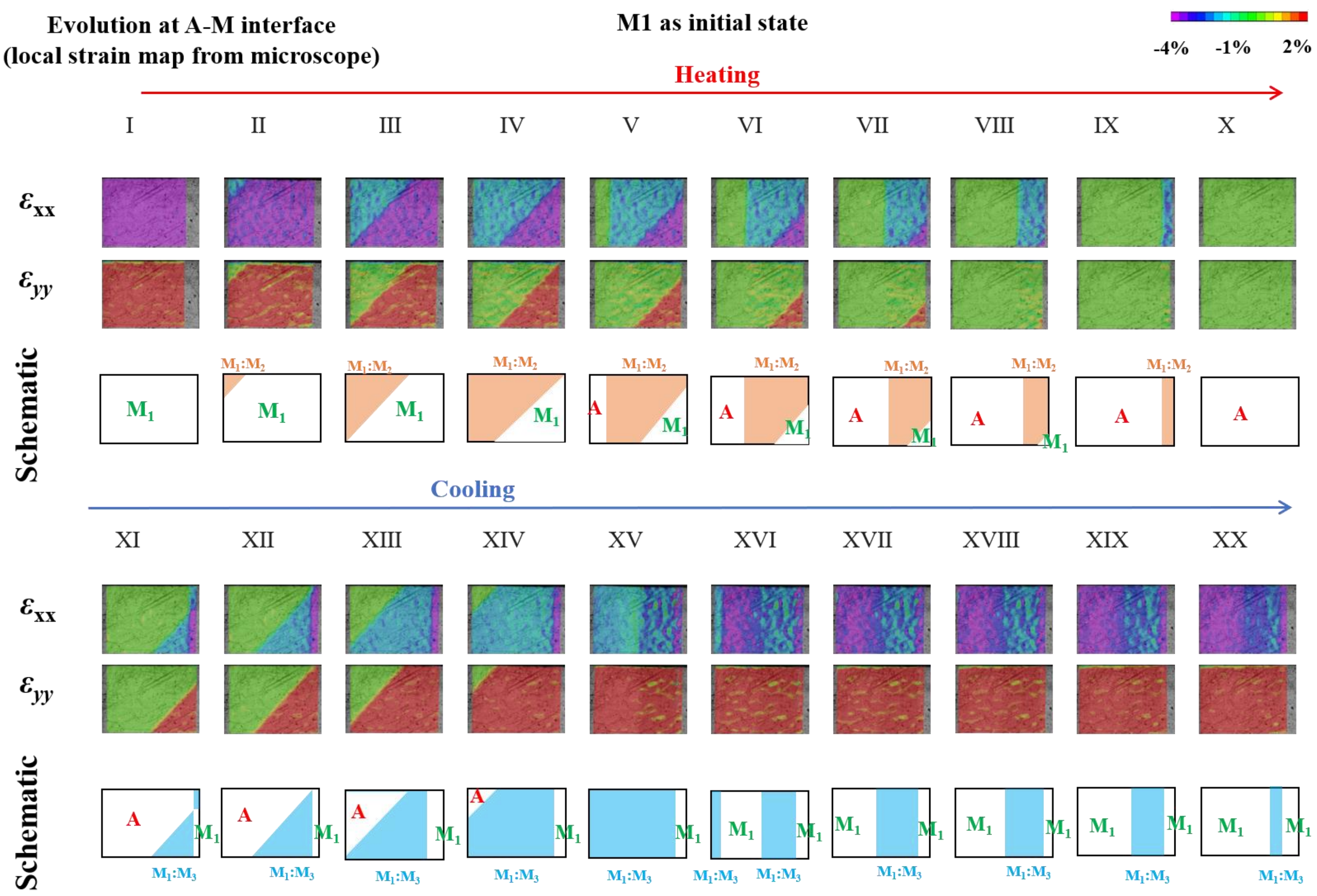

Figure D1 The observation by the microscope on the local strain evolution during the heating-cooling cycle of “Partial specimen under transformation” with the initial martensite state of M_1 in the thick specimen.

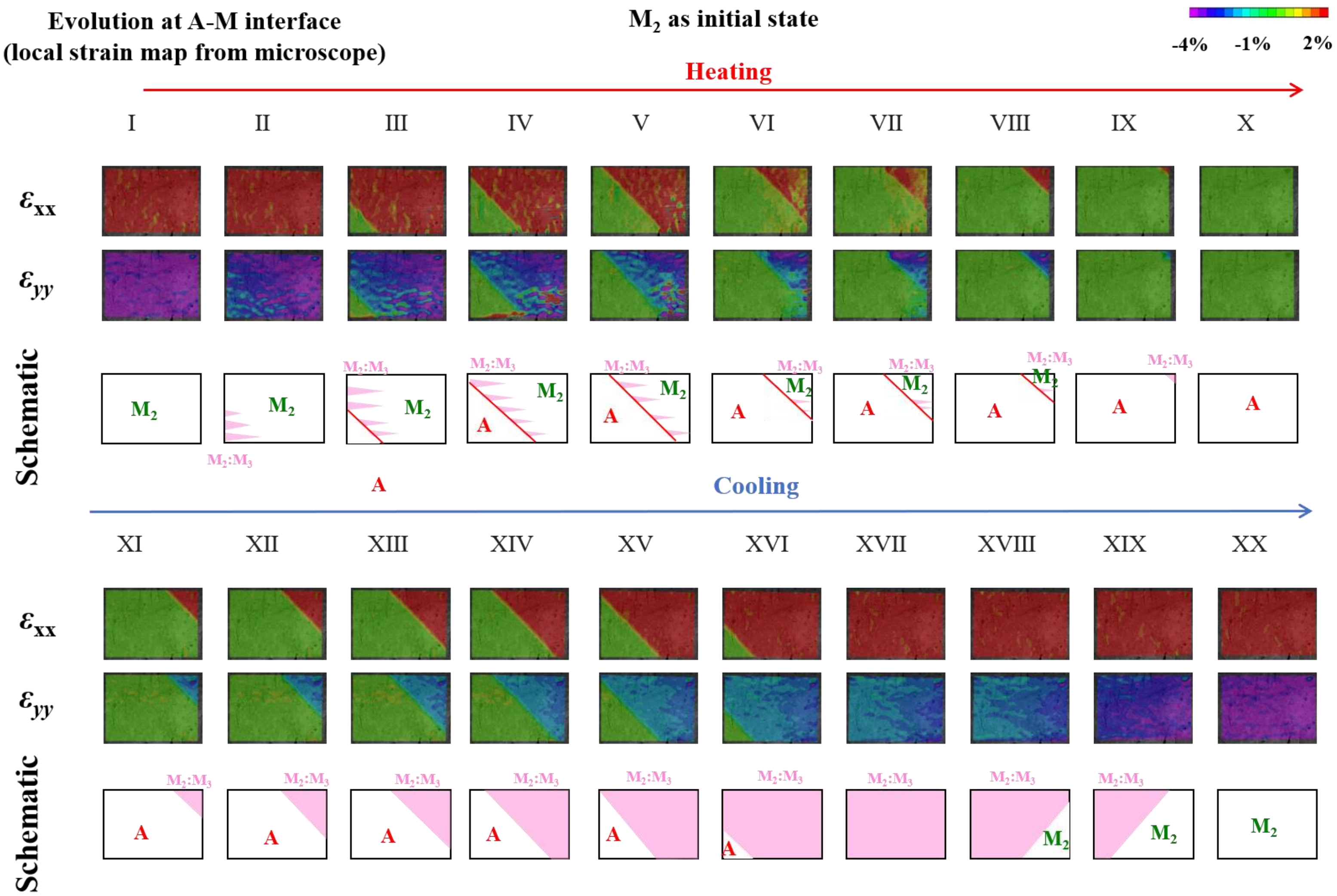

Figure D2 The observation by the microscope on the local strain evolution during the heating-cooling cycle of "Partial specimen under transformation" with the initial martensite state of M_2 in the thick specimen.

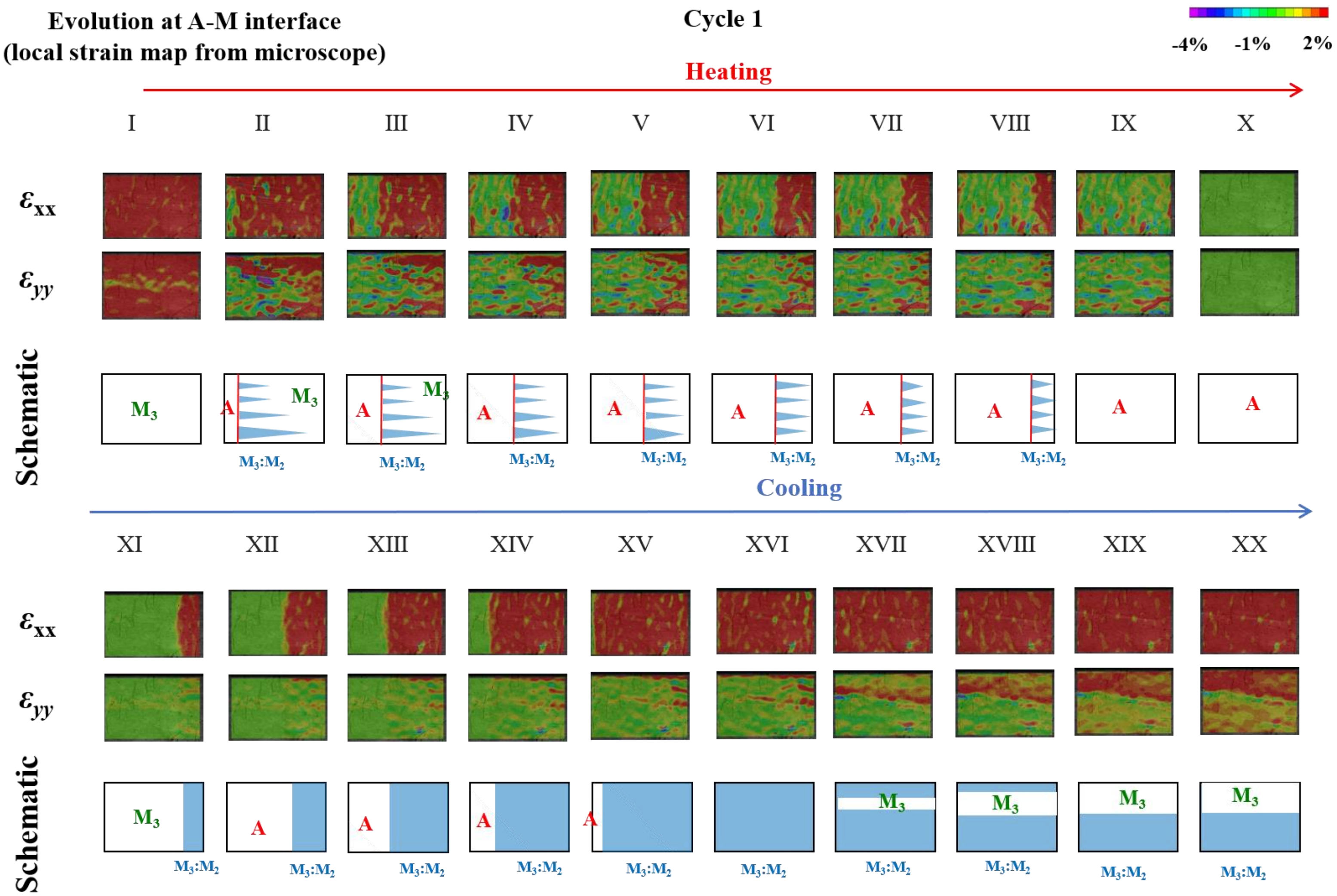

Figure D3 The observation by the microscope on the local strain evolution during the heating-cooling cycle of "Partial specimen under transformation" with the initial martensite state of M_3 in the thick specimen.

Bibliography

Arndt, M., Griebel, M., Novák, V., Roubíček, T., Šittner, P., 2006. Martensitic transformation in NiMnGa single crystals: Numerical simulation and experiments. Int. J. Plasticity 22, 1943-1961.

Aydogdu, Y., Aydogdu, A., Adiguzel, O., 2002. Self-accommodating martensite plate variants in shape memory CuAlNi alloys. Journal of Materials Processing Technology 123, 498-500.

Basso, V., Sasso, C.P., Skokov, K.P., Gutfleisch, O., Khovaylo, V.V., 2012. Hysteresis and magnetocaloric effect at the magnetostructural phase transition of Ni-Mn-Ga and Ni-Mn-Co-Sn Heusler alloys. Physical Review B 85.

Balandraud, X., Zanzotto, G., 2007. Stressed microstructures in thermally induced M9R–M18R martensites. J. Mech. Phys. Solids 55, 194-224.

Ball, J.M., James, R.D., 1987. Fine phase mixtures as minimizers of energy. Archive for Rational Mechanics and Analysis volume 100, 13–52.

Bhattacharya, K., 1992. Self-accommodation in martensite, Arch. Rational Mech. Anal. 120(3), 201-244.

Bhattacharya, K., 2003. Microstructure of Martensite: Why it Forms and How it Gives Rise to the Shape-memory Effect. Oxford University Press, Oxford.

Bruno, N.M., Wang, S., Karaman, I., Chumlyakov, Y.I., 2017. Reversible Martensitic Transformation under Low Magnetic Fields in Magnetic Shape Memory Alloys. Sci. Rep. 7, 40434.

Chai, Y.W., Kim, H.Y., Hosoda, H., Miyazaki, S., 2009. Self-accommodation in Ti–Nb shape memory alloys. Acta Mater. 57, 4054-4064.

Chemisky, Y., Duval, A., Patoor, E., Ben Zineb, T., 2011. Constitutive model for shape memory alloys including phase transformation, martensitic reorientation and twins accommodation. Mechanics of Materials 43, 361-376.

Chen, X., He, Y., 2020. Thermo-magneto-mechanical coupling dynamics of magnetic shape memory alloys. Int. J. Plasticity 129, 102686.

Chen, X., He, Y., Moumni, Z., 2013. Twin boundary motion in NiMnGa single crystals under biaxial compression. Mater. Lett. 90, 72-75.

Chen, X., Moumni, Z., He, Y., Zhang, W., 2014. A three-dimensional model of magneto-mechanical behaviors of martensite reorientation in ferromagnetic shape memory alloys. J. Mech. Phys. Solids 64, 249-286.

Chernenko, V.A., L'Vov, V.A., Cesari, E., Barandiaran, J.M., 2019. Fundamentals of magnetocaloric effect in magnetic shape memory alloys, Handbook of Magnetic Materials 28, 1-45.

Chernenko, V.A., L’Vov, V.A., Müllner, P., Kostorz, G., Takagi, T., 2004. Magnetic-field-induced superelasticity of ferromagnetic thermoelastic martensites: Experiment and modeling, Phys. Rev. B. 69, 134410.

Chmielus, M., Chernenko, V.A., Knowlton, W.B., Kostorz, G., Müllner, P., 2008. Training, constraints, and high-cycle magneto-mechanical properties of Ni-Mn-Ga magnetic shape-memory alloys. The European Physical Journal Special Topics 158, 79-85.

Chulist, R., Straka, L., Lanska, N., Soroka, A., Sozinov, A., Skrotzki, W., 2013. Characterization of mobile type I and type II twin boundaries in 10M modulated Ni–Mn–Ga martensite by electron backscatter diffraction. Acta Mater. 61, 1913-1920.

Chulist, R., Straka, L., Seiner, H., Sozinov, A., Schell, N., Tokarski, T., 2019. Branching of {110) twin boundaries in five-layered Ni-Mn-Ga bent single crystals. Materials & Design 171, 107703.

Cisse, C., Zaki, W., Ben Zineb, T., 2016. A review of constitutive models and modeling techniques for shape memory alloys. Int. J. Plasticity 76, 244-284.

Faran, E., Shilo, D., 2011. The kinetic relation for twin wall motion in NiMnGa. J. Mech. Phys. Solids 59, 975-987.

Faran, E., Shilo, D., 2013. The kinetic relation for twin wall motion in NiMnGa—part 2. J. Mech. Phys. Solids 61, 726-741.

Faran, E., Shilo, D., 2016. Ferromagnetic shape memory alloys — challenges, applications, and experimental characterization. Exp. Techniques 40, 1005-1031.

Gu, H., Bumke, L., Chluba, C., Quandt, E., James, R.D., 2018. Phase engineering and supercompatibility of shape memory alloys. Materials Today 21, 265-277.

Guilemany, J. M. et Fernandez, J.,1994. On the mechanism of two way shape memory effect obtained by stabilised stress induced martensite, Scripta Metallurgica et Materialia 30, 319-323.

Haldar, K., Lagoudas, D.C., Karaman, I., 2014. Magnetic field-induced martensitic phase transformation in magnetic shape memory alloys: Modeling and experiments. J. Mech. Phys. Solids 69, 33-66.

Haldar, K., Lagoudas, D.C., 2018. Dynamic magnetic shape memory alloys responses: Eddy current effect and Joule heating, J. Magn. Magn. Mater. 465, 278–289.

He, Y.J., Chen, X., Moumni, Z., 2011. Two-dimensional analysis to improve the output stress in ferromagnetic shape memory alloys. J. Appl. Phys. 110, 1-11.

He, Y.J., Chen, X., Moumni, Z., 2012. Reversible-strain criteria of ferromagnetic shape memory alloys under cyclic 3D magneto-mechanical loadings. J. Appl. Phys. 112, 33902.

He, Y.J., Sun, Q.P., 2010 a. Rate-dependent domain spacing in a stretched NiTi strip. International Journal of Solids and Structures 47, 2775-2783.

He, Y.J., Yin, H., Zhou, R., Sun, Q., 2010. Ambient effect on damping peak of NiTi shape memory alloy, Mater. Lett. 64, 1483–1486.

He, Y.J., Sun, Q.P., 2010 b. Frequency-dependent temperature evolution in NiTi shape memory alloy, Smart Mater. Struct. 19, 115014.

Heczko, O., Lanska, N., Soderberg, O., Ullakko, K., 2002. Temperature variation of structure and magnetic properties of Ni–Mn–Ga magnetic shape memory alloys. J. Magn. Magn. Mater. 242-245, 1446-1449.

Heczko, O., Seiner, H., Stoklasová, P., Sedlák, P., Sermeus, J., Glorieux, C., Backen, A., Fähler, S., Landa, M., 2018. Temperature dependence of elastic properties in austenite and martensite of Ni-Mn-Ga epitaxial films. Acta Mater. 145, 298-305.

Heczko O, Straka L (2004) Giant magneto-elastic strain-magnetic shape memory effect. Czechoslovak Journal of Physics 54, 611–614.

Heczko O. , Sozinov Alexei, Kari, U., 2000. Giant field-induced reversible strain in magnetic shape memory NiMnGa alloy. IEEE Transactions on Magnetics 36, 3266-3268.

Heczko, O., Veřtát, P., Vronka, M., Kopecky, V., Perevertov, O., 2016. Ni–Mn–Ga Single Crystal Exhibiting Multiple Magnetic Shape Memory Effects. Shap. Mem. Superelasticity 2, 272-280.

Henry, C.P., Bono, D., Feuchtwanger, J., Allen, S.M., O'Handley, R.C., 2002. ac field-induced actuation of single crystal Ni–Mn–Ga, J. Appl. Phys. 91,7810.

Hirth, J.P., Pond, R.C., 2011. Compatibility and accommodation in displacive phase transformations. Progress in Materials Science 56, 586-636.

Iadicola, M.A., Shaw, J.A., 2004. Rate and thermal sensitivities of unstable transformation behavior in a shape memory alloy. Int. J. Plasticity 20, 577-605.

James, R.D., Kohn, R.V., Shield, T.W., 1995. Modeling of Branched Needle Microstructures at the Edge of a Martensite Laminate. Le Journal de Physique IV 05, C8-253-C258-259.

James, R.D., Wuttig, M., 2009. Magnetostriction of martensite. Philos. Mag. A 77, 1273-1299.

Karaca, H., Karaman, I., Basaran, B., Chumlyakov, Y., Maier, H., 2006. Magnetic field and stress induced martensite reorientation in NiMnGa ferromagnetic shape memory alloy single crystals. Acta Mater. 54, 233-245.

Karaca, H.E., Basaran, B., Karaman, I., Chumlyakov, Y.I., 2012. Stress-induced martensite to austenite phase transformation in Ni2MnGa magnetic shape memory alloys. Smart Materials and Structures 21, 045011.

Karaca, H.E., Karaman, I., Basaran, B., Lagoudas, D.C., Chumlyakov, Y.I., Maier, H.J., 2007. On the stress-assisted magnetic-field-induced phase transformation in Ni_2MnGa ferromagnetic shape memory alloys. Acta Mater. 55, 4253-4269.

Karaman, I., Karaca, H.E., Basaran, B., Lagoudas, D.C., Chumlyakov, Y.I., Maier, H.J., 2006. Stress-assisted reversible magnetic field-induced phase transformation in Ni2MnGa magnetic shape memory alloys. Scripta Mater. 55, 403-406.

Kim, J.-h., Fukuda, T., Kakeshita, T., 2006. A new phase induced in Ni2MnGa by uniaxial stress. Scripta Mater. 54, 585-588.

Kiefer, B., Lagoudas, D.C., 2008. Modeling the Coupled Strain and Magnetization Response of Magnetic Shape Memory Alloys under Magnetomechanical Loading. J. Intel. Mat. Syst. Str. 20, 143-170.

Kohl, M., Reddy Y, S., Khelfaoui, F., Krevet, B., Backen, A., Fähler, S., Eichhorn, T., Jakob, G., Mecklenburg, A., 2009. Recent Progress in FSMA Microactuator Developments. Materials Science Forum 635, 145-154.

Kohl, M., Schmitt, M., Backen, A., Schultz, L., Krevet, B., Fähler, S., 2014. Ni-Mn-Ga shape memory nanoactuation. Appl. Phys. Lett. 104, 043111.

Lahoz, R., Gracia-Villa, L., and Puertolas, J. A., 2002. Training of the Two-Way Shape Memory Effect by Bending in NiTi Alloys . J. Eng. Mater. Technol. 124(4), 397–401.

Lexcellent C., Leclercq S., Gabry B., Bourbon G., 2000. The two way shape memory effect of shape memory alloys: an experimental study and a phenomenological model. International Journal of Plasticity 16(10-11), 1155-1168.

Li, D., Li, Z., Yang, J., Li, Z., Yang, B., Yan, H., Wang, D., Hou, L., Li, X., Zhang, Y., Esling, C., Zhao, X., Zuo, L., 2019. Large elastocaloric effect driven by stress-induced two-step structural transformation in a directionally solidified $Ni_{55}Mn_{18}Ga_{27}$ alloy. Scripta Mater. 163, 116-120.

Li, Y., Jiang, C., Liang, T., Ma, Y., Xu, H., 2003. Martensitic transformation and magnetization of Ni–Fe–Ga ferromagnetic shape memory alloys. Scripta Mater. 48, 1255-1258.

Liu, J., Gottschall, T., Skokov, K.P., Moore, J.D., Gutfleisch, O., 2012. Giant magnetocaloric effect driven by structural transitions. Nat Mater 11, 620-626.

Madangopal, K., 1997. The self accommodating martensitic microstructure of Nisingle bondTi shape memory alloys. Acta Mater. 45, 5347-5365.

Madangopal, K., Singh, J., Banerjee, S., 1991. Self-accommodation in Ni-Ti shape memory alloys. Scripta Metallurgica et Materialia 25, 2153-2158.

Madangopal, K., Singh, J.B., Banerjee, S., 1993a. The nature of self-accommodation in Ni-Ti shape memory alloys. Scripta Metallurgica et Materilia 29, 725-728.

Madangopal, K., Tiwari, R., Banerjee, S., 1993b. Microscopic self-accommodation in shape memory alloy martensites. Scripta Metallurgica et Materialia 28, 991-996.

Masdeu, F. , Pons, J., Chumlyakov, Y. , Cesari, E., 2021. Two-way shape memory effect in $Ni_{49}Fe_{18}Ga_{27}Co_6$ ferromagnetic shape memory single crystals, Materials Science and Engineering: A 805, 140543.

Miyazaki S., Otsuka K., Wayman C.M., 1989. The shape memory mechanism associated with the martensitic transformation in Ti-Ni alloys—I. Self-accommodation. Acta Metallurgica 37, 1873-1884.

Morito, H., Oikawa, K., Fujita, A., Fukamichi, K., Kainuma, R., Ishida, K., 2009. Stress-assisted large magnetic-field-induced strain in single-variant Co-Ni-Ga ferromagnetic shape memory alloy. J Phys Condens Matter 21, 256002.

Murray, S.J., Marioni, M., Allen, S.M., O’Handley, R.C., Lograsso, T.A., 2000. 6% magnetic-field-induced strain by twin-boundary motion in ferromagnetic Ni–Mn–Ga. Appl. Phys. Lett. 77, 886-888.

Novák, V., Šittner, P., Ignacová, S., Černoch, T., 2006. Transformation behavior of prism shaped shape memory alloy single crystals. Mat. Sci. Eng. A-Struct. 438-440, 755-762.

O'Handley R.C., Paul D.I., Marioni M. , Henry C.P., Richard M., Tello P.G., S.M., A., 2003. Micromagnetics and micromechanics of Ni-Mn-Ga actuation. J. Phys. IV France 112, 973-976.

Pagounis, E., Chulist, R., Szczerba, M.J., Laufenberg, M., 2014. Over 7% magnetic field-induced strain in a Ni-Mn-Ga five-layered martensite. Appl. Phys. Lett. 105, 1-5.

Pagounis, E., Chulist, R., Szczerba, M.J., Laufenberg, M., 2014. High-temperature magnetic shape memory actuation in a Ni–Mn–Ga single crystal, Scr. Mater. 83, 29–32.

Pascan, O.Z., He, Y.J., Moumni, Z., Zhang, W.H., 2015. Temperature rise of high-frequency martensite reorientation via Type II twin boundary motion in NiMnGa Ferromagnetic Shape Memory Alloy. Scripta Mater. 104, 71-74.

Pascan, O.Z., He, Y.J., Moumni, Z., Zhang, W.H., 2016. High-frequency performance of Ferromagnetic Shape Memory Alloys, Ann. Solid Struct. Mech. 8, 17–25.

Pascan, O.Z., 2015. Dynamic behaviors of Ferromagnetic Shape Memory Alloys. PhD thesis. Ecole Polytechnique de Paris.

Peng, Q., He, Y.J., Moumni, Z., 2015. A phase-field model on the hysteretic magneto-mechanical behaviors of ferromagnetic shape memory alloy. Acta Mater. 88, 13-24.

Pinneker, V., Gueltig, M., Sozinov, A., Kohl, M., 2014. Single phase boundary actuation of a ferromagnetic shape memory foil. Acta Mater. 64, 179-187.

Pinneker, V., R.Yin, Eberl, C., Sozinov, A., Ezer, Y., Kohl, M., 2013. Evolution of local strain bands of different orientation in single crystalline Ni–Mn–Ga foils under tension. J. Alloy Compd. 577, S358-S361.

Radelytskyi, I., Pękała, M., Szymczak, R., Gawryluk, D.J., Berkowski, M., Fink-Finowicki, J., Diduszko, R., Dyakonov, V., Szymczak, H., 2017. Magnetocaloric effect in Ni_2MnGa single crystal in the vicinity of the martensitic phase transition. J. Magn. Magn. Mater. 430, 16-21.

Ruddock, G., 1994. A Microstructure of Martensite which is not a Minimiser of Energy: the X-Interface. Arch. Rational Mech. Anal. 127, 1-39.

Schryversa, D., Boullay, P., Potapov, P.L., Kohn, R.V., Ball, J.M., 2002. Microstructures and interfaces in Ni–Al martensite: comparing HRTEM observations with continuum theories. International Journal of Solids and Structures 39, 3543-3554.

Sehitoglu, H., Wang, J., Maier, H.J., 2012. Transformation and slip behavior of Ni2FeGa. Int. J. Plasticity 39, 61-74.

Seiner, H., Glatz, O., Landa, M., 2011. A finite element analysis of the morphology of the twinned-to-detwinned interface observed in microstructure of the Cu–Al–Ni shape memory alloy. International Journal of Solids and Structures 48, 2005-2014.

Seiner, H., Sedlák, P., Landa, M., 2008. Shape recovery mechanism observed in single crystals of Cu–Al–Ni shape memory alloy. Phase Transitions 81, 537-551.

Seiner, H., Straka, L., Heczko, O., 2014. A microstructural model of motion of macro-twin interfaces in Ni–Mn–Ga 10M martensite, J. Mech. Phys. Solids. 64, 198–211.

Smith, A.R., Tellinen, J., Ullakko, K., 2014. Rapid actuation and response of Ni–Mn–Ga to magnetic-field-induced stress. Acta Mater. 80, 373-379.

Song, Y., Bhatti, K.P., Srivastava, V., Leighton, C., James, R.D., 2013. Thermodynamics of energy conversion via first order phase transformation in low hysteresis magnetic materials. Energy & Environmental Science 6, 1315-1327.

Sozinov, A., Lanska, N., Soroka, A., Straka, L., 2011. Highly mobile type II twin boundary in Ni-Mn-Ga five-layered martensite. Appl. Phys. Lett. 99, 124103.

Sozinov, A., Soroka, A., Lanska, N., Rameš, M., Straka, L., Ullakko, K., 2017. Temperature dependence of twinning and magnetic stresses in $Ni_{46}Mn_{24}Ga_{22}Co_4Cu_4$ alloy with giant 12% magnetic field-induced strain, Scr. Mater. 131, 33–36.

Straka, L., Heczko, O., Hannula, S.P., 2006. Temperature dependence of reversible field-induced strain in Ni–Mn–Ga single crystal. Scripta Mater. 54, 1497-1500.

Straka, L., Heczko, O., Hänninen, H., 2008. Activation of magnetic shape memory effect in Ni–Mn–Ga alloys by mechanical and magnetic treatment. Acta Mater. 56, 5492-5499.

Straka, L., Hänninen, H., Soroka, A., Sozinov, A., 2011a. Ni-Mn-Ga single crystals with very low twinning stress. Journal of Physics: Conference Series 303, 012079.

Straka, L., Heczko, O., Seiner, H., Lanska, N., Drahokoupil, J., Soroka, A., Fähler, S., Hänninen, H., Sozinov, A., 2011b. Highly mobile twinned interface in 10M modulated Ni–Mn–Ga martensite: Analysis beyond the tetragonal approximation of lattice. Acta Mater. 59, 7450-7463.

Straka, L., Soroka, A., Seiner, H., Hänninen, H., Sozinov, A., 2012. Temperature dependence of twinning stress of Type I and Type II twins in 10M modulated Ni–Mn–Ga martensite. Scripta Mater. 67, 25-28.

Stephan, J.M., Pagounis, E., Laufenberg, M., Paul, O., Ruther, P., 2011. A Novel Concept for Strain Sensing Based on the Ferromagnetic Shape Memory Alloy NiMnGa. IEEE Sensors Journal 11, 2683-2689.

Stupkiewicz, S., Maciejewski, G., Petryk, H., 2007. Low-energy morphology of the interface layer between austenite and twinned martensite. Acta Mater. 55, 6292-6306.

Techapiesancharoenkij, R., Kostamo, J., Allen, S.M., O’Handley, R.C., 2009. Frequency response of acoustic-assisted Ni-Mn-Ga ferromagnetic-shape- memory-alloy actuator, J. Appl. Phys. 105, 093923.

Techapiesancharoenkij, R., Simon, J., Bono, D., Allen, S.M., O’Handley, R.C., 2008. Acoustic-assist effect on magnetic threshold field and twinning-yield stress of Ni-Mn-Ga single crystals, J. Appl. Phys. 104, 33907.

Techapiesancharoenkij, R., Kostamo, J., Allen, S.M., O’Handley, R.C., 2009. Frequency response of acoustic-assisted Ni–Mn–Ga ferromagnetic-shape-memory-alloy actuator, J. Appl. Phys. 105, 93923.

Techapiesancharoenkij, R., 2011. The effect of magnetic stress and stiffness modulus on resonant characteristics of Ni–Mn–Ga ferromagnetic shape memory alloy actuators, J. Magn. Magn. Mater. 323, 3109–3116.

Teramoto, T., Nagahira, K., Tanaka, K., 2020. Geometry and energy barrier of martensite in the initial stage martensitic transformation in B19' TiNi shape memory alloy. Acta Mater. 201, 94-101.

Tzou, H.S., Lee, H.J., Arnold, S.M., 2004. Smart Materials, Precision Sensors/Actuators, Smart Structures, and Structronic Systems. Mechanics of Advanced Materials and Structures 11, 367-393.

Ullakko, K., Huang, J.K., Kantner, C., O'Handly, R.C., Kokorin, V.V., 1996. Large magnetic field-induced strains in Ni_2MnGa single crystals. Appl. Phys. Lett. 69, 1966.

Waitz, T., 2005. The self-accommodated morphology of martensite in nanocrystalline NiTi shape memory alloys. Acta Mater. 53, 2273-2283.

Waitz, T., Pranger, W., Antretter, T., Fischer, F.D., Karnthaler, H.P., 2008. Competing accommodation mechanisms of the martensite in nanocrystalline NiTi shape memory alloys. Mat. Sci. Eng. A-Struct. 481-482, 479-483.

Wang, J., Du, P., 2019. Theoretical study and numerical simulations on the stress-induced twin interface nucleation in single-crystalline NiMnGa alloys Theoretical study and numerical simulations on the stress-induced twin interface nucleation in single-crystalline NiMnGa alloys, J. Appl. Phys. 126, 115101.

Wang, W.H., Wu, G.H., Chen, J.L., Yu, C.H., Gao, S.X., S., Z.W., 2000. Stress-free two-way thermoelastic shape memory and field-enhanced strain in $Ni_{52}Mn_{24}Ga_{24}$ single crystals. Appl. Phys. Lett. 77, 3245-3247.

Webster, P.J., Ziebeck, K.R.A., Town, S.L., Peak, M.S., 1984. Magnetic order and phase transformation in Ni2MnGa. Philosophical Magazine B 49, 295-310.

Yin, R., Wendler, F., Krevet, B., Kohl, M., 2016. A magnetic shape memory microactuator with intrinsic position sensing, Sensors and Actuators: A Phys. 246, 48–57.

Yoo, I., Y. and Lee J. J.,2011. Two-way Shape Memory Effect of NiTi under Compressive Loading Cycles, Physics Procedia. 22, 449-454.

Yu, C., Kang, G., Fang, D., 2018. A Thermo-Magneto-Mechanically Coupled Constitutive Model of Magnetic Shape Memory Alloys, Acta Mech. Solida Sin. 31, 535–556.

Yu, C., Chen, T., Yin, H., Kang, G., Fang, D., 2020. Modeling the anisotropic elastocaloric effect of textured NiMnGa ferromagnetic shape memory alloys. International Journal of Solids and Structures 191-192, 509-528.

Yuan, B., Zhu, X., Zhang, X., Qian, M., 2019. Elastocaloric effect with small hysteresis in bamboo-grained Cu–Al–Mn microwires. Journal of Materials Science 54, 9613-9621.

Zhang, S., Chen, X., Moumni, Z., He, Y., 2018a. Coexistence and compatibility of martensite reorientation and phase transformation in high-frequency magnetic-field-induced deformation of Ni-Mn-Ga single crystal. Int. J. Plasticity 110, 110-122.

Zhang, S., Chen, X., Moumni, Z., He, Y., 2018b. Thermal effects on high-frequency magnetic-field-induced martensite reorientation in ferromagnetic shape memory alloys: An experimental and theoretical investigation. Int. J. Plasticity 108, 1-20.

Zhang, S., 2018. High Frequency Magnetic Field-induced Strain of Ferromagnetic Shape Memory Alloys. PhD thesis. Paris-Saclay University.

Zhang, S., Qin, G., He, Y., 2020. Ambient effects on the output strain of Ni–Mn-Ga single crystal magnetic shape memory alloy. J. Alloy Compd. 835, 155159.

Zhang, X., Feng, P., He, Y., Yu, T., Sun, Q., 2010. Experimental study on rate dependence of macroscopic domain and stress hysteresis in NiTi shape memory alloy strips. International Journal of Mechanical Sciences 52, 1660-1670.

Zhang, Z., James, R.D., Müller, S., 2009. Energy barriers and hysteresis in martensitic phase transformations. Acta Mater. 57, 4332-4352.

Zhou, T., Kang, G.Z., Yin, H., Yu, C., 2020. Modeling the two-way shape memory and elastocaloric effects of bamboo-grained oligocrystalline shape memory alloy microwire. Acta Mater. 198, 10-24.

Zreihan, N., Krimer, A., Avisar, D., Pagounis, E., Shilo, D., Faran, E., 2019. Microstructure evolution and kinetic laws for the motion of multiple twin boundaries in Ni–Mn–Ga. Functional Materials Letters 12.

Titre : La relation entre la transformation de phase martensitique et la réorientation martensitique dans les alliages magnétiques à mémoire de forme de Ni-Mn-Ga monocristal

Mots clés : transfert de chaleur, reorientation martensitique induit par le champs magnetic, auto-accommodées, two-way shape memory effect, compatibilité, martensite detwinning.

Résumé : L'alliage magnétique à mémoire de forme (MSMA) est un candidat prometteur pour les actionneurs en raison de sa propriété de déformation induite par champ magnétique à haute fréquence. Dans la littérature, la réorientation de la martensite et la transformation de phase du monocristal Ni_2MnGa ont généralement été étudiées séparément. Leur interaction n'a pas encore été systématiquement étudiée. Dans cette thèse, je démontre dans deux situations typiques que la réorientation de la martensite et la transformation de phase peuvent avoir lieu simultanément, conduisant à des performances spéciales.

La première série d'expériences systématiques étudie l'effet thermique sur l'oscillation de déformation induite par le champ magnétique du monocristal de Ni_2MnGa en modifiant progressivement les conditions aux limites thermiques (de l'air ambiant immobile à un fort flux d'air). Les résultats montrent que à faible transfert de chaleur ambiant, la dissipation d'énergie de la réorientation de la martensite à haute fréquence peut déclencher l'augmentation de la température de l'échantillon, conduisant à la transformation de phase en phase austénite, qui peut à son tour moduler l'amplitude d'oscillation de déformation par la fraction de phase ajustement de la transformation de phase martensitique.

La deuxième série d'expériences systématiques étudie la transformation de phase martensitique des barres monocristallines Ni_2MnGa de différentes tailles géométriques sous différents cycles de chauffage-refroidissement sans contrainte ni champ magnétique. Les résultats expérimentaux montrent que la réorientation de la martensite s'est effectivement produite lors de la transformation de phase induite par le refroidissement sans aucune force motrice directionnelle (sans contrainte ni champ magnétique), ce qui peut avoir un grand changement de forme global.

Title : The relation between martensitic phase transformation and martensite reorientation in single crystal Ni-Mn-Ga magnetic shape memory alloy

Keywords : heat transfer, magnetic-field-induced martensite reorientation, self-accommodation, two-way shape memory effect, compatibility, martensite detwinning.

Abstract : Magnetic shape memory alloy (MSMA) is a promising candidate for actuators because of its high-frequency Magnetic-Field-Induced-Strain (MFIS) property. In literature, the martensite reorientation and phase transformation of Ni_2MnGa single crystal were usually studied separately. Their interaction has not yet been systematically studied. In this thesis, I demonstrate in two typical situations that both martensite reorientation and phase transformation can take place simultaneously, leading to some special performances.

The first set of the systematic experiments investigates the thermal effect on the magnetic-field-induced strain oscillation of Ni_2MnGa single crystal by stepwise gradually changing thermal boundary condition (from still ambient air to strong airflow). The results show that at weak ambient heat transfer, the energy dissipation of the high-frequency martensite reorientation can trigger the temperature increase of the specimen, leading to the phase transformation to austenite phase, which can in turn modulate the strain oscillation amplitude by the phase-fraction adjustment of the martensitic phase transformation.

The second set of the systematic experiments investigates the martensitic phase transformation of the Ni_2MnGa single crystal bars of different geometric sizes under different heating-cooling cycles without stress or magnetic-field. The experimental results show that the martensite reorientation indeed occurs during the cooling-induced phase transformation without any directional driving force (i.e., without stress or magnetic field), which can have a large global shape change.

Institut Polytechnique de Paris
91120 Palaiseau, France